Department of Precision and Microsystems Engineering

High Potential

Design, modelling, and fabrication of a novel unipolar micro-electret transducer

Frank Schilperoort

Report no : 2022.078
Coach : E. van de Wetering
Professor : M. K. Ghatkesar
Specialisation : MNE
Type of report : MSc Thesis
Date : 11 November 2022

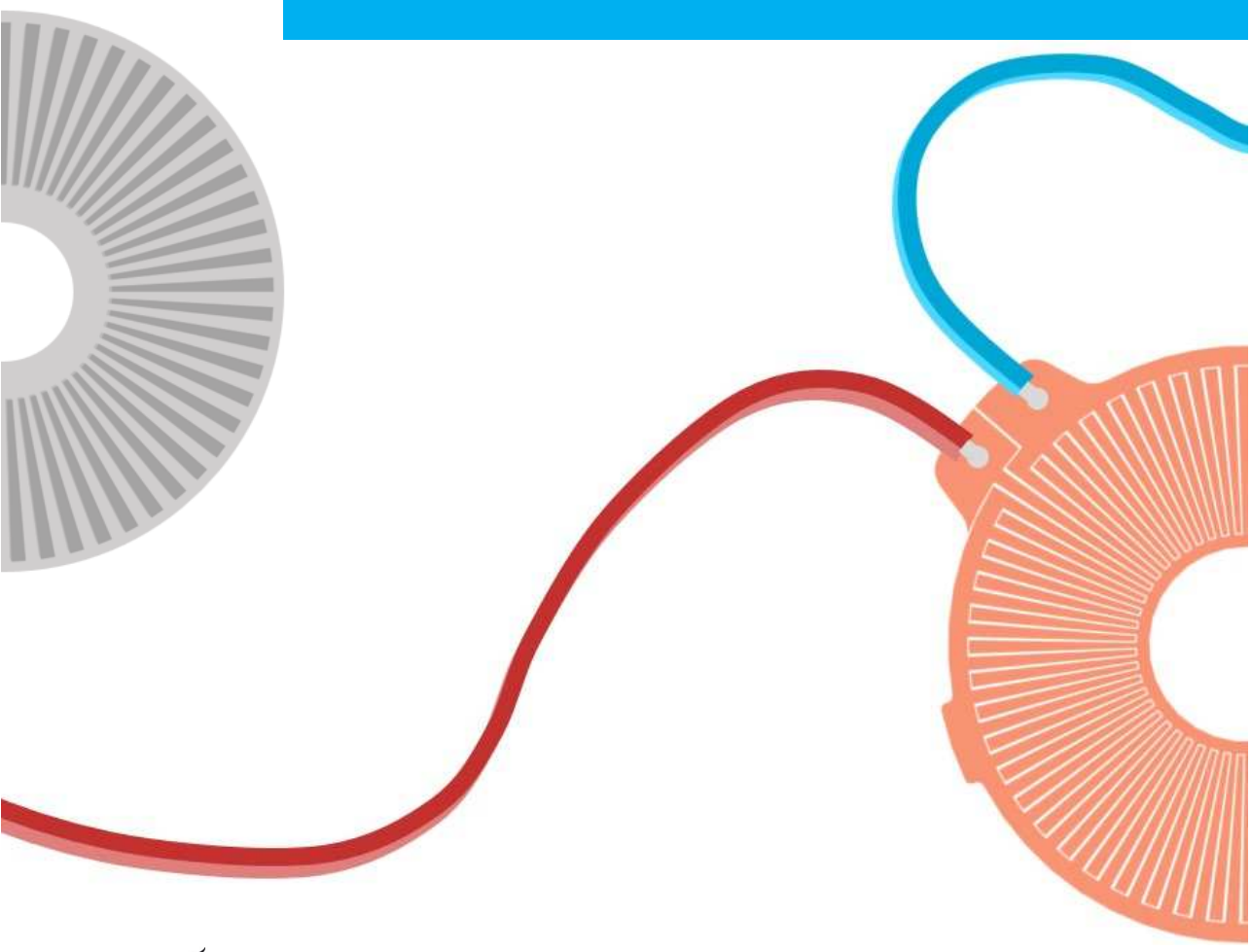

TU Delft Delft University of Technology

Challenge the future

HIGH POTENTIAL

DESIGN, MODELLING, AND FABRICATION OF A NOVEL UNIPOLAR MICRO-ELECTRET TRANSDUCER

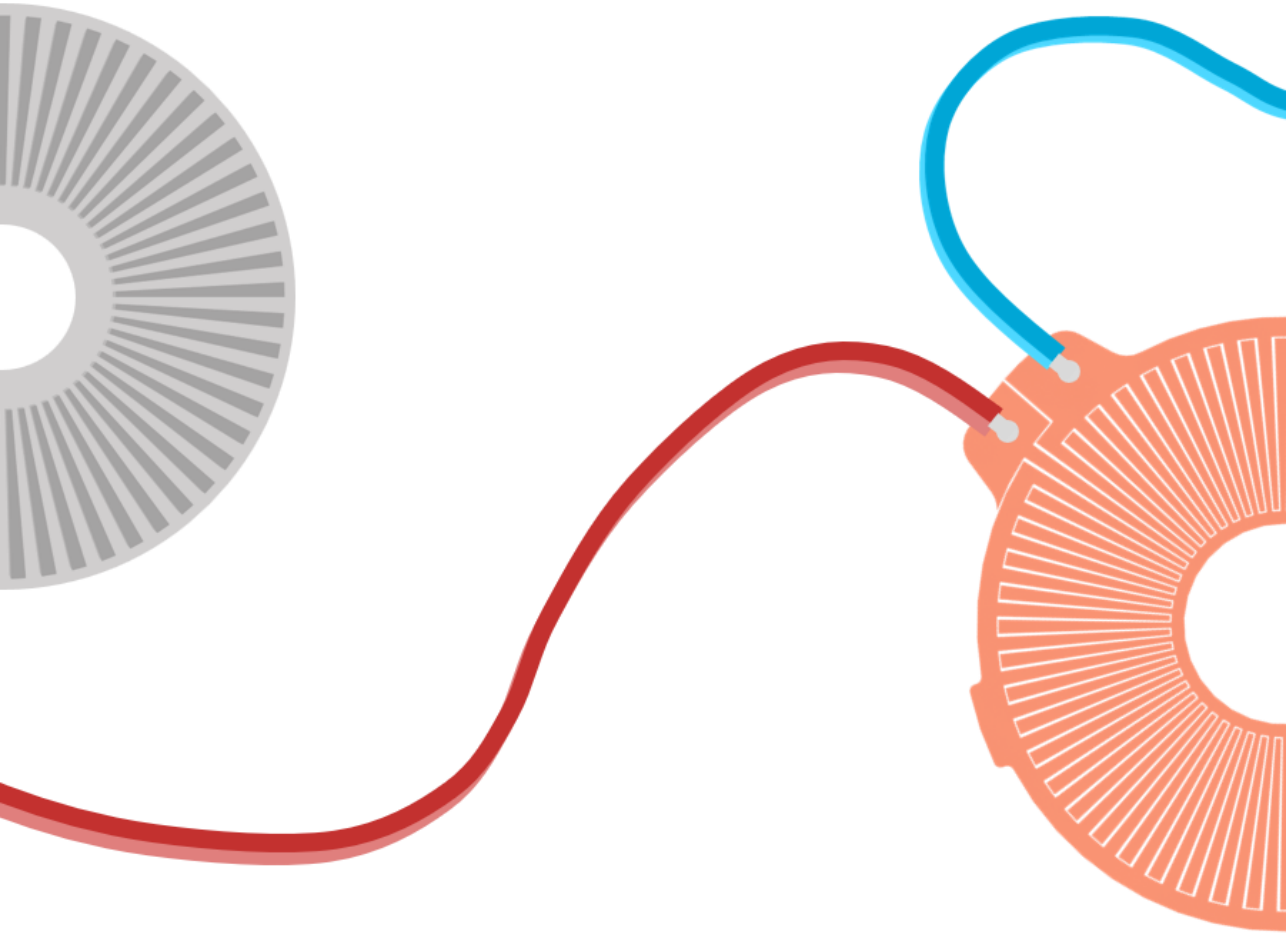

Frank SCHILPEROORT

HIGH POTENTIAL

DESIGN, MODELLING, AND FABRICATION OF A NOVEL UNIPOLAR MICRO-ELECTRET TRANSDUCER

MSc Thesis

In partial fulfillment of the requirements for the degree of
Master of Science in Mechanical Engineering.
To be defended on the 25th of November, 2022 at 14:00

by

Frank SCHILPEROORT

This thesis was approved by the following committee:

Dr. M. Ghaffarian Niasar,	Delft University of Technology
Dr. M. K. Ghatkesar,	Delft University of Technology
Dr. G. J. Verbiest,	Delft University of Technology
Ir. E. van de Wetering,	Kinergizer

Keywords: Micro-electret transducer, Unipolar electret, Quartz watch

Front & Back: F. Schilperoort

CONTENTS

1

INTRODUCTION

The first chapter provides an introduction to the field of energy harvesting and discusses the relevance and opportunities of energy harvesting. Then, mechanical energy harvesting will be discussed and examples of energy harvesters applied in quartz watches will be shown and evaluated. Hereafter, the shortcomings of current energy harvester transducers will be explained, and an alternative transduction method is proposed. Finally, the problem statement will be formed followed by an outline of the remainder of this thesis.

1.1. RELEVANCE OF ENERGY HARVESTING

With the advancements in micro-electromechanical systems (MEMS), the emergence of more complex Wireless Sensor Networks (WSN), and the Internet of Things (IoT), improvements to the energy supply of devices and sensors become increasingly important [1, 2]. There are two conventional methods for powering devices and sensors.

- Energy is provided by means of an **energy reservoir**, which has a finite amount of energy. When all the energy in the reservoir is used up, either the energy reservoir has to be refilled or replaced entirely. Examples of energy reservoirs are batteries, fuel cells, and springs.
- Energy is provided by the means of **connection to a central power supply**, such as an electrical grid. In this way, the device can be powered indefinitely, as long as the electrical grid remains operational.

Both of these methods have considerable downsides. When using an energy reservoir, the lifetime of the device is limited by its capacity. The energy reservoir also generally takes up a large volume of the device. The energy reservoir can be refilled or replaced, but this increases cost and wastage, and poses issues with reliability. Connection to a central power supply requires significant infrastructure and limits the flexibility of use [3].

This calls for alternative methods to power devices. There is a third method that has garnered attention in recent years, namely **energy harvesting**. With energy harvesting, ambient environmental energy is harvested and converted into energy that can be used to power a device, as is shown in Figure 1.1. When an energy harvester is suitably designed for the device it has to supply of power and the environment it operates in, it allows the device to run indefinitely. This increases the long-term reliability of the device and decreases cost, as the lifetime is not limited by the capacity of an energy reservoir. It also ensures that the device is flexible, which is an advantage compared to powering the device through a connection to a central power supply.

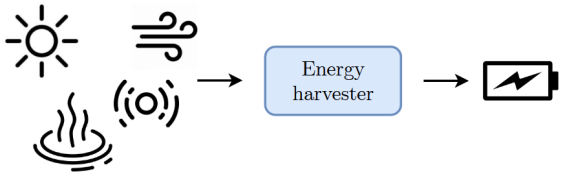

Figure 1.1: The principle of energy harvesting: environmental energy is used by an energy harvester that converts it into useful electrical energy.

A number of energy harvesting methods are displayed in Table 1.1. The energy harvesting methods are categorized based on the energy type, the transduction method (i.e. the method of converting said energy source into electrical energy), the source of the energy, and the fundamental limits of the energy harvesting methods.

Table 1.1: Energy harvesting methods.

Energy type	Transduction Method	Energy source	Fundamental limits
Thermal	Seebeck effect	Waste heat, body heat, geothermal energy	Temperature gradients, Carnot efficiency
Radiant	Photovoltaic	Sunlight, artificial light	Irradiance of light, Solar cell efficiency
	Electromagnetic (recieving antenna)	Mobile phones, wifi-routers, radio broadcast stations	Transmitter's distance & emitted power, RF to DC conversion efficiency
Mechanical	Electromagnetic Piezoelectric Electrostatic	Equipment vibration, building & vehicle vibration, human motion, wind, tides	Source acceleration & frequency, Proof mass displacement range, Transduction efficiency

Large-scale energy harvesting plays a large role in our every day lives. Think of solar panels, wind turbines, and geothermal power stations. These energy harvesters have been deployed around the world, supplying power to the central grid.

On the other end of the spectrum, micro-energy harvesting has received a lot of attention in recent decades for the purpose of powering small wearable devices, such as pacemakers, heart rate monitors, and quartz watches. The lifetime of these types of devices is typically limited by the battery capacity. Replacing or recharging the battery can be a nuisance at best. But in the case of pacemakers, this can result in the replacement of the entire device, needing a highly invasive procedure that has a large impact on the patient's life. Because of the forenamed reasons, energy harvesting is an attractive solution for these kinds of devices.

The power necessary to run these types of devices is generally on the microwatt scale [1, 4, 5]. To power these devices effectively, the energy harvester should be able to operate regardless of the environment that the wearer is in, making mechanical energy harvesting from human motion a promising energy type to harvest. Mechanical energy harvesting from human motion solely depends on the activity of the wearer. This allows for a robust embedded device whose performance does not depend on external environmental factors, such as the irradiance of light and the temperature, as is the case for photovoltaic and thermal energy harvesting respectively.

1.2. MECHANICAL ENERGY HARVESTING

A mechanical energy harvester consists of three fundamental components; mechanical conversion, mechanical-to-electrical transduction, and power processing, as is shown in Figure 1.2.

- **Mechanical conversion:** Before mechanical energy can be converted into electrical energy, it has to be conditioned in such a way that it can be efficiently handled by a transducer. Think of a wind turbine. The mechanical source energy is the kinetic energy of the air molecules, but this energy cannot be directly converted

into electrical energy. It first has to be converted into motion of the blades, before it can be transduced.

- **Transduction:** When the mechanical energy is converted into an appropriate form, it is ready to be transduced. Transduction is the conversion of mechanical energy into electrical energy. Several transduction mechanisms have been identified. The three most common transduction methods; electrostatic, electromagnetic, and piezoelectric transduction are discussed in more detail in chapter 2.
- **Power processing:** Although power processing can have a large influence the performance and design of an energy harvester, it is out of scope for this thesis and deserves a separate study in its own right. Therefore, power processing has largely been omitted from this study. The potential efficiency of power processing is used as a consideration for specific cases where low efficiency and difficulty of power processing pose obvious significant problems.

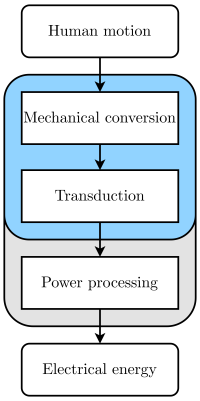

Figure 1.2: Schematic of the fundamental parts of an energy harvester, with the research focus highlighted in blue.

1.3. ENERGY HARVESTING FOR QUARTZ WATCHES

This thesis focuses on energy harvesting for the purpose of powering quartz watches. Quartz watches are watches that use a piezoelectric quartz crystal to regulate time. Conventional quartz watches are powered using electrical energy that is stored in a button cell, which is a type of primary battery. Primary batteries are portable voltaic cells that are not rechargeable, whereas secondary batteries are rechargeable portable voltaic cells. In 2018, only 48 % of portable batteries sold in the EU were collected for recycling. This means that large amounts of valuable resources are lost. Of these, some 35 kilotonnes of portable batteries end up in municipal waste annually (with possible leaching of hazardous substances). The European Commission is currently reviewing the Batteries Directive 2006/66/EC with the main focus on environmental sustainability. The proposed measures under discussion include a restriction or even a total ban of primary batteries [6].

Because of the forenamed reason, an alternative to the conventional button cell in quartz watches is necessary. One solution would be replacing the button cell with a secondary battery, which can be recharged by the user. The downside is that secondary batteries have a lower volumetric energy density than primary batteries. Although the secondary (rechargeable) batteries have improved, a regular household alkaline primary battery can provide 50% more energy than a ithium-ion battery, one of the highest energy-dense secondary batteries [7]. This means that the wearer would have to recharge the battery regularly, which is not preferable from the perspective of the user experience. For this reason, human motion energy harvesting is a better solution. The power consumption of a quartz watch is approximately 3 μW [8]. This low level of energy consumption means that the available energy from human wrist motion is large enough to power quartz watches using an appropriate energy harvester [3, 9].

1.3.1. DEVELOPMENT OF QUARTZ WATCH ENERGY HARVESTERS

Energy harvesting in quartz watches is not a totally new concept. The first implementation of energy harvesting in quartz watches is the Seiko Automatic Generation System (AGS) launched in 1988. A schematic of the Seiko AGS energy harvester is shown in Figure 1.3. The main components comprising the energy harvester are shown in Figure 1.4. The Seiko AGS energy harvester uses a watch rotor (in Figure 1.3 referred to as oscillating weight') that rotates as a result of human motion. This rotation is then amplified by means of a gear train and transferred to a magnet. The magnet will thus rotate at a higher angular velocity than the watch rotor, and through electromagnetic transduction induce a potential difference in the wound coil next to the magnet. The average power that can be generated using the seiko AGS system has been determined to be 0.5 μW during daily use [10]. This is lower than the energy consumption of the quartz watch as stated in section 1.3.

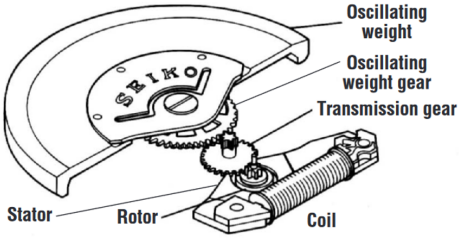

Figure 1.3: Schematic of the Seiko Automatic Generation System (AGS) energy harvester. (Courtesy of Paradiso and Starner (2005) [11])

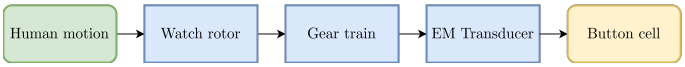

Figure 1.4: Block diagram showing the main components of the Seiko AGS energy harvester. The green block represents the input energy, the blue blocks represent the energy harvester components, and the yellow block represents the energy reservoir.

In 1996, ETA introduced the ETA autoquartz Self-Winding Electric Watch, as shown in Figure 1.5. The working principle is much the same as the Seiko AGS, with a notable exception being the micro-spring that is used to store the mechanical energy from the user before it is transferred to the transducer. In this way, energy in the spring can build up. When the spring is fully wound, it unwinds rapidly, transferring energy to the transducer at its optimal rate of 15,000 rotations per minute. The transducer is pulsed for 50 ms at a time, yielding a current of 6 mA at a potential greater than 16V [11]. The generated power is stored in a battery as an energy buffer for the quartz watch to extract energy from. The main components of the ETA autoquartz can be seen in Figure 1.6.

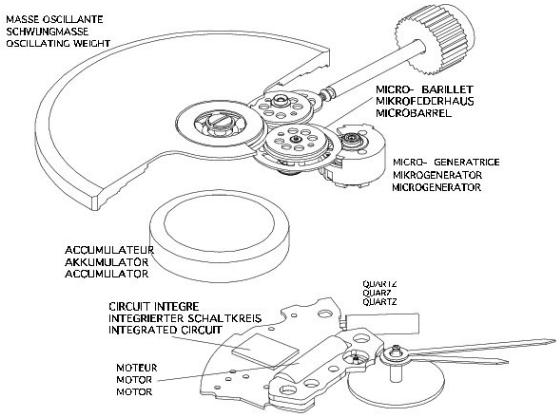

Figure 1.5: ETA Autoquartz energy harvester. (Courtesy of Paradiso and Starner (2005) [11])

Figure 1.6: Block diagram showing the main components of the ETA autoquartz energy harvester. The green block represents the input energy, the blue blocks the energy harvester components, and the yellow blocks the energy reservoir.

In 1999, Seiko introduced the spring drive energy harvester. In Figure 1.7, a schematic figure of the Seiko spring drive mechanism is shown. In the Seiko spring drive energy harvester, a main spring is used to store energy. The main spring is wound by the rotation of a watch rotor, much the same as with traditional mechanical watches. The main spring unwinds slowly at a constant rate. The energy released is used to turn the watch hands, and also induces a rotation of the electromagnetic transducer. This transducer converts mechanical energy into electrical energy. The generated electricity powers the integrated circuit (IC) and the piezoelectric quartz oscillator linked to it, with the latter generating a precise reference signal. The IC compares this signal to the rotating speed of the transducer. The regulator periodically applies an electromagnetic brake to ensure that the transducer's rotation is aligned with the reference signal from the quartz oscillator. The IC monitor compares the speed of the transducer with the reference signal

and intermittently extracts more energy to prevent excessively fast rotation [12]. In this way, the battery is entirely omitted, and the main spring is used as an energy reservoir instead. The main components of the Seiko spring drive can be seen in Figure 1.8.

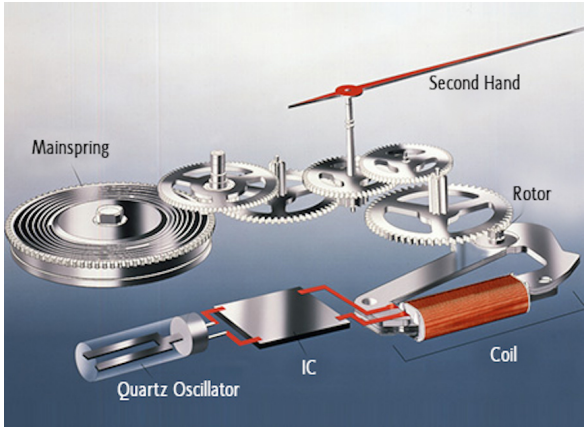

Figure 1.7: Seiko Spring drive energy harvester (Courtesy of Seiko [13]).

Figure 1.8: Block diagram showing the main components of the Seiko spring drive energy harvester. The green block represents the input energy, the blue blocks the energy harvester components, and the yellow block the energy reservoir.

In Table 1.2, the main properties of the three quartz watch energy harvesters discussed in this section is presented.

Table 1.2: Properties of energy harvesters applied in quartz watches.

Energy harvester	**Seiko AGS**	**ETA Autoquartz**	**Seiko Spring Drive**
Year of introduction	1988	1996	1999
Maximum output voltage [V]	0.6 [14]	16 [11]	1.5 [15]
Average output power [μW]	0.5 [10]	5 [9]	0.025 [16]
Energy storage method	Battery	Battery & Spring	Spring
Transduction method	Electromagnetic	Electromagnetic	Electromagnetic

1.3.2. ELECTROMAGNETIC TRANSDUCTION

Although the three quartz watch energy harvesters discussed in subsection 1.3.1 all use different mechanical designs, their transducers are much the same. They all use an electromagnetic transducer, consisting of a magnet rotor and a wound coil. Electromagnetic transduction is the most well-established transduction method and offers a robust

method to achieve high power densities. However, for micro-energy harvesters, electromagnetic transducers have several major drawbacks. For electromagnetic transducers, the voltage scales proportionally with the angular velocity and the number of coil turns squared.

$$U \propto \omega N^2 \tag{1.1}$$

Where U is the output voltage, ω is the angular velocity, and N is the number of coil turns. For micro-electromagnetic transducers, the number of coil turns is limited due to the size limitations of the device. If the rotational velocity of the watch rotor is not amplified through a form of transmission or frequency-up-conversion, the voltage output would be very low, in the mV range. The generated potential would be AC voltages that need to be rectified to be used as a power source for micro-electronics. To rectify the voltages, they would have to be transformed up to the range of two to several Volts, necessitating a transformer with a conversion ratio on the order of 100 [17]. Such a transformer in turn increases the volume and reduces the efficiency of the energy harvester drastically.

To increase the output voltage of the transducer without the need for a transformer, as is the case for the forenamed quartz watch energy harvesters, transmission is used in the form of a gear train between the watch rotor and the transducer. This gear train amplifies the angular velocity of the watch rotor, increasing the angular velocity of the transducer and thus increasing the output potential. However, transmission is not a perfect solution, as the added gear train increases the cost and volume of the device, and is subject to wear and tear. For the Seiko AGS, the energy harvester only generates sufficient energy during high angular velocity of the watch rotor, which is only achieved through activities such as running or forcibly shaking. When the angular velocity is too low, the transducer output potential is too low to generate any energy [10].

To solve this problem, the ETA autoquartz first stores the energy harvested from human motion as potential energy in a micro-spring. The energy stored in the micro-spring is released in short pulses, achieving very high angular velocities of the transducer. The Seiko spring drive also stores the energy harvested from human motion as potential energy in a spring, but instead, the spring is allowed to unwind slowly. The angular velocity of the unwinding of the spring is amplified by a gear train.

What can be concluded from the analysis of the current quartz watch energy harvesters, is that they all use similar electromagnetic transducers. These electromagnetic transducers have inherent disadvantages when applied for energy harvesting on the micro-scale. The main disadvantage is that high angular velocities are needed to achieve a high output voltage. Other disadvantages are the difficulty in miniaturization due to the need for coils, integrated permanent magnets, and ferromagnetic materials for the flux path.

1.3.3. ELECTRET TRANSDUCTION

In the forenamed energy harvesters, the solutions offered to the problems posed by electromagnetic transduction are merely in the mechanical design of the energy harvesting mechanism. The transducers are all similar. In this thesis, an alternative transducer is proposed, which would make complicated mechanisms, such as the mechanisms used in the energy harvesters discussed in subsection 1.3.1 largely redundant.

Electret transduction is a promising alternative transduction method for quartz watch applications. Electrets are dielectric materials that have embedded quasi-permanent electric charges. They are electrostatic dipoles, analogous to permanent magnets (which are magnetic dipoles) that can embed stable charges for decades [18].

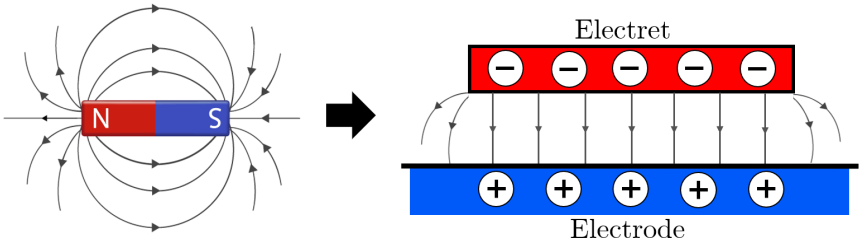

Figure 1.9: Magnet with its magnetic field vs. electret with its electrostatic field.

Electret transducers use capacitive structures made of two electrodes separated by air, vacuum, or a dielectric material. The electret is used to induce charges on an electrode, which allows for an energy cycle that does not require an energy source to polarize the structure. The change in capacitance induces an output voltage directly. A relative movement between the two electrodes, and thus a capacitance variation, leads to a difference in voltage according to the following relation.

$$U = \frac{Q}{C} \tag{1.2}$$

Where U is the voltage, Q is the charge, and C is the capacitance. In Figure 1.10, the simplest schematic representation of an electret transducer is shown. The electret delivers the bias voltage V_e, and the variable capacitor C_v changes capacitance due to displacement of the capacitor structure changing the charge, which flows across the load resistance R. This current across the load resistance in turn dissipates energy.

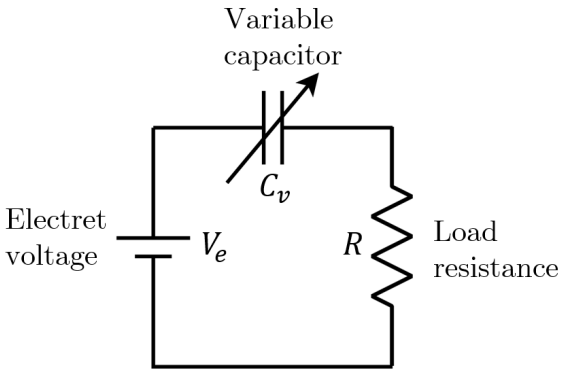

Figure 1.10: Schematic showing the electric circuit representation of an electret transducer.

An advantage of electret transducers at a small scale is that the output voltage is on the order of tens of volts, at low angular velocities [19–22]. This is because the output voltage at the matched load resistance is independent of the angular velocity in electret transducers. It is merely a function of the induced charge magnitude on the electrodes and the geometry of the transducer, which will be discussed in more detail in chapter 4. The continuous power generated by an electret transducer is dependent on multiple factors, but scales according to the following relation.

$$P \propto \frac{dC}{dt} Q_i^2 \tag{1.3}$$

Where P is the power generated, $\frac{dC}{dt}$ is the instantaneous change in capacitance, and Q_i is the induced charge.

1.4. PROBLEM STATEMENT

To summarize, quartz watches are powered using non-rechargeable batteries. These batteries are difficult to recycle and harmful to the environment. Therefore, there is a push for more legislation, including a restriction or even a ban on non-rechargeable batteries. An alternative method of powering quartz watches is thus necessary.

A promising alternative is energy harvesting from human motion. Energy harvesting in quartz watches is not a completely new concept, but conventional energy harvesters used in quartz watches have inherent flaws related to their transduction method, as they use electromagnetic transduction, which cannot achieve a high output potential from human motion at a small scale. To compensate for the flaws of electromagnetic transduction, conventional energy harvesters make use of elaborate mechanical designs, amplifying the input motion using gear trains and springs. This in turn increases the complexity and cost.

Micro-electret transducers do not suffer from a low output potential, as the output potential is not dependent on the angular velocity of the rotor. This reduces the need for elaborate mechanical designs amplifying the input motion. For a micro-electret transducer to be a viable alternative to conventional electromagnetic transducers, several requirements need to be fulfilled.

- The micro-electret transducer needs to have an average **output power** of at least **3 microwatts**, such that it can power a quartz watch continuously.
- The **voltage output** of the micro-electret transducer must be at least **3 volts**, such that the power generated can be conditioned by conventional integrated circuits.
- To ensure that the transducer can be manufactured used in quartz watches, it needs to be able to be manufactured at a **large scale**.

In accordance with the forenamed requirements, the following research objective is defined.

Research objective: *Design, model, and experimentally verify a microfabricated electret transducer that can be used to power a quartz watch.*

To be able to achieve this research objective, several research questions have to be answered. To be able to design and model a micro-electret transducer, an accurate model must first be developed. Then, the output power of an electret transducer needs to be maximized to ensure that the transducer can generate enough energy to power a quartz watch. The research questions are thus the following.

Research question: *How to accurately model and predict the output power characteristics of a micro-electret transducer?*

Research question: *How to maximize the output power of a micro-electret transducer?*

1.5. THESIS OUTLINE

This thesis will describe the design, fabrication, and experimental verification of a micro-electret transducer. In chapter 2, the literature study that was performed prior to the thesis works will be presented in the form of a literature review paper. The literature study is a review of human motion energy harvesting methods for the application of powering quartz watches. In chapter 3, the micro-electret transducer concept is introduced, and concept design decisions are explained and justified. In chapter 4 a novel electrostatic model for micro-electret transducers is introduced and experimentally verified, answering the first research question. In chapter 5, a novel 'unipolar' electret design is proposed and experimentally verified, which allows for maximizing the output power of electret transducers. In chapter 6, the experimental results from the fabricated micro-electret transducer prototype are used to develop a complete design of an energy harvester using a micro-electret transducer. Using a numerical model, the power generated by the energy harvester is compared under different activities of the wearer, such as computer work, walking, and running. In chapter 7 the results and the thesis process are discussed and conclusions are drawn. Recommendations are made for directions for future research. In Appendix A, Appendix B, and Appendix C, an extended theoretical background of electrets is given, design and fabrication details are discussed, and supporting measurements and experimental data are shown.

2

HUMAN MOTION ENERGY HARVESTING FOR QUARTZ WATCHES

In this literature review paper, energy harvesting methods for the purpose of powering wearable devices, specifically quartz watches, are investigated. Energy harvesters are categorized based on the characteristics of their mechanical design and their transduction method in a framework. The performance of reported energy harvesting methods is compared. For the transduction method, electret transducers look most promising due to their direct mechanical to electrical transduction, the improvements in charge stability, and the microfabrication compatibility.

Human motion energy harvesting for quartz watches

F. Schilperoort

***Abstract*— Energy harvesting is a well-developed field of research with a broad spectrum of reported working principles and architectures that have been theorized and experimentally verified. In this review, designers are provided with an overview of energy harvesting methods that can be applied to power wearable electronic devices, specifically quartz watches. Reported energy harvesters are categorized according to their working principles in a novel framework. The qualities and drawbacks of energy harvesting working principles are reviewed based on defined key parameters. Finally, conclusions are drawn based on the performance analysis of reported energy harvesters and the theoretical limitations of energy harvesting methods.**

Keywords: Energy harvesting, Non-resonant, Low-frequency, Human motion, Microsystems, Quartz watch

I. INTRODUCTION

With the advancements in microelectromechanical systems (MEMS), the emergence of more complex Wireless Sensor Networks (WSN), and the Internet of Things (IoT), improvements to the energy supply of devices and sensors become increasingly important [1, 2]. There are two conventional methods for powering devices and sensors.

- Either energy is supplied by means of an **energy reservoir**, which has a finite amount of energy, and when all the energy is used up, either the energy reservoir has to be refilled or replaced entirely. Think of batteries, fuel cells, and mechanical springs.
- The second option is supplying energy by the means of **connection to a central power supply**, such as an electrical grid. In this way, the sensor can be used indefinitely, as long as the electrical grid remains operational.

Both of these methods have considerable downsides. When using an energy reservoir, the lifetime of the device or sensor is limited by the capacity of the energy reservoir. The energy reservoir also usually takes up a large volume of the total device or sensor. The energy reservoir can be refilled or replaced, but this increases cost, and wastage, and poses issues with reliability. Connection to a central power supply requires significant expensive infrastructure and limits the flexibility of use [3]. This calls for alternative methods to power devices and sensors. A third method has garnered attention in recent years, which is energy harvesting. In energy harvesting, power is delivered through a device that harvests energy from the environment, and converts it into energy that can be used to power a device.

For quartz watches, energy harvesting is a promising solution to prolong the lifetime of devices and reduce wastage. This is because the power consumption of a quartz watch is on the scale of 3 μW [4]. This low energy consumption means that the energy from human wrist motion is high enough to power quartz watches indefinitely using an appropriate energy harvester (EH) [3].

Vibration energy harvesting has attracted a lot of attention over the past decade. Many researchers have attempted to design EHs based on different electrical to mechanical transduction mechanisms [5]–[7]. However, some of the energy harvesting devices fail to meet the requirement of the original goals as the transduction efficiency from mechanical vibrations to electrical energy is often lower than expected. This unsatisfactory result can occur for two reasons. Either the resonant frequency of the EHs is not matched with the frequency of the environmental vibrations, or the frequency bandwidth of the EH is limited to a specific range that cannot cover the stochastic vibration frequencies of external sources. The resulting output power of most EHs is drastically reduced when the frequency of the input motion deviates slightly from the resonant frequency of the EH [8].

The problem with human motion is that the accelerations induced on the EH are highly stochastic and the frequencies are very low, below 12 Hz [5, 9]. An additional challenge is that the amplitude of the input motion is large, on the order of millimeters to meters, compared to the maximum internal displacement in a quartz watch which is on the order of millimeters. The motion ratio is defined as the ratio between the internal displacement Z_l and the input displacement, which is equal to twice the input amplitude Y_0, as can be seen in Figure 2 [10]. For human motion energy harvesting, the motion ratio is smaller than one, as can be seen in Equation 5.

$$\lambda = \frac{Z_l}{2Y_0} \leq 1 \tag{1}$$

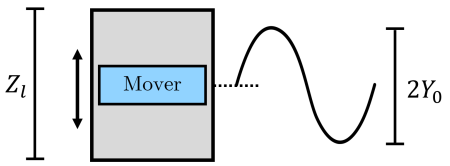

Fig. 1: Schematic of the internal displacement of an energy harvester Z_l, and the input amplitude Y_0.

This poses strict constraints on the EH, as resonance cannot be used to amplify the input motion which is a common method to achieve an efficient EH. Besides the maximum motion ratio, the bandwidth of a simple resonant EH is also too narrow to effectively harvest

energy from a non-resonant energy source. This shows that making a miniaturized efficient EH for non-resonant input accelerations is a difficult problem to solve.

In the following sections, the methods are explained, covering the search method, the definition of the classification, and key parameters found in the current research. Subsequently, the results are presented; EHs are categorized in a novel framework and their performance is judged according to this framework and experimental results from the literature. Lastly, the results are discussed and the conclusions are presented.

II. Method

In this section, the methods used for this review are presented. First, the search method is discussed, followed by the categorization, and then the key properties that are addressed.

A. Categorization

An EH consists of three fundamental components: mechanical conversion, mechanical-to-electrical transduction, and power processing. In this paper, the focus is on mechanical conversion and transduction. Although power conditioning is an essential part of an EH that has a great influence on its performance and design, it is out of the scope of this paper and deserves a separate study in its own right. Therefore, power processing has largely been omitted from this study. In this paper, the potential efficiency of power processing is used as a consideration for specific cases where low efficiency and difficulty of power processing pose obvious significant problems. A Schematic showing the fundamental components of an EH can be seen in Figure 2.

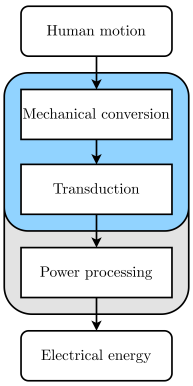

Fig. 2: Schematic of the fundamental components of an energy harvester, with the research focus highlighted in blue.

B. Key parameters

The performance of EHs is addressed according to several key parameters. For some parameters, a quantitative comparison cannot be made as there are too few EHs reported in the literature that publish data on the performance of these parameters, such as fabrication cost, lifetime, and bandwidth. Within these parameters, a qualitative comparison is still possible by comparing the fundamental theoretical principles used in the design of the EHs. The key parameters that are used to discuss the performance of EHs are defined as follows.

- **Power density:** The power density ρ_P of an EH is an essential parameter. It is calculated as the output power of the energy harvester divided by the volume as follows.

$$\rho_P = \frac{P}{V} \tag{2}$$

  The power density indicates the power that can be generated by EHs relative to their size and allows for the comparison of the performance of similar EHs.
- **Effectiveness:** The effectiveness of an energy harvester describes the performance of an energy harvester compared to the theoretical maximum energy harvested for a given input vibration as described by Roundy [11].

$$E_H = \frac{\text{Useful power output}}{\text{Maximum possible output}} \tag{3}$$

  For a single degree of freedom (sDoF) inertial vibrational energy harvester this results in the following expression.

$$E_H = \frac{\text{Useful power output}}{\frac{1}{2} Y_0 Z_l \omega^3 m} \tag{4}$$

  This concept is expanded in this paper to also include non-vibrational energy harvesters, such as the non-inertial rotational energy harvester described by Yeatman [12] and the sprung rotational inertial energy harvester described by Halim [13]. The maximum energy harvested from these devices is calculated using the theoretical relations described by Yeatman [14]. The effectiveness allows for a more objective comparison of EHs by accounting for the frequencies and amplitudes of the input motion. In this way, it is possible to compare EHs that operate in different conditions.
- **Miniaturization:** The EH must stay below certain dimensions for it to be possible to incorporate the EH in a quartz watch. If the EH has a significant impact on the size of the device it becomes an unattractive solution.
- **Fabrication cost:** The cost of the EH must be low enough such that it does not dominate the cost of the quartz watch. Otherwise there would not be an economic incentive to implement EHs in wearable electronic devices.
- **Lifetime:** The lifetime of the EH should be long enough such that it can outlive quartz watches that make use of a conventional disposable battery. The lifetime of a disposable battery in quartz watches is around five years.
- **Motion ratio:** The motion ratio of the EH is strictly constrained as described in section I and is calculated

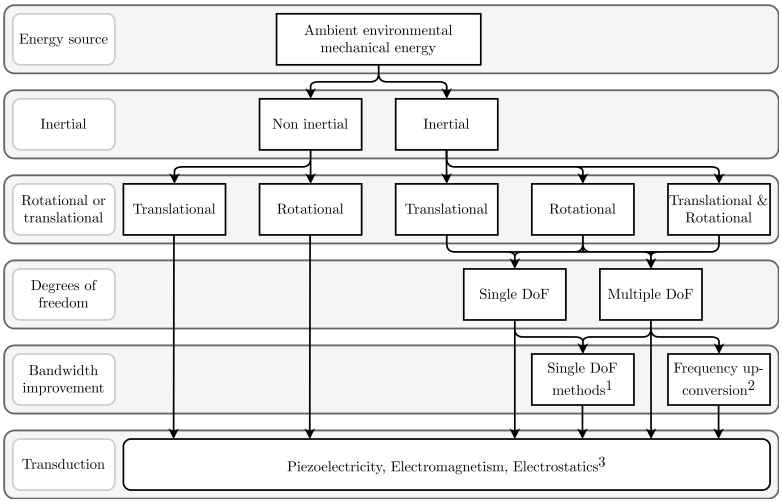

Fig. 3: Mechanical conversion design tree. 1: Elaborated on in subsubsection III-B.2. 2: Elaborated on in subsubsection III-B.1, 3: Elaborated on in subsection III-C.

according to Equation 5. The motion ratio greatly influences the design of the EH and should therefore be taken into account.

III. RESULTS

A. Mechanical design

Besides the transduction method, the human input motion needs to be conditioned such that kinetic energy can be efficiently transduced into electrical energy. This component of the EH is referred to as mechanical design.

To systematically compare all mechanical designs, a decision tree is made that uses multiple aspects of the designs found in existing research that can be seen in Figure 3. The different levels of design can be seen in the table in the rounded boxes on the left of Figure 3 and are more closely explained in the subsubsection III-A.1-subsection III-B. By using this method, designs can be compared more accurately and trends can be discovered between reported EH designs. This method also allows the decoupling of the mechanical design and the transduction methods, as these are largely mutually exclusive and are thus discussed separately.

1) Non-inertial and inertial: The first level of the design tree divides EHs into two categories; those that utilize the non-inertial direct application of force and those that make use of inertial forces acting on a proof mass.

The operating principle of a non-inertial EH is shown in Figure 20a. In this case, the driving force on a proof mass m supported on a suspension with spring constant k, with a damping element $f(\dot{z})$ present to provide a force opposing the motion. The variable Z_l represents the displacement limit, $z(t)$ the time-dependent displacement and $f_{dr}(t)$ the driving force.

If the damper is implemented by using a suitable transduction mechanism, then by opposing the motion, mechanical energy is converted to electrical energy. Non-inertial force generators must make mechanical contact with two structures that move relative to each other, and can thus apply a force on the damper. The operating principle of inertial EHs is shown in Figure 20b. In this figure, $y(t)$ is the displacement of the EH frame relative to the fixed world, and $x(t)$ is the displacement of the inertial proof mass m relative to the fixed world. A proof mass is supported on a suspension, and its inertia results in a relative displacement when the frame experiences acceleration. Energy is converted when work is done against the damping force, which opposes the relative motion. Inertial generators require only one point of attachment to a moving structure. In order to generate power, the damper must be implemented by means of a suitable transducer. This can be done using one of the methods described in section III-C.

2) Rotational and translational: The second subdivision is dividing energy harvesters into rotational and translational energy harvesters or in some special cases a combination of the two.

A translational EH is one where the proof mass moves in a straight line. This is the most common architecture for EHs. Most translational EHs only translate in 1 DoF and thus can also only harvest energy from accelerations applied in the respective direction. Translational EHs also have a limited internal displacement. An example of a schematic of a translational EH can be seen in Figure 20b.

In a rotational EH, the mover rotates around a point instead. A schematic of a rotational inertial EH can be seen in Figure 5 below. In this schematic, an eccentric mass m is able to rotate due to translations $x(t)$ and $y(t)$ and rotation $\omega(t)$

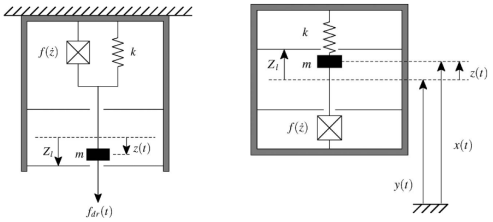

(a) (b)

Fig. 4: Schematic of non-inertial and inertial EHs. **(a)** Non-inertial or direct EH that uses direct application of force on the proof mass m to generate relative motion between the proof massand the EH frame. **(b)** Inertial EH that uses inertial forces to generate relative motion between the proof mass m and the EH frame. (Courtesy of Mitcheson et al. (2008) [3])

applied to the EH frame. A transducer delivers the damping force $f(\dot{\theta})$.

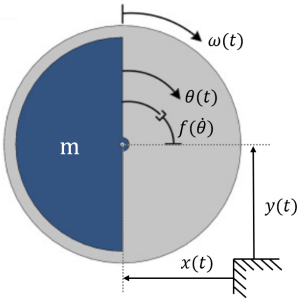

Fig. 5: Schematic of a non-inertial rotational energy harvester. (Courtesy of Fu et al. (2021) [15])

3) Degrees of Freedom (DoF): EHs are further split up into single DoF (sDoF) and multiple DoF (mDoF) designs. The number of DoFs of an EH is important as it determines which methods to increase the bandwidth can be applied.

B. Bandwidth improvement

To ensure that an EH functions optimally, its bandwidth needs to match the bandwidth of the input motion. Only by ensuring that the resonance frequency of the EH matches that of the motion, the EH will function optimally. For some devices, this is a relatively simple task. For example, EHs that are made to harvest energy from equipment connected to 50 Hz mains electricity have a specific narrow bandwidth to target.

However, for human motion energy harvesting this is not that straightforward. The motion of a human wrist is stochastic, intermittent, and mainly distributed in the low frequency ($< 12Hz$) as stated in section I. This means that many sDoF inertial EHs will struggle to efficiently extract energy as their bandwidth is too narrow. To combat this problem, multiple ways to increase the bandwidth of the EH can be used. Many EHs that use bandwidth improvement methods have been reported in the literature [5]–[7, 12, 16]–[22]. To be able to categorize the different methods that exist to increase the bandwidth of EHs, a framework has been made that encompasses all methods reported in the existing research. The framework can be seen in Figure 6.

1) Frequency up-Conversion (FupC): One well-reported method to increase the bandwidth of EHs is through the use of FupC. In FupC, a proof mass is put in motion by a low-frequency input motion. The transduction mechanism is actuated at its higher natural frequency through impact or a plucking mechanism. This is by definition only possible in mDoF energy harvesters. An example of a FupC EH can be seen in Figure 10. Where the revolving host excites the cantilever by magnetic forces between the revolving host magnet and the magnet on the cantilever.

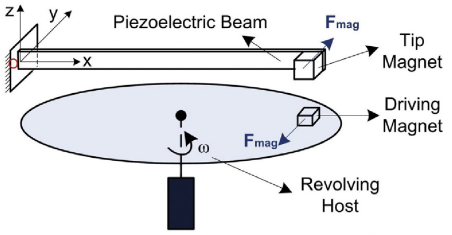

Fig. 7: Example of an energy harvester using frequency-up conversion. (Courtesy of [12])

FupCs can be further split up into plucking FupCs (Figure 8a), and impact FupCs (Figure 8b) [10], and are discussed respectively below.

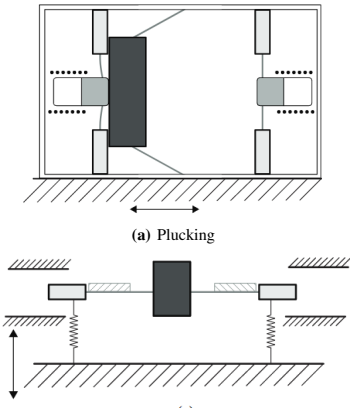

(a) Plucking

(b) Impact

Fig. 8: Plucking and impact frequency-up-conversion. (Courtesy of Blad and Tolou (2019) [10])

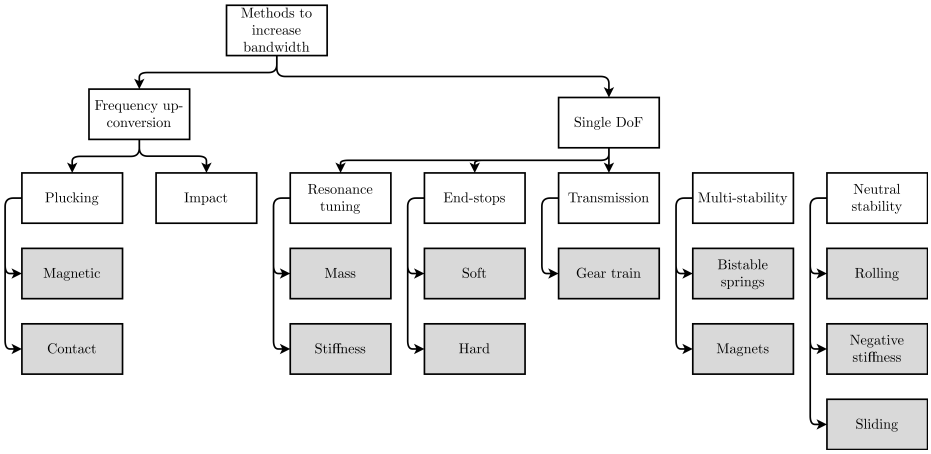

Fig. 6: Design tree showing the methods to increase the bandwidth of an energy harvester.

a) Plucking: In plucking FupC, a mass-spring system is actuated by a second system through means of contact or magnetic coupling. This induces a high force on the mass-spring system exciting all frequencies which causes the system to resonate.

b) Impact: In impact FupC, the main proof mass is constrained by end-stops and when accelerations are applied to the system, the main proof mass impacts these end-stops. This excites all frequencies of the second mass, which is attached to the proof mass through a spring, leading to resonance. An example of the output motion of an impact energy harvester can be seen in Figure 9.

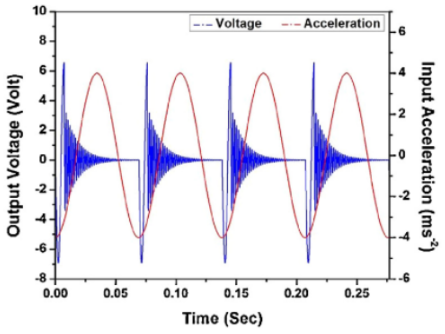

Fig. 9: Simulated waveform of an impact driven FupC energy harvester. (Courtesy of Halim and Park (2014) [23])

2) sDoF methods: sDoF methods can also be applied to increase the bandwidth of EHs. The sDoF methods discussed are resonance tuning, end-stops, transmission, multi-stability, and neutral stability.

a) Resonance tuning: Resonance tuning can increase the bandwidth of EHs by changing the resonance frequency to fit the frequency of the motion that is applied to the EH. Several configurations have been reported in the existing research. Tunable resonance frequency EHs were developed on open-loop ([24, 25]) and closed-loop ([26]) configurations. The open-loop configuration allows for adjusting the resonance frequency when the EH is not in operation, while the closed-loop configuration allows resonance tuning when it is in operation.

b) End-stops: Another method to widen the bandwidth is through the introduction of end-stops that constrain the displacement of the proof mass. During the vibration, the proof mass strikes the stopper. This affects the stiffness and causes the oscillation response to change from linear to non-linear. The new effective stiffness causes a widening of the operating range close to the resonance frequency of the vibrating structure [10], as is shown in Figure 10.

Two kinds of end-stops are identified in the current research. Soft-stops are end-stops that employ repelling magnets or mechanical springs such that the end-stop force on the proof mass gradually increases after initial impact with the end-stop. Hard-stops allow for minimal displacement, inducing a large load on the proof mass. The mechanics of hard-stops can be approximated by a non-linear spring of which the stiffness can be approximated by a static analysis of Hertz's contact [27].

c) Transmission: One straightforward bandwidth improvement method that has been applied in EHs such as Seiko's AGS EH, shown in Figure 16 is transmission. With transmission, a low-frequency input acceleration can be increased by means of a transmission such as a belt drive, gears, or a gear train.

d) Multi-stability: Multi-stable EHs make use of a mechanical design that allows for multiple stable states in their displacement range. This can be done by means of magnets as shown in Figure 11, or mechanical multi-stability such as bistable buckling beams as shown in Figure 12.

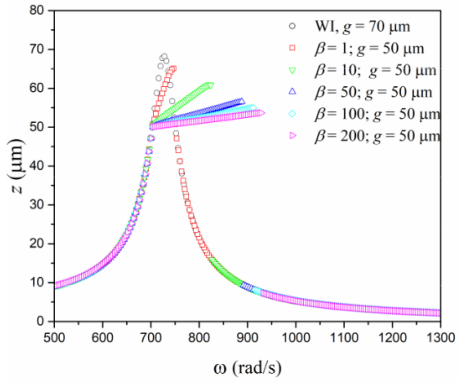

Fig. 10: The effect of end-stops on an up sweep for a gap of 50 μm and a stiffness ratio between the spring and end-stops β. (Courtesy of Ai et al. (2019) [28])

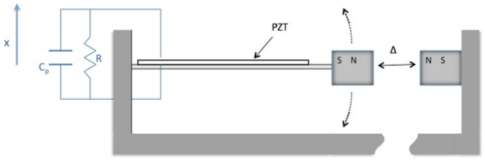

Fig. 11: Schematic of a magnetic multi-stable EH (Courtesy of Vocca et al. (2012) [29]).

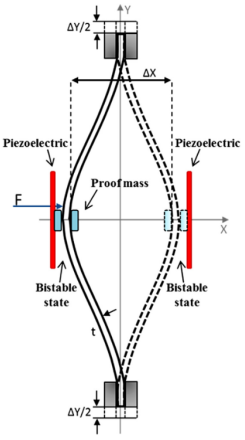

Fig. 12: Schematic of a buckling multi-stable EH (Courtesy of Ando et al. (2014) [30]).

e) Neutral stability: Neutral stability and statically balanced are synonyms for systems that exhibit constant potential energy over a certain range of motion. This means that the system can be put in a range of different stable positions. Zero-stiffness adds another aspect to this. Zero stiffness systems are neutrally stable and also exhibit quasi-zero stiffness throughout a certain range of motion. Zero stiffness EHs can be used to harvest low-frequency input motion as the resonance frequency is proportional to the square root of the stiffness of the spring for a simple mass-spring system.

$$\omega_r \propto \sqrt{k} \tag{5}$$

Where ω_r is the resonance frequency and k is the spring stiffness. Tolou et al. (2010) have shown that a stiffness reduction of 99% is possible, resulting in a decrease of the resonance frequency of factor ten [31]. Neutral stability in EHs can be achieved in several ways. An example of a zero stiffness EH is shown in Figure 13. In this EH, the proof mass moves with respect to the frame of reference using a linear guide supported by micro-balls [32]. Other zero stifness EHs are fabricated by omitting the spring entirely by having a loose mass in a constrained volume [22], or by using negative stiffness. Although the last method has not yet been applied for the application of energy harvesting.

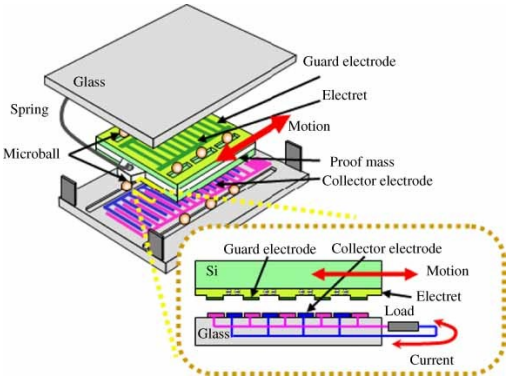

Fig. 13: Schematic of a zero stiffness EH (Courtesy of Suzuki (2011) [32]).

C. Transduction methods

There are broadly three different ways of converting mechanical energy into electrical energy: electromagnetic, electrostatic, and piezoelectric transduction. These transduction methods are shown in Table I with their main advantages and drawbacks.

1) Electromagnetic transduction: The most researched and well-established method of transduction is electromagnetic transduction. The majority of EHs used today are based on rotation and are used in numerous applications, from the large-scale generation of power in power stations to smaller-scale applications such as in cars to recharge the battery. Electromagnetic EHs (EMEHs) can also be used to harvest micro- to milliWatt levels of power. Provided an EMEH is correctly designed, they can

TABLE I: Advantages and drawbacks of the three common transduction methods [33][34] .

Transduction method	Advantage	Drawbacks
Electromagnetic	-High output currents -Long lifetime -Robustness	-Low output voltage -Complicated assembly -Not very MEMS compatible -Low efficiency for low frequencies and small device sizes
Electrostatic	-High output voltages -Possibility to build low cost systems -Easily adjustable coupling coefficient -High coupling coefficient possible -Size reduction increases capacitances	-Low capacitances -High impact of parasitic capacitances -Need for micrometer dimension control -No direct mechanical-electrical conversion for electret free converters
Piezoelectric	-High output voltages -High capacitances -No need to control any gap	-Expensive (material) -Coupling coefficient linked to material properties -Degradation

be efficient converters of kinetic energy into electrical. However, attempts to miniaturize the technique using MEMS technology to fabricate an EH, reduce efficiency levels considerably [35].

EMEHs are based on Faraday's law of electromagnetic induction. Faraday's law states that when an electric conductor is moved through a magnetic field, a potential difference is generated between the ends of the conductor. The voltage induced in a circuit is proportional to the time rate of change of the magnetic flux linkage of that circuit.

$$U = -\frac{d\phi}{dt} \tag{6}$$

Where U is the generated voltage and ϕ is the flux linkage. A schematic of an EMEH is shown in Figure 14.

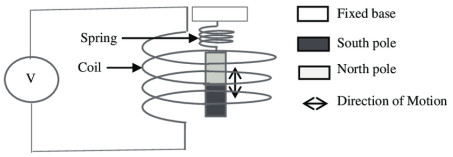

Fig. 14: Schematic of an electromagnetic energy harvester. (Courtesy of Batra and Alomari (2017) [36])

Power is extracted from the EH by connecting the coil terminals to a load resistance, allowing a current to flow through it. This current creates its own magnetic field which acts to oppose the field generated by the permanent magnet. By acting against this electromagnetic force, F_{em}, the mechanical energy is transformed into electrical energy. The electromagnetic force is proportional to the current and hence the velocity. Therefore, the product of electromagnetic damping D_{em} and the velocity $\frac{dx}{dt}$ can be expressed in the following way.

$$F_{em} = D_{em}\frac{dx}{dt} \tag{7}$$

There are two main designs of coils. The conventional way to construct a coil is by winding copper wire around a cylinder [5, 6, 18, 19]. This is difficult to miniaturize. For this reason, micro-fabricated planar coils have become increasingly popular for micro-EHs. An example of a microfabricated planar coil can be seen in Figure 15. Many examples of microfabricated coils in EHs have been explored [13, 37].

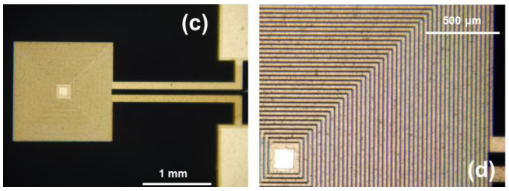

Fig. 15: Images of a micro-fabricated planar coil. (Courtesy of Podder et al. (2015) [38])

The first implementation of electromagnetic energy harvesters (EMEHs) in watches is the Seiko Automatic Generation System (AGS) as seen in Figure 16 below. The Seiko AGS EH uses an eccentric mass that rotates as a result of the applied accelerations. This rotation is amplified utilizing a gear train by a factor of 100 and is transmitted to a magnet rotating next to a coil.

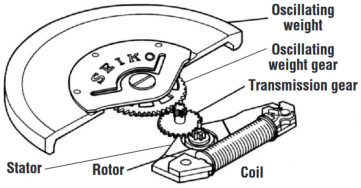

Fig. 16: Schematic of the Seiko Automatic Generation System (AGS) EH. (Courtesy of Paradiso and Starner (2005) [39])

2) Electrostatic transduction: Electrostatic energy harvesters (ESEH) are EHs that use a change in capacitance of a variable capacitor to generate a potential difference.

There are broadly two different ways to operate an ESEH; switched mode or continuous electret mode [34]. In switched mode, the ESEH is a passive device that requires an energy

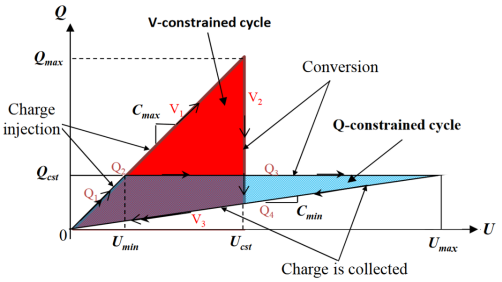

Fig. 17: Standard energy conversion cycles for electret-free electrostatic devices. The voltage-constrained cycle is shown in red and the charge-constrained cycle is shown in blue. (Courtesy of Boiseseau et al. (2012) [34])

cycle to convert mechanical energy into electricity. Many such cycles can be envisioned, but the two most common are defined as charge-constrained and voltage-constrained, demonstrated by the voltage-charge plane in Figure 17.

The relation between charge Q, voltage U and capacitance C is shown in Equation 8 below.

$$Q = U \cdot C \tag{8}$$

A step in the Q-U cycle with constant capacitance results in a straight line with the magnitude of the derivative being equal to the capacitance during that step.

In the charge-constrained cycle, the structure is polarized when its capacitance is maximum (C_{max}). An electric charge is stored in the capacitor at a predefined voltage (U_{min}). When no charge can flow in or out, the structure moves away, decreasing the capacitance. As the capacitance decreases, the voltage increases as the charge is constant. The reservoir does not provide any energy during this step (Q3) as all the energy gained in the system comes from mechanical energy. At this step, the energy can be removed from the structure and the cycle can restart. The maximum energy that can be harvested per cycle is equal to the area enclosed by the Q-U-cycle and is equal to ΔE as can be seen in Equation 9 [40].

$$\Delta E = \frac{1}{2}\Delta C U_{min} U_{max} \tag{9}$$

Where ΔC is the difference between the minimum and maximum capacitance in the cycle, U_{min} is the minimum voltage during the cycle, and U_{max} is the maximum voltage during the cycle.

In the voltage-constrained cycle, the structure is polarized when its capacitance is maximum with a high voltage. The structure is then moved to a lower capacitance whilst the voltage is kept constant by an external power source. Because the voltage is kept constant and the capacitance decreases, the charge of the capacitor increases, generating a current that can be scavenged. After the capacitance reaches its minimal state, the charge can be collected and stored. The maximum energy that can be harvested per cycle is equal to ΔE as can be seen in Equation 10, which is higher than the maximum energy that can be collected during the charge-constrained cycle [40].

$$\Delta E = \frac{1}{2}\Delta C U_{max}^2 \tag{10}$$

Where ΔC is the difference between the minimum and maximum capacitance in the cycle, and U_{max} is the maximum voltage during the cycle. The voltage-constrained cycle needs an external power source to polarize the structure when the capacitance is maximum.

A way to achieve direct mechanical to electrical conversion without the need for energy cycles is by using an electret-based ESEH. An electret is the electrostatic equivalent of a magnet. Electrets contain a quasi-permanent embedded charge. The electret is used to induce charges on an electrode, which allows for an energy cycle that does not require an energy source to polarize the structure. The structure deformation induces an output voltage directly.

When making an electret, a dielectric layer is charged. The most common method is charging through means of corona discharge. Corona discharge is a process in which a strong electric field generates ions that are projected onto the dielectric layer, thus transferring charge [34]. An advantage of electrets is that the polarization voltage can be very high, on the order of 100s of Volts, with the dielectric breakdown imposing an ultimate limit on the stable charge of all electrets [41]. The continuous power generated by an electret energy harvester is dependent on multiple factors, but scales according to the following relation.

$$P \propto \frac{dC}{dt} U_s^2 \tag{11}$$

Where P is the power generated, $\frac{dC}{dt}$ is the instantaneous change in capacitance and U_s is the electret surface voltage. Besides the operation methods that can be used to generate energy using ESEHs, there are also several capacitor shapes that can be used with their own advantages and disadvantages. The most common capacitor shapes are shown in Figure 18.

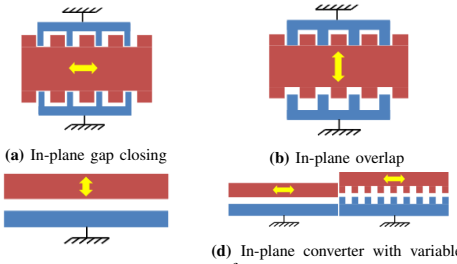

(a) In-plane gap closing

(b) In-plane overlap

(c) Out-of-plane gap closing

(d) In-plane converter with variable surface

Fig. 18: Basic capacitor shapes that can be used in ESEHs. In the schematic, blue represents the stator and red represents the mover. The yellow arrows indicate the movement direction. (Courtesy of Boisseau et al. (2012) [34])

In Table II, the main advantages and drawbacks of the different capacitor shapes are shown. As can be seen, the best capacitor architecture depends on many factors and is specific for each EH.

TABLE II: Advantages and drawbacks of the four different capacitor shapes.

Capacitor shape	Advantage	Drawback
in-plane gap closing	-Simple fabrication -High power density	-Small displacement range
in-plane overlap	-Simple fabrication	-Sensitive to stability issues [40]
out-of-plane gap closing	-Simple electret application -Small influence of parasitic capacitances	-Non-planar fabrication -High influence of viscous damping
in-plane with variable surface	-Very large displacement range -Simple electret application	-Non-planar fabrication

Another consideration for EHs is the electrostatic force variation. The electrostatic force variation for out-of-plane, in-plane overlap, and in-plane gap closing capacitors can be seen in Table III below, where F_e is the electrostatic force and z is the displacement of the mover. This electrostatic force variation can add electrostatic stiffness to the ESEH, changing the dynamics of the system, and should therefore be taken into account in the mechanical design.

TABLE III: Electrostatic force variation for different system configurations. (Courtesy of [42])

Structure	Q constrained	V constrained
Out-of-plane	F_e constant	$F_e \sim 1/z$
In-plane overlap	$F_e \sim 1/z^2$	F_e constant
In-plane gap closing	$F_e \sim z$	$F_e \sim 1/z^2$

3) Piezoelectric transduction: Piezoelectricity is a property of certain crystalline materials such as quartz that gemerate electricity when pressure is applied. This is called the direct piezoelectric effect. Piezoelectric materials undergo deformation when an electric field is applied, which is termed the converse effect. The converse effect can be used as an actuator, and the direct effect can be used as a transducer [43]. The direct electromechanical behavior of piezoelectric materials can be modeled by the following constitutive equation [44].

$$D = dT + \epsilon E \tag{12}$$

where D is electrical displacement, d piezoelectric coefficient, T stress, ϵ permittivity of the material, and E electric field. Piezoelectric transduction has drawn significant attention due to its simplicity in structure, high energy density, and good compatibility with microfabrication methods [45, 46].

The most common method of piezoelectric energy harvesting is utilizing a cantilever beam with a proof mass attached on the end, as demonstrated in Figure 19. A piezoelectric layer is attached on one side (unimorph), or both sides (bimorph), of the cantilever. When accelerations are applied to the base, the proof mass moves, bending the cantilever and thus applying stress. This stress induces a charge in the piezoelectric layer.

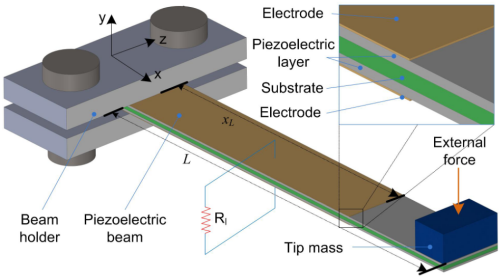

Fig. 19: Schematic diagram of a general bimorph piezoelectric energy harvester with a substrate and two electrodes. (Courtesy of Fu et al. (2018) [47])

Piezoceramics are most used in energy harvesting applications for their high electromechanical coupling factor. The electromechanical coupling factor is an indicator of the effectiveness with which a piezoelectric material converts electrical energy into mechanical energy [48]. Piezoceramics are characterized by their large dielectric and piezoelectric coefficients, and electromechanical coupling factors, as well as their high energy conversion rates. However, they are very brittle so they cannot absorb large strains without being damaged [49]. More flexible piezopolymers can be used, but this comes at a cost of lower electromechanical coupling [50].

D. Harvester performance

Evaluating and comparing the performance of EHs is not a straightforward task. Several figures of merit (FoM) are proposed in the existing research that can be used in the evaluation. One of the most widely used FoM is power density [51]. The power density of an EH is defined as the power generated per volume of the EH as mentioned in section II-B. The problem with this metric is that the power that an EH generates is very dependent on the environment it operates in. To solve part of this issue, the normalized power density (NPD) can be used as an FoM as introduced by Beeby et al. (2007) [52]. The NPD can be determined by calculating the power density and dividing it by the maximum acceleration applied squared. This takes away the dependency of the power output on the amplitude/acceleration of the vibrations. This still leaves environmental influences such as the frequency unaccounted for. For this reason, another FoM has been introduced that is now widely used. This FoM is the harvester effectiveness η_h [11] as mentioned in section I. The harvester effectiveness compares the power output of the EH with the theoretically maximum power harvested and is a function of the input vibrations and the EH dimensions and proof mass weight.

Thus far, EH principles have been characterized and discussed according to theory. In this section, an effort is made to determine whether reported EHs in the literature follow expectations. This is done by comparing EHs reported

in existing research according to the key parameters outlined in section II-B. 19 EHs reported in the literature have been used for the comparison and the result can be seen in Table IV below. The EHs are characterized in the table according to the framework outlined in section III. Only EHs that have been experimentally validated have been considered, and also only those that contain enough information to be able to determine the FoMs.

TABLE IV: Performances of experimentally verified EHs reported in literature.

Reference	Transduction method	Inertial/ non-inertial	Rotational/ translational	DoF	Bandwidth improvement	Power harvested RMS [μW]	Volume [cm^3]	Maximum possible energy harvested [μW]	Power density [$\mu W/cm^3$]	Normalized power density [$\mu W/cm^3/g^2$]	Motion ratio [-]	Harvester effectiveness [-]
[12]	Piezoelectric	Non-inertial	Rotational	multiple	magnetic plucking FupC	20.0	3.3	612	6.0	-		0.033
[16]	Piezoelectric	Inertial	Translational	1	Neutral stability & Hard end-stops	350.0	32.4	7670	10.8	1	0.034	0.04563
[53]	Piezoelectric	Inertial	Translational	1	-	2.09	0.002169	163.29	963.7	154	500.000	0.01280
[17]	Piezoelectric	Inertial	Translational	multiple	impact FupC	1530.0	16.4	2477.85	93.2	583	2.540	0.61747
[17]	Piezoelectric	Inertial	Translational	1	-	290.0	21.3	9230.91	13.6	85	8.475	0.03142
[54]	Piezoelectric	Inertial	Translational	1	-	40	16.57	1278.13	2.4	60	104.310	0.03130
[18]	Electromagnetic	Inertial	Translational	1	Neutral stability & Soft end-stops	284.0	6.3	6080	45.3	155	4.980	0.047
[5]	Electromagnetic	Inertial	Rotational	1	Neutral stability	10400.0	33.1	616380.5	314.2	140	infinite	0.017
[55]	Electromagnetic	Inertial	Rotational	1	-	61.3	3.5	2791.6	17.5	-	infinite	0.022
[37]	Electromagnetic	Inertial	Translational	1		0.61	0.205	3.58	3.0	1	3.065	0.171
[6]	Electromagnetic	Inertial	Tranlsational	multiple	Neutral stability & Soft end-stops & Impact FupC	203.0	3.90	5425.38	52.1	13	0.065	0.037
[19]	Electromagnetic	Inertial	Rotational	1	Hard end-stops	3000	10	60513.01	287.8	12	0.198	0.050
[56]	Electrostatic	Inertial	Translational	1	-	1.2	0.02	87.29	60.0	6	54.371	0.014
[57]	Electrostatic	Inertial	Translational	1	-	1	0.0015	3.76	866.7	21	13.197	0.346
[57]	Electrostatic	Inertial	Translational	1	-	1	0.0015	7.51	866.7	5	6.599	0.173
[7]	Electrostatic	Inertial	Translational	1	Neutral stability & Hard end-stops	-	0.1	6.20	-	-	0.000	-
[20]	Electrostatic	Inertial	Translational & Rotational	multiple	Neutral stability & Hard end-stops	45.3	1	1937.89	45.3	7	0.000	0.023
[21]	Electrostatic	Inertial	Translational	1	-	2.2	0.038	10.98	57.9	58	1.630	0.200
[22]	Electrostatic	Inertial	Translational	1	Neutral stability & Hard end-stops	0.2	0.3	56.34	0.7	0	0.030	0.004

IV. Discussion

The results will be discussed according to the same categorization presented in section III.

A. Mechanical design

Evaluating the performance of the mechanical design is split up based on the same subdivision as presented in Figure 3 and used in section III-A.

1) Inertial/non-inertial: Inertial EHs have superior useability in a wider range of applications due to the flexibility of requiring one point of contact with the source. This also allows a greater degree of miniaturization [3]. Non-inertial EHs require two points of contact. This makes non-inertial EHs unappealing for an EH incorporated in a quartz watch, as the EH will be contained within the device and thus there are no two structures that can move relative to one another. For the forenamed reasons, inertial EHs are seen as preferable for quartz watch applications.

2) Rotational/translational: Rotational EHs have the advantage of having a potentially infinite inertial displacement. They can harvest energy from input accelerations from an entire plane and rotations, instead of just from one direction as is the case with most translational EHs. The disadvantage is that because of the large displacements, a compliant suspension is not possible when taking advantage of the infinite internal motion range for rotational EHs. To solve this, micro-bearings have to be implemented. Micro-bearings are difficult and expensive to fabricate, subject to wear, and have large tolerances. Due to the need for a more complex connection to the device, rotational EHs perform worse on miniaturization, as can be seen in Figure 22. The upside of this large internal displacement ratio is a theoretically larger power density, although this could not be verified using the data collected from the reported EHs in existing research. Rotational EHs also have the benefit of easily being made neutrally stable, increasing their bandwidth. An example of a rotational EH that has a neutrally stable eccentric mass can be seen in Figure 16.

B. Bandwidth improvement

1) Frequency up-conversion: FupC has been shown to increase the bandwidth of EHs considerably and is thus a good candidate for achieving high efficiency at low frequencies. Impact and Plucking FupC are discussed separately.

a) Plucking: Plucking FupC can achieve high normalized bandwidth whilst keeping a high efficiency when properly designed [10]. The two reported methods of achieving plucking FupC are magnetic interaction and using contact. Magnetic plucking is preferred as contact increases friction and wear and leads to lower efficiency. Magnetic plucking does pose a problem in terms of miniaturization as magnets have to be embedded into the EH.

b) Impact: With impact FupC, a large part of the energy that is contained in the proof mass is dissipated by the impact. This results in a low efficiency [10]. For this reason, plucking FupC is seen as preferable.

2) sDoF methods:

a) Resonance tuning: In resonance tuning, a distinction was made between open-loop and closed-loop configurations.

Open-loop configurations are impractical and do not comply with the 'install and forget' benefits of EHs. For quartz watches especially, open-loop configurations are not possible. Closed-loop configurations are more practical but require advanced measurement and actuation methods. Those EHs have a more complex design and a lower overall efficiency for the active case.

More importantly, resonance tuning is only useful when the input motion has one dominant frequency. When the input energy is highly stochastic, as is the case with human motion, resonance tuning is close to useless to increase efficiency.

b) End-stops: End-stops are an effective method to increase the bandwidth of EHs, increasing the normalized bandwidth by a factor of 10-100 [10]. The downside of end-stops is that part of the kinetic energy of the proof mass is dissipated in the impact with the end-stop. This effect is smaller when soft-stops are used, and reduced to nearly zero when magnetic soft-stops are used. For miniaturized EHs, magnetic soft-stops are impractical due to their relatively large size, but soft-stops in the form of microfabricated springs have been reported in literature, as is shown in Figure 20.

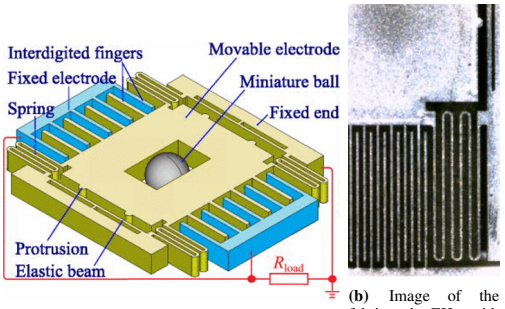

(a) Schematic of an ESEH utilizing soft-stops

(b) Image of the fabricated EH with the soft-stop shown at the top right.

Fig. 20: Example of an EH reported in literature that uses soft-stops. (Courtesy of Lu et al. (2015) [58])

c) Transmission: Multiple EHs that use transmission have been reported, and the first EHs used for quartz watches employ transmission as can be seen in Figure 16. The drawback of using a transmission is that the gears take up a large volume, are expensive to manufacture, and generate friction and thus dissipate energy. This also causes the transmission to be subject to wear and tear, limiting the lifetime.

d) Multi-stability: An extensive review of these multi-stability methods was made by Pellegrini et. al [59]. The review concludes that multi-stable EHs are capable of coping with vibrations of frequencies much lower than typical resonance frequencies, outweighing the increased complexity of the design. This makes multi-stability an attractive method to increase the efficiency of broadband energy harvesting.

e) Neutral stability: There are several reported ESEH designs that successfully implement neutral stability in their design. Most notably the rolling designs from [7, 32], or an unconstrained proof mass in a box [22]. Although these EHs exhibit a large bandwidth and a high energy density, they lack in the ease of fabrication and assembly, and are highly sensitive to wear. When the proof mass is underconstrained, end-stops are also generally necessary for neutrally stable EHs. Employing negative stiffness to achieve neutrally stable EHs can be a promising alternative to achieve zero-stiffness whilst still having a monolithic, easy-to-fabricate design. Statically balanced MEMS have already been proposed by Tolou et. al, but not yet applied in EHs [31].

C. Transduction methods

1) Electromagnetic transduction: Electromagnetic transduction is the most well-established method for energy harvesting and has been used for quartz watch applications for decades. EMEHs offer a robust method to achieve high power densities but have several drawbacks. The voltage output of EMEHs is typically very low, which results in the need for transformers. This increases losses and increases the size of the device. EMEHs are also difficult to scale down due to the need for coils, integrated permanent magnets, and ferromagnetic materials for the flux path. This means that miniaturization is still a big challenge for EMEHs.

Planar microfabricated coils exist, but as the voltage generated scales quadratically with the number of coil turns, and as planar coils are a 2D planar technology, as opposed to the wire-winding 3D technology, the amount of turns that can be achieved is limited. This limits the voltage generated. Another downside is that the electromechanical damping scales proportionally with the number of coil turns squared, divided by the resistance of the coil wire as follows.

$$D_{em} \propto \frac{N^2}{R_C} \tag{13}$$

As the resistance of the coil wire for planar coils increases quadratically for each turn due to the increasing radius, the overall electromechanical coupling is decreased. This effect is smaller for wire-winding coils as the radius of the coil is constant and the electromagnetic damping is thus independent of the number of turns.

In Seiko's AGS EH, a gear train is used to amplify the rotational velocity to increase the voltage. This increases the volume of the device and also increases the cost of fabrication. However, the main problem is that the voltage generated when the eccentric mass rotates below a certain rotational velocity is too low for any power to be left after power processing. The generated potential would be AC voltages that need to be rectified to be used as a power source for electronics. To rectify the voltages, they would have to be transformed up to the range of two to several Volts, necessitating a transformer with a conversion ratio on the order of 100 [40]. Such a transformer in turn increases the volume of the EH drastically. The average power that can be generated using the Seiko AGS system has been determined to be 0.5 μW during daily use [60]. This is lower than the energy consumption of a quartz watch as stated in section I.

2) Electrostatic transduction: Electrostatic energy harvesting is an attractive solution as the output voltages generated are high and can be adjusted straightforwardly by varying the load cycle for electret-free ESEHs, or the electret charge for electret-based ESEHs. ESEHs perform well because of their high electromechanical coupling and their compatibility with microfabrication methods, making them a cost-effective method to produce miniaturized EHs.

Electret-free ESEHs need an energy cycle to generate energy which results in the need for complex control through electronic circuits, and an external power source to start the energy cycle. Electrets can solve this issue but come with their own drawbacks of increased cost of fabrication, complex handling, and stability issues.

Several microfabrication compatible electret materials exist, such as CYTOP and silicon-based inorganic electrets. These materials solve most of the issues related to electrets. Their high charge stability and compatibility with IC and micromachining technologies make them an excellent candidate for ESEHs [61].

In terms of fabrication, in-plane gap closing and in-plane overlap converters are the most simple as they exist of simple planar structures. Roundy (2003) [40] has shown that by making realistic assumptions about dimensions based on fabrication technology and parasitic capacitances, an estimate can be made for the maximum power density that can be achieved. This analysis demonstrated that the performance of in-plane gap closing EHs had superior performance. However, it should be noted that the in-plane patterned capacitance structure was not taken into account in the analysis. Furthermore, the result is not necessarily the same for any EH design as the mechanical design has a large effect on performance.

3) Piezoelectric transduction: Piezoelectric energy harvesting offers high energy densities, making it an attractive energy harvesting solution. Piezoelectric devices provide high voltages and low currents. Modeling and experiments performed by Roundy show that voltages in the range of two to several volts and currents on the order of tens to hundreds of micro-amps are easily obtainable [40]. Therefore, like electrostatic converters, one of the advantages of piezoelectric conversion is the direct generation of appropriate voltages. Another advantage is that separate voltage source is needed to initiate the conversion process, as is the case for electret-free ESEHs.

A drawback of piezoelectric conversion is the difficulty of

miniaturization and integration with microelectronics. While it is true that piezoelectric thin films can be microfabricated [62, 63], this greatly reduces the piezoelectric coupling [63, 64]. The piezoelectric coupling is a unitless quantity that is used to compare the efficiency of different piezoelectric materials in converting mechanical energy to electrical energy. PZT-based thin-films, one of the most widely used piezoelectric materials, contain a high percentage of lead (Pb). This toxic element prevents their employment in biomedical devices and their large diffusion due to environmental concerns [62]. For these reasons, the miniaturized PEHs in quartz watches have several problems that need to be overcome before they can be integrated into quartz watches.

D. Harvester performance

An effort is made to quantitatively compare EHs using the data of the harvesters that are presented in Table IV. The results are plotted in Figure 21, Figure 22 and Figure 23. Each dot in the graph represents an EH.

In Figure 21, the volume and effectiveness are plotted for the three transduction methods. What can be concluded is that ESEHs excel for small volumes, achieving similar effectiveness for volumes on the order of 10-100 times smaller than their EMEH and PEH counterparts. This agrees with the expectations based on the theory.

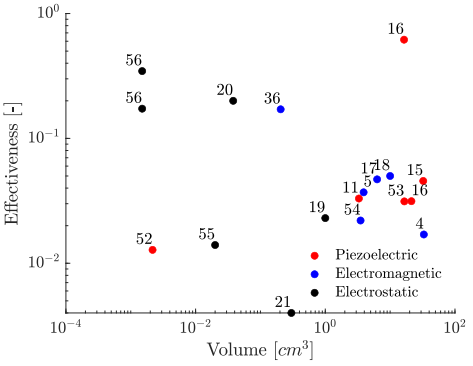

Fig. 21: The volume and effectiveness of the energy harvesters analyzed in Table IV categorized based on their transduction method.

In Figure 22, the volume and effectiveness are plotted for rotational and translational EHs. What can be concluded is that translational EHs perform better on miniaturization and effectiveness. This is due to the fact that the rotational EHs make use of their large internal displacement, resulting in a non-monolithic design. This design is less efficient in terms of volume as components such as bearings need to be included.

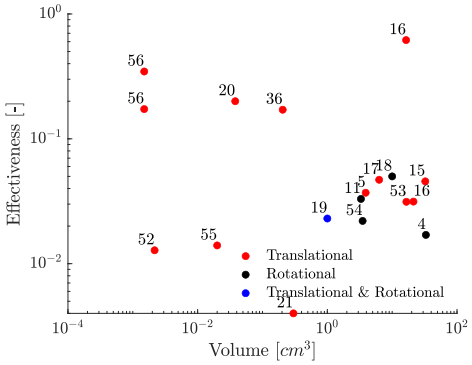

Fig. 22: The volume and effectiveness of rotational and translational energy harvesters analyzed in Table IV.

In Figure 23, the NPD and effectiveness are plotted for the three transduction methods. The resulting analysis shows that there is no clear relation between the two FoMs.

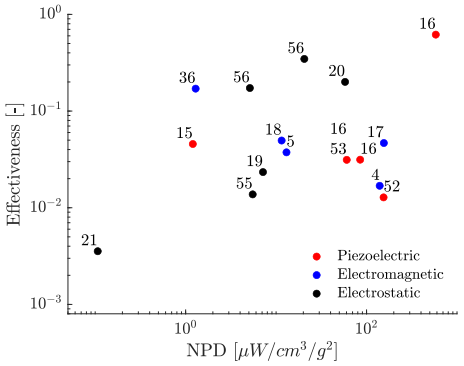

Fig. 23: The NPD and volume of different transduction mechanisms energy harvesters analyzed in Table IV.

V. Conclusion

Energy harvesting is an area of research that has been investigated thoroughly, and numerous physical principles, designs, and applications have been theorized and experimentally verified. A number of key parameters have been presented in this paper that can be used to compare the performance of energy harvesting principles and designs for the application of quartz watches.

A framework is presented that is used to categorize EHs. EHs found in the literature are subdivided based on their working principles and design according to the framework, and subsequently compared.

For quartz watch applications, inertial energy harvesting should be used. Rotational and translational inertial EHs each have their own advantages and disadvantages. Rotational EHs have a higher theoretical maximum energy due to

their infinite internal displacement and can harvest energy from motions in multiple DoFs. Translational EHs allow for a monolithic design which would aid miniaturization and decrease friction, and thereby the resulting wear.

For the transduction method, electret-based transducers look most promising due to their direct mechanical to electrical transduction, the recent improvements in charge stability, and microfabrication compatibility of electret-based transducers.

Due to the stochastic low-frequency nature of human motion, bandwidth improvement methods have to be employed. Based on the analysis, FupC is less promising due to the complex design, low efficiency of impact FupC, and limited miniaturization possibilities of plucking FupC. Instead, sDoF methods should be used. Of the sDoF bandwidth improvement methods, soft-stops, multi-stability, and neutral stability look the most promising. This is due to their volume effectiveness, large bandwidth improvement, and simple design. The most appropriate sDoF bandwidth improvement method also depends on aspects of the mechanical design such as the displacement orientation and the suspension method.

REFERENCES

[1] T. Fernández-Caramés and P. Fraga-Lamas, "Towards the internet of smart clothing: A review on iot wearables and garments for creating intelligent connected e-textiles," vol. 7, p. 405, 12 2018.

[2] A. Mohanty, S. Parida, R. Behera, and T. Roy, "Vibration energy harvesting; a review," *Journal of Advanced Dielectrics*, vol. 9, 08 2019.

[3] P. D. Mitcheson, E. M. Yeatman, G. K. Rao, A. S. Holmes, and T. C. Green, "Energy harvesting from human and machine motion for wireless electronic devices," *Proceedings of the IEEE*, vol. 96, pp. 1457–1486, 2008.

[4] "Watch batteries," 2016.

[5] H. Liu, C. Hou, J. Lin, Y. Li, Q. Shi, L. Sun, and C. Lee, "A non-resonant rotational electromagnetic energy harvester for low-frequency and irregular human motion," *Applied Physics Letters*, vol. 113, p. 203901, 11 2018.

[6] M. A. Halim, H. Cho, M. Salauddin, and J. Y. Park, "A miniaturized electromagnetic vibration energy harvester using flux-guided magnet stacks for human-body-induced motion," *Sensors and Actuators A: Physical*, vol. 249, pp. 23–31, 2016.

[7] M. Kiziroglou, C. He, and E. Yeatman, "Non-resonant electrostatic energy harvesting from a rolling mass," pp. 318 – 321, 07 2008.

[8] A. Erturk and D. Inman, "Broadband piezoelectric power generation on high-energy orbits of the bistable duffing oscillator with electromechanical coupling," *Journal of Sound and Vibration*, vol. 330, no. 10, pp. 2339–2353, 2011. Dynamics of Vibro-Impact Systems.

[9] D. Qiao, G. Pang, M. Kit, and D. Lam, "A new pcb-based low-cost accelerometer for human motion sensing," pp. 56 – 60, 10 2008.

[10] T. W. Blad and N. Tolou, "On the efficiency of energy harvesters: A classification of dynamics in miniaturized generators under low-frequency excitation," *Journal of Intelligent Material Systems and Structures*, vol. 30, no. 16, pp. 2436–2446, 2019.

[11] S. Roundy, "On the effectiveness of vibration-based energy harvesting," *Journal of Intelligent Material Systems and Structures*, vol. 16, pp. 809–823, 10 2005.

[12] H. Fu and E. M. Yeatman, "A methodology for low-speed broadband rotational energy harvesting using piezoelectric transduction and frequency up-conversion," *Energy*, vol. 125, no. C, pp. 152–161, 2017.

[13] M. Halim, R. Rantz, Q. Zhang, L. Gu, K. Yang, and S. Roundy, "An electromagnetic rotational energy harvester using sprung eccentric rotor, driven by pseudo-walking motion," *Applied Energy*, vol. 217, pp. 66–74, 2018.

[14] E. Yeatman, "Energy harvesting from motion using rotating and gyroscopic proof masses," *Proceedings of The Institution of Mechanical Engineers Part C-journal of Mechanical Engineering Science - PROC INST MECH ENG C-J MECH E*, vol. 222, 01 2008.

[15] H. Fu, X. Mei, D. Yurchenko, S. Zhou, S. Theodossiades, K. Nakano, and E. M. Yeatman, "Rotational energy harvesting for self-powered sensing," *Joule*, vol. 5, no. 5, pp. 1074–1118, 2021.

[16] K. Fan, Z. Liu, H. Liu, L. Wang, Y. Zhu, and B. Yu, "Scavenging energy from human walking through a shoe-mounted piezoelectric harvester," *Applied Physics Letters*, vol. 110, p. 143902, 04 2017.

[17] L. Gu, "Low-frequency piezoelectric energy harvesting prototype suitable for the mems implementation," *Microelectron. J.*, vol. 42, pp. 277–282, 2011.

[18] H. Liu, S. Gudla, F. A. Hassani, C.-H. Heng, Y. Lian, and C. Lee, "Investigation of the nonlinear electromagnetic energy harvesters from hand shaking," *IEEE Sensors Journal*, vol. 15, pp. 2356–2364, 2015.

[19] M. Geisler, S. Boisseau, P. Gasnier, J. Willemin, C. Gobbo, G. Despesse, I. Ait-Ali, and S. Perraud, "Looped energy harvester for human motion," *Smart Materials and Structures*, vol. 26, 08 2017.

[20] H. C.-H. K. H.-D. . Y. J.-B. Choi, Dong-Hoon, "Liquid-based electrostatic energy harvester with high sensitivity to human physical motion.," *Smart Materials and Structures*, vol. 20, 2011.

[21] P. Basset, D. Galayko, F. Cottone, R. Guillemet, E. Blokhina, F. Marty, and T. Bourouina, "Electrostatic vibration energy harvester with combined effect of electrical nonlinearities and mechanical impact," *Journal of Micromechanics and Microengineering*, vol. 24, 02 2014.

[22] L. Bu, X. Wu, X. Wang, and L. Liu, "Non-resonant electrostatic energy harvester for wideband applications," *Micro & Nano Letters*, vol. 8, no. 3, pp. 135–137, 2013.

[23] M. A. Halim and J. Y. Park, "Theoretical modeling and analysis of mechanical impact driven and frequency up-converted piezoelectric energy harvester for low-frequency and wide-bandwidth operation," *Sensors and Actuators A: Physical*, vol. 208, pp. 56–65, 2014.

[24] C. Eichhorn, F. Goldschmidtboeing, and P. Woias, "Bidirectional frequency tuning of a piezoelectric energy converter based on a cantilever beam," *Journal of Micromechanics and Microengineering*, vol. 19, p. 094006, 08 2009.

[25] E. Leland and P. Wright, "Resonance tuning of piezoelectric vibration energy scavenging generators using compressive axial preload," *Smart Materials and Structures*, vol. 15, p. 1413, 09 2006.

[26] I. Ayala, D. Zhu, M. Tudor, and S. Beeby, "A tunable kinetic energy harvester with dynamic over range protection," *Smart Materials and Structures*, vol. 19, p. 115005, 09 2010.

[27] B. Truong, C. Le, and E. Halvorsen, "Experimentally verified model of electrostatic energy harvester with internal impacts," vol. 2015, 01 2015.

[28] R. Ai, L. L. S. Monteiro, P. C. C. Monteiro, P. M. C. L. Pacheco, and M. A. Savi, "Piezoelectric vibration-based energy harvesting enhancement exploiting nonsmoothness," *Actuators*, vol. 8, no. 1, 2019.

[29] H. Vocca, I. Neri, F. Travasso, and L. Gammaitoni, "Kinetic energy harvesting with bistable oscillators," *Applied Energy*, vol. 97, pp. 771–776, 2012. Energy Solutions for a Sustainable World - Proceedings of the Third International Conference on Applied Energy, May 16-18, 2011 - Perugia, Italy.

[30] B. Andò, S. Baglio, A. Bulsara, and V. Marletta, "A bistable buckled beam based approach for vibrational energy harvesting," *Sensors and Actuators A: Physical*, vol. 211, pp. 153–161, 2014.

[31] N. Tolou, J. Gallego Sanchez, and J. Herder, "Statically-balanced compliant micromechanisms," *Mikroniek*, vol. 50, pp. 20–25, 01 2010.

[32] Y. Suzuki, "Recent progress in mems electret generator for energy harvesting," *IEEJ Transactions on Electrical and Electronic Engineering*, vol. 6, no. 2, pp. 101–111, 2011.

[33] J. Zhao, G. Zhen, G. Liu, T. Bu, W. Liu, X. Fu, P. Zhang, C. Zhang, and Z. L. Wang, "Remarkable merits of triboelectric nanogenerator than electromagnetic generator for harvesting small-amplitude mechanical energy," *Nano Energy*, vol. 61, pp. 111–118, 2019.

[34] S. Boisseau, G. Despesse, and B. Seddik, "Electrostatic conversion for vibration energy harvesting," *Intech*, 10 2012.

[35] S. P. Beeby and T. O'Donnell, *Electromagnetic Energy Harvesting*, pp. 129–161. Boston, MA: Springer US, 2009.

[36] A. Batra and A. Alomari, *Power Harvesting via Smart Materials*. 07 2017.

[37] P. Wang, K. Tanaka, S. Sugiyama, X. Dai, X. Zhao, and J. Liu, "A micro electromagnetic low level vibration energy harvester based on mems technology," *Microsystem Technologies*, vol. 15, pp. 941–951, 2009.

[38] P. Podder, P. Constantinou, D. Mallick, and S. Roy, "Silicon mems bistable electromagnetic vibration energy harvester using double-layer

micro-coils," *Journal of Physics: Conference Series*, vol. 660, p. 012124, 12 2015.
[39] J. Paradiso and T. Starner, "Energy scavenging for mobile and wireless electronics," *Pervasive Computing, IEEE*, vol. 4, pp. 18 – 27, 02 2005.
[40] S. Roundy, "Energy scavenging for wireless sensor nodes with a focus on vibration to electricity conversion," 01 2003.
[41] L. S. McCarty, A. Winkleman, and G. M. Whitesides, "Ionic electrets: electrostatic charging of surfaces by transferring mobile ions upon contact.," *Journal of the American Chemical Society*, vol. 129 13, pp. 4075–88, 2007.
[42] G. Despesse, J. Chaillout, T. Jager, J.-M. Leger, A. Vassilev, S. BASROUR, and B. Charlot, "High damping electrostatic system for vibration energy scavenging," pp. 283–286, 10 2005.
[43] H. S. Kim, J.-H. Kim, and J. Kim, "A review of piezoelectric energy harvesting based on vibration," *International Journal of Precision Engineering and Manufacturing*, vol. 12, 12 2011.
[44] A. Jain, P. K. J., A. K. Sharma, A. Jain, and R. P.N, "Dielectric and piezoelectric properties of pvdf/pzt composites: A review," *Polymer Engineering & Science*, vol. 55, no. 7, pp. 1589–1616, 2015.
[45] K. Fan, J. Chang, F. Chao, and W. Pedrycz, "Design and development of a multipurpose piezoelectric energy harvester," *Energy Conversion and Management*, vol. 96, pp. 430–439, 2015.
[46] S. Roundy and P. K. Wright, "A piezoelectric vibration based generator for wireless electronics," *Smart Materials and Structures*, vol. 13, pp. 1131–1142, 2004.
[47] H. Fu, G. Chen, and N. Bai, "Electrode coverage optimization for piezoelectric energy harvesting from tip excitation," *Sensors*, vol. 18, p. 804, 03 2018.
[48] Q.-M. Wang, X.-H. Du, B. Xu, and L. Cross, "Electromechanical coupling and output efficiency of piezoelectric bending actuators," *IEEE Transactions on Ultrasonics, Ferroelectrics, and Frequency Control*, vol. 46, no. 3, pp. 638–646, 1999.
[49] N. Sezer and M. Koç, "A comprehensive review on the state-of-the-art of piezoelectric energy harvesting," *Nano Energy*, vol. 80, p. 105567, 2021.
[50] H. S. Kim, J.-H. Kim, and J. Kim, "A review of piezoelectric energy harvesting based on vibration," *International Journal of Precision Engineering and Manufacturing*, vol. 12, 12 2011.
[51] X. Cao, W.-J. Chiang, Y.-C. King, and Y. Lee, "Electromagnetic energy harvesting circuit with feedforward and feedback dc–dc pwm boost converter for vibration power generator system," *Power Electronics, IEEE Transactions on*, vol. 22, pp. 679 – 685, 04 2007.
[52] S. P. Beeby, R. N. Torah, M. Tudor, P. Glynne-Jones, T. O'Donnell, C. Saha, and S. Roy, "A micro electromagnetic generator for vibration energy harvesting," *Journal of Micromechanics and Microengineering*, vol. 17, pp. 1257–1265, 2007.
[53] B.-S. Lee, S. C. Lin, W.-L. Wu, X. yu Wang, P.-Z. Chang, and C.-K. Lee, "Piezoelectric mems generators fabricated with an aerosol deposition pzt thin film," *Journal of Micromechanics and Microengineering*, vol. 19, p. 065014, 2009.
[54] L. Dhakar, H. Liu, F. E. H. Tay, and C. Lee, "A new energy harvester design for high power output at low frequencies," *Sensors and Actuators A-physical*, vol. 199, pp. 344–352, 2013.
[55] M. Halima, R. Rantza, Q. Zhangb, L. Gub, K. Yangb, and S. Roundya, "An electromagnetic rotational energy harvester using sprung eccentric rotor , driven by pseudo-walking motion," 2018.
[56] J. Oxaal, M. M. Hella, and D.-A. Borca-Tasciuc, "Electrostatic mems vibration energy harvester for hvac applications with impact-based frequency up-conversion," *Journal of Micromechanics and Microengineering*, vol. 26, p. 124012, 2016.
[57] D. Hoffmann, B. Folkmer, and Y. Manoli, "Fabrication, characterization and modelling of electrostatic micro-generators," *Journal of Micromechanics and Microengineering*, vol. 19, p. 094001, 2009.
[58] Y. Lu, F. Cottone, S. Boisseau, F. Marty, D. Galayko, and P. Basset, "A nonlinear mems electrostatic kinetic energy harvester for human-powered biomedical devices," *Applied Physics Letters*, vol. 107, no. 25, p. 253902, 2015.
[59] S. P Pellegrini, N. Tolou, M. Schenk, and J. Herder, "Bistable vibration energy harvesters: A review," *Journal of Intelligent Material Systems and Structures*, vol. 24, pp. 1303–1312, 07 2013.
[60] G. Görge, M. Kirstein, and R. Erbel, "Microgenerators for energy autarkic pacemakers and defibrillators: Fact or fiction?," *Herz*, vol. 26, pp. 64–68, 2001.
[61] V. Leonov and C. Van Hoof, "Multilayer inorganic electrets with sio2 and si3n4 layers for applications on heated machinery," *Smart Materials Research*, vol. 2012, p. 904168, 05 2012.
[62] M. T. Todaro, F. Guido, V. Mastronardi, D. Desmaele, G. Epifani, L. Algieri, and M. De Vittorio, "Piezoelectric mems vibrational energy harvesters: Advances and outlook," *Microelectronic Engineering*, vol. 183-184, pp. 23–36, 2017.
[63] I. Kanno, "Piezoelectric MEMS for energy harvesting," vol. 660, p. 012001, dec 2015.
[64] R. Abdolvand, H. Fatemi, and S. Moradian, *Quality Factor and Coupling in Piezoelectric MEMS Resonators*, pp. 133–152. Cham: Springer International Publishing, 2017.

3

CONCEPT DESIGN

In this chapter, several micro-electret transducers are explained in more detail, and a conceptual design for a micro-electret transducer is presented. This concept is further elaborated in chapter 4 and chapter 5.

3.1. VARIABLE CAPACITOR ORIENTATION

As is concluded in chapter 2, electret transduction looks promising for the purpose of micro-energy harvesting for quartz watches. There are a number of different configurations that have been identified that can be used to create variable capacitors, shown in Figure 3.1.

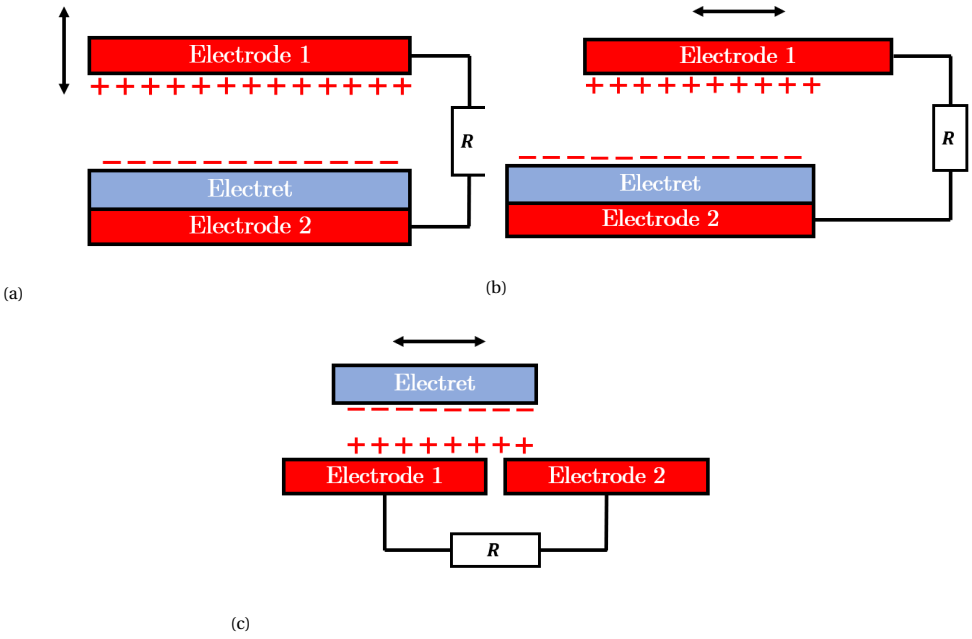

Figure 3.1: Schematic representations of several variable capacitor orientations used in electret transducers. **(a)** Out-of-plane gap closing. **(b)** In-plane variable area. **(c)** Freestanding electret.

In Figure 3.1a, the out-of-plane gap-closing configuration is shown. In Figure 3.1b, the in-plane variable area configuration is shown. Both of these methods use two electrodes that are connected with a load resistance R. An electret is used to induce charge on the electrodes. When the electrodes move relative to one another, the capacitance changes, and thus the charge on the electrodes changes. This charge then moves across the load resistance, dissipating energy.

In Figure 3.1c, the freestanding electret configuration is shown. It is called freestanding, as there are no electrical connections to the electret mover. This transducer works by varying the charge which is induced on the two counter electrodes. As the electret moves, it first induces charge on electrode 1, and then it induces a charge on electrode 2, and vice versa. This induced charge moves across the load resistance, dissipating energy.

The out-of-plane gap closing and the in-plane variable area configurations use electrodes on the mover and the stator. Because of this, signal lines have to be used that are connected to the mover. These signal lines have to withstand the stress of deformation due to the displacement of the mover. With a device lifetime of five years and a fre-

quency of just 1 Hz, the fatigue limit of the signal lines should be larger than 10^8 cycles. Moreover, the signal lines limit the displacement range. As the mover can only move as far as the signal lines allow. From a manufacturing point of view, it is typically difficult to lead out the signal lines from both sides of the device, where additional wiring or 3D structures such as metal stud bumps are demanded [23].

The freestanding electret configuration only has signal lines connected to the stator. The metal signal lines stay static during the movement of the mover and the signal lead-outs are fabricated easily by simple metal patterning. This means that the mover can have a significantly larger displacement than the out-of-plane gap closing or the in-plane variable area electret transducers.

Yeatman has shown that under harmonic excitation motion, the theoretical maximum power harvested by an energy harvester is a function of only a few parameters [24].

$$P_{max} = \frac{1}{2} Y_0 Z_l \omega_s^3 m \tag{3.1}$$

Where P_{max} is the maximum output power, Y_0 is the source motion amplitude, Z_l is the displacement range inside the device, ω_s is the frequency of the source motion, and m is the proof mass. This simple relation shows that the output power of the device scales linearly with the displacement range. Furthermore, it is preferable that the electret transducer can achieve full rotation such that it is compatible with conventional mechanical systems used in quartz watches. Such a design is only possible if the mover is freestanding. Because of the forenamed reasons, the freestanding electret configuration is seen as the most suitable electret transducer for quartz watches.

3.2. FREESTANDING ELECTRET TRANSDUCER

The schematic of the freestanding electret transducer shown in Figure 3.1c only shows one 'unit cell'. To increase the output power of the electret transducer, interdigitated electrode pairs can be used to increase the working frequency of the transducer [20], as the output power of an electret transducer scales linearly with the working frequency of the transducer.

$$P \propto \omega_t = n\omega \tag{3.2}$$

Where P is the output power of the transducer, ω_t is the working frequency of the transducer, n is the number of electrode segments and ω is the rotor frequency.

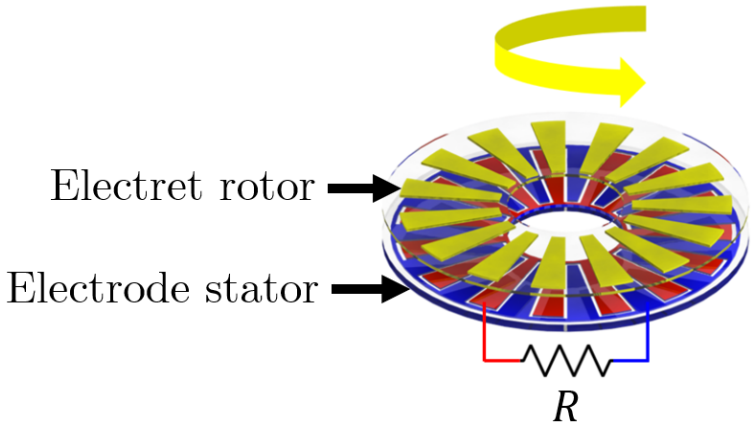

Figure 3.2: Schematic showing the resulting energy harvester concept. The electret segments are shown in yellow, and the interdigitated electrode is shown in blue and red.

A more detailed schematic of the rotational electret transducer, including the interdigitated electrode pair, is shown in Figure 3.2. The electret rotor rotates relative to the electrode pair. The electret segments are shown in yellow. The electrode pair is connected by a load resistance R.

4

NOVEL ELECTROSTATIC MODEL FOR ELECTRET TRANSDUCERS

In this chapter, the shortcomings of the conventional electret transducer models are discussed. A novel electrostatic model is proposed which takes fringing fields into account which allows for a more accurate prediction of the output power characteristics of micro-electret transducers. To verify the model, a comparison is made between the novel model predictions and the measured output power characteristics of a reported electret transducer. The output power characteristics of the electret transducer are found to closely follow the novel model predictions.

Novel electrostatic model for electret transducers

F. Schilperoort

***Abstract*— Energy harvesting by means of micro-electret transducers is a promising method to power small-scale devices. Micro-electret transducers can be fabricated using conventional microfabrication processes at a large scale, and exhibit a large electromechanical coupling with favorable output power characteristics such as a high output voltage.**

One-dimensional models have been developed to predict the output power of electret transducers. However, fringing fields play a large role in the electrostatic domain for micro-electret transducers. Therefore, the one-dimensional electret transducer model is inaccurate and can lead to a significant overestimation of the output power.

To be able to more accurately predict the output power characteristics of micro-electret transducers, a two-dimensional electrostatic model is proposed which accounts for fringing fields. This two-dimensional model allows for more accurate optimization of design parameters early in the design phase, leading to an improved transducer performance. To verify the model, a comparison is made between the novel model predictions and the measured output power characteristics of a reported electret transducer. The output power characteristics of the electret transducer are found to closely follow the novel model predictions.

Keywords: Energy harvesting, Electret, Electrostatic transduction, two-dimensional model, Fringing fields

I. INTRODUCTION

A. Mechanical energy harvesting

Mechanical energy harvesting is the method of transforming ambient mechanical energy into electrical energy by means of an appropriate transduction mechanism. For mechanical energy harvesters, a number of methods have been identified that can be used to cnvert mechanical energy into electrical energy, such as electrostatic transduction [1]–[4], piezoelectric transduction [5]–[7] and electromagnetic transduction [8]–[11].

For micro-energy harvesters, electromagnetic transduction, the most well-established transduction method, does not perform well [12, 13]. For electromagnetic transducers, the output voltage scales proportionally with the magnet velocity and the number of coil turns squared. Due to size limitations, the number of coil turns is limited. This means that the magnet velocity needs to be extremely large to achieve a sufficient output voltage.

Electrostatic transduction is a promising alternative transduction method for micro-energy harvesters. This is due to their compatibility with microfabrication methods, high electromechanical coupling, small size, and high output voltage [14, 15]. Electrets have been identified as a method of inducing charge, allowing for power generation without the need for an external power source and power management circuit as bias, which is the case for electret-free electrostatic transduction [16].

B. Freestanding electret transducers

Freestanding electret transducers are a type of electret transducer in which the electret is decoupled from the electrodes. In Figure 1, a section view of a rotational freestanding electret transducer is shown. The electret is attached to a mover and moves relative to pair of interdigitated electrodes, on which the electret induces charge. In such an electret transducer configuration, infinite mover displacement is possible, as the electrodes with the attached signal lines are attached to the stator [15].

The ability to achieve very large mover displacements enables an energy harvester using a freestanding electret transducer to harvest energy from low frequency and large amplitude signals effectively [15]. Because of this, freestanding electret transducers are promising electret transducer configurations for harvesting energy from human motion. As the frequency of human motion is very low ($< 12Hz$) [9, 17], and its amplitude is on the order of millimeters to meters.

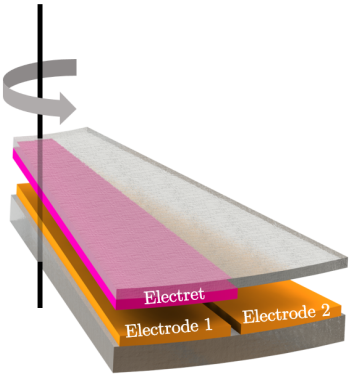

Fig. 1: Section view showing one 'unit cell' of a freestanding rotational electret transducer with the electret segment (pink) on the rotor and the two electrodes (orange).

For freestanding electret transducers, the output power scales inversely proportional with the electrode width.

$$P \propto \frac{1}{w} \tag{1}$$

Where P is the output power and w is the electrode width. To ensure that the electret transducer has high output power, electret transducers with increasingly narrow interdigitated electrodes have been fabricated [15, 18, 19]. These so-called

micro-electret transducers achieve a higher output power with an output voltage on the order of tens of Volts.

Bi et al. have proposed a one-dimensional (1D) electrostatic model that predicts the output power characteristics of electret transducers [20]. The model predicts the output power characteristics of larger electret transducers accurately, where fringing fields can be ignored, but for micro-electret transducers, the model greatly overestimates the performance.

For micro-electret transducers, the width of the electrode and the distance between the electret and the electrode are on the same order of magnitude. This is because the gap distance between the electret and the electrodes is limited by manufacturing tolerances and dielectric breakdown of air.

As a result, fringing fields can no longer be ignored and a more accurate two-dimensional (2D) model has to be used that takes fringing fields into account. In this work, an improved 2D model is proposed, and verified by comparing the model predictions with measurement results from a reported electret transducer.

II. WORKING PRINCIPLE AND MODEL

A. Theory

Electret transducers generate energy using an electret with embedded charge density σ to induce a charge σ_i on interdigitated electrodes. When the electret moves relative to the two electrodes, which are connected by a load resistance R, the induced charge moves from one to the other electrode. Part of the charge is stored in the capacitance C, which exists due to the proximity of the two electrodes, and part of the charge flows through the load resistance. A schematic representation of an electret transducer is shown in Figure 2 below. This simple schematic representation can be used to model the output power characteristics of electret transducers.

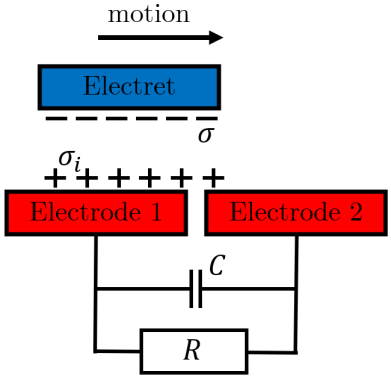

Fig. 2: Schematic of a freestanding electret transducer that is used as a basis for the transducer model.

1) Conventional one-dimensional model: The derivation of the conventional 1D model is explained to show the difference between the conventional 1D model and the novel 2D model.

By applying Kirchhoff's first law, we can balance the current in the circuit.

$$\sum i = 0 \tag{2}$$

This results in the following expression for the total current across the load resistance.

$$i(t) + \frac{dQ_E}{dt} + \frac{dQ_C}{dt} = 0$$

Where $i(t)$ is the current across the load resistance, $\frac{dQ_E}{dt}$ is the change of the electrode charge and $\frac{dQ_C}{dt}$ is the change in the capacitor charge.

The charge stored in the capacitance can be expressed as a function of the charge across the load resistance as follows.

$$Q_C = C \cdot u \Longrightarrow u = i \cdot R \Longrightarrow \frac{dQ_C}{dt} = RC\frac{di}{dt} \tag{4}$$

This results in the following expression for the current across the load resistance.

$$i(t) + \frac{dQ_E}{dt} + RC\frac{di}{dt} = 0 \tag{5}$$

When assuming that fringing fields are negligible, the induced charge is constant on the area below the electret and equal to σ_i, and 0 everywhere else. This can be used to calculate the total charge on the electrode which is equal to the area of the electret superimposed on the electrode, multiplied by the induced charge. The area of the electrode that has an induced charge is equal to the total electret area S_0, multiplied by a time-dependent factor.

$$S(t) = S_0(1 - \frac{n\theta}{\pi}) = S_0(1 - \frac{n\omega t}{\pi}) \tag{6}$$

Where S_0 is the total electret area, n is the number of electret segments, θ is the angle of the rotor, ω is the angular velocity of the rotor and t is the time. Now the total charge on the electrode can be calculated by multiplying the induced charge density σ_i with the area of the induced charge $S(t)$ as defined in Equation 6.

$$Q_E = \sigma_i S(t) = \sigma_i S_0(1 - \frac{n\omega t}{\pi}) \quad t \in \left[0, \frac{\pi}{n\omega}\right) \tag{7}$$

By taking the time derivative of the electrode charge Q_E, the charge that is flowing from the electrode can be found.

$$\frac{dQ_E}{dt} = -\sigma_i S_0 \frac{n\omega}{\pi} \quad t \in \left[0, \frac{\pi}{n\omega}\right) \tag{8}$$

This expression can be plugged into Equation 5, which results in the following differential equation.

$$i(t) - \sigma_i S_0 \frac{n\omega}{\pi} + RC\frac{di}{dt} = 0 \quad t \in \left[0, \frac{\pi}{n\omega}\right) \tag{9}$$

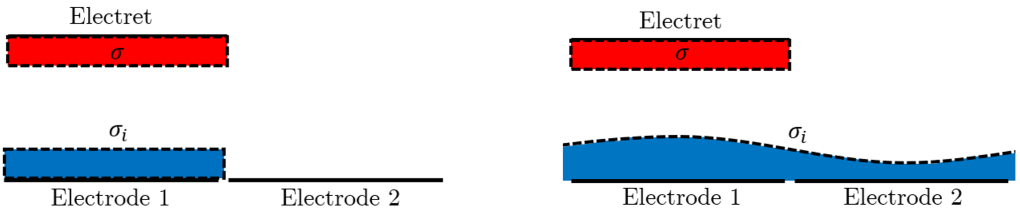

Fig. 3: (a) Schematic representation of the charge distribution on the electrodes for the conventional one-dimensional model. **(b)** Schematic representation of the charge distribution on the electrodes for the novel two-dimensional model.

Solving this differential equation with the initial boundary condition $i|_{t=0} + i|_{t=\frac{\pi}{n\omega}} = 0$ and the periodic boundary condition $i|_{t=0} = i|_{t=\frac{2\pi}{n\omega}}$, an expression for the current across the load resistance is found, which can be used to calculate the average power. The resulting equation for the average power is shown in Equation 43.

$$P_{av} = \frac{\sigma_i^2 S_0^2 n\omega}{\pi^2 C}\kappa \tag{10}$$

Where P_{av} is the average power generated and κ is an expression dependent on the dimensionless factor a.

$$\kappa = a + \frac{2a^2}{\pi}\left(1 - \frac{2}{1+\exp\left(-\frac{\pi}{a}\right)}\right) \tag{11}$$

a equals the product of the time constant (RC) of charge transfer and the working frequency $(n\omega)$ of the freestanding electret transducer.

$$a = n\omega RC \tag{12}$$

2) Novel two-dimensional model: The novel 2D model uses a new expression for the induced charge on the electrode. The difference in the induced charge on the electrode is shown qualitatively in Figure 3.

a) Method of image charges: First, Gauss' law is used to determine the electric field as a result of a point charge. To simplify the calculations, the calculation is performed for a charge in a 2D plane, as opposed to a three-dimensional space. This simplification results in only a minor deviation between the model predictions and the actual result as the length of electrode segments are orders of magnitude larger than the width for most electret transducers.

$$\oint \vec{E} \cdot d\vec{A} = \frac{q_{\text{enc}}}{\varepsilon_0} \tag{13}$$

Where $\vec{E}$ is the Electric field, $\vec{A}$ is the surface area, q_{enc} is the enclosed charge and ϵ_0 is the vacuum permittivity. For a point charge q in two dimensions, this reduces to the following expression.

$$E(r) \cdot 2\pi r_q = \frac{q}{\epsilon_0}\hat{r_q} \tag{14}$$

Where r_q is the distance from the point charge and $\hat{r_q}$ is the radial unit vector. Rearranging gives the following expression for the electric field induced by a point charge.

$$E(r_q) = \frac{q}{2\pi r_q \epsilon_0}\hat{r_q} \tag{15}$$

Now the method of image charges can be applied to determine the charge density on an electrode as a result of a nearby point charge. The method of image charges can be used to simply calculate the distribution of the electric field of a charge in the vicinity of a conducting surface. A visualization of the method of image charges can be seen in Figure 4.

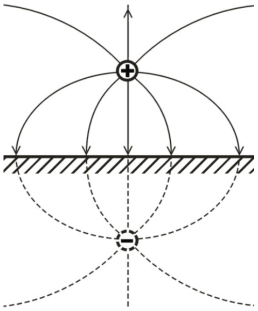

Fig. 4: The electric field of a charge near a flat conducting surface, found by the method of images.

The distance between the charge and the image charge is equal to twice the distance between the image charge and the electrode which is equal to z. The electrostatic field perpendicular to the electrode surface as a result of a charge q is given as follows.

$$E_z(r_q) = \frac{q}{2\pi r_q \epsilon_0}\hat{z} \tag{16}$$

Where $\hat{z}$ is the unit vector perpendicular to the electrode surface.

$$\hat{z} = \frac{z}{r_q}, r_q = \sqrt{x^2 + z^2} \tag{17}$$

By substituting r_q and $\hat{z}$ as functions of the dimensions z, and x, the equation can be simplified as follows.

$$E_z(x) = \frac{1}{2\pi\epsilon_0}\frac{q}{\sqrt{x^2+z^2}}\hat{z} = \frac{q}{2\pi\epsilon_0}\frac{z}{x^2+z^2} \tag{18}$$

When accounting for the charge and the image charge by the method of superposition, the following expression is found.

$$E_z(x) = \frac{1}{2\pi\epsilon_0}\frac{q\cdot z}{x^2+z^2} + \frac{1}{2\pi\epsilon_0}\frac{-q\cdot -z}{x^2+z^2} = \frac{q}{\pi\epsilon_0}\frac{z}{x^2+z^2} \tag{19}$$

From the electric field, the charge density as a function of x and z can be found.

$$\sigma(x) = \epsilon_0 \cdot E_z(x) = \frac{q}{\pi}\frac{z}{x^2+z^2} \tag{20}$$

The charge density on an electrode surface as a result of a point charge is schematically represented in Figure 5.

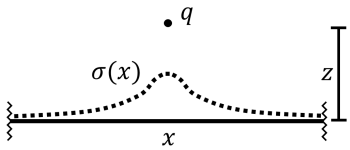

Fig. 5: Charge distribution on a conductive surface as a consequence of a point charge q.

The charge density induced on an electrode by a point charge can be used to make a numerical model for the charge distribution. Using the principle of superposition, the charge distribution $\sigma(x)$ on an electrode as a result of a charged line segment w at a distance z above the conductive surface can be approximated as a combination of n_q number of point charges spaced a distance dx away from each other.

$$dx = \frac{w}{n_q+1} \tag{21}$$

The charge magnitude q is equal to the area of one electret segment divided by the number of point charges n_q.

$$q = \frac{\sigma S_0}{n n_q} \tag{22}$$

The charge distribution is then calculated as follows.

$$\sigma(x) = \sum_{i=-n/2}^{n/2}\sigma_i(x) = \sum_{i=-n/2}^{n/2}\frac{q}{\pi}\frac{z}{(x-i\cdot dx)^2+z^2} \tag{23}$$

This charge distribution is calculated as a function of the ratio between the width of the electrode and the distance between the electret and the electrode $r = \frac{w}{z}$. This is plotted in Figure 6.

What can be seen in Figure 6, is that when the value of r decreases, the charge distribution looks less like a square wave, which is the assumption made by the 1D model, and more like a sine wave.

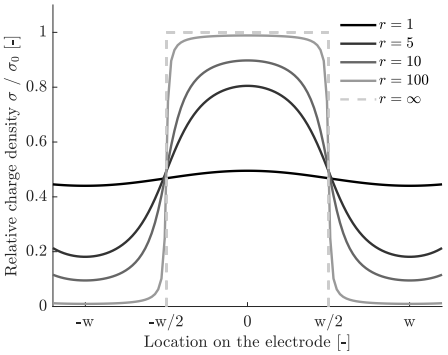

Fig. 6: Normalized charge distribution as a function of r.

b) Curve fitting: For micro-electret transducers, the value of r is generally lower than ten. This is because the width w of the electret segments is narrow as this leads to higher output power, whereas the distance between the electret and the electrode z is limited by manufacturing tolerances and dielectric breakdown of air. For these values of r, a sine fit can be made to approximate the charge distribution on the electrodes. The charge distribution according to a sine fit is equal to the following expression.

$$\sigma(x) = \sigma_{avg} + Acos(\frac{\pi x}{w}) \tag{24}$$

Where σ_{avg} is the average charge density, and A is the amplitude of the charge density. The amplitude of the charge density is calculated by taking the maximum and minimum value of $\sigma(x)$ as calculated according to Equation 23 for a range of values of r.

$$A = \frac{max(\sigma(x)) - min(\sigma(x))}{2} \tag{25}$$

In Figure 7, the dimensionless charge amplitude $\frac{A}{\sigma_0}$ is plotted for values of r ranging from 1 to 100. A rational fit can be made to find an analytical expression for the charge amplitude as a function of r.

$$\frac{A}{\sigma_0} = \frac{r-1}{2r+\frac{7}{2}} \tag{26}$$

Where σ_0 is the maximum possible induced charge, that would be achieved if fringing fields would not influence the charge distribution.

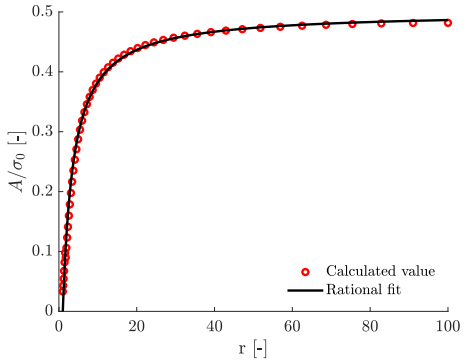

Fig. 7: Normalized charge amplitude as a function of the ratio r as calculated using the method of image charges (red circles) and the rational fit (black).

To verify whether the charge distribution on the electrodes is well-approximated by the sine fit, the normalized charge difference ΔQ_{norm} is compared between the calculated value, the conventional model, and the novel model. The normalized charge difference is the difference in charge between electrode 1 (Q_1) and electrode 2 (Q_2), divided by the total charge induced (Q_0).

$$\Delta Q_{norm} = \frac{Q_1 - Q_2}{Q_{tot}} \tag{27}$$

Electrode 1 and electrode 2 are schematically represented in Figure 3. The calculated value of Q_1 and Q_2 are found by numerically integrating the charge distribution as calculated in Equation 23.

$$Q_1 = \sum_{i=-w/2}^{w/2} \sigma(x)dx \quad Q_2 = \sum_{i=w/2}^{3w/2} \sigma(x)dx \tag{28}$$

The conventional model makes the following assumption for Q_1 and Q_2.

$$Q_1 = \sigma_i(x)w \quad Q_2 = 0 \tag{29}$$

The novel model value of Q_1 and Q_2 can be found by integrating $\sigma(x)$ as calculated according to Equation 24.

$$Q_1 = \int_{-w/2}^{w/2} \sigma(x)dx \quad Q_2 = \int_{w/2}^{3w/2} \sigma(x)dx \tag{30}$$

This results in the following expressions for Q_1 and Q_2.

$$Q_1 = \sigma_{avg}w + \frac{2\pi}{w}A \quad Q_2 = \sigma_{avg}w - \frac{2\pi}{w}A \tag{31}$$

In Figure 8, the normalized charge difference is shown for the novel model, the calculated value, and the conventional model. What can be seen is that for a value of $r \in [0, 10]$, the novel model predicts the charge distribution on the electrodes significantly more accurately than the conventional model. At larger values of r, the charge distribution looks more like a square wave. As a result, the sine fit will underestimate the total charge difference. The normalized charge difference prediction of the novel model asymptotically approaches the average value of a sine wave of an amplitude of one, which is approximately equal to 0.637.

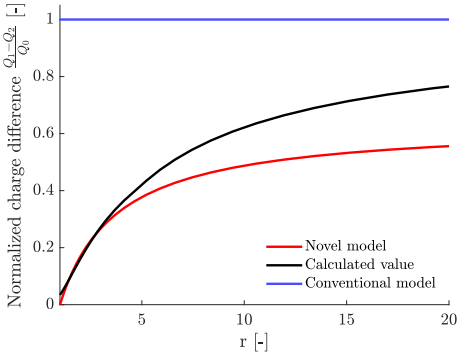

Fig. 8: The normalized charge difference between the two electrodes is calculated using the novel sine fit (red) compared to the actual value (black) and the old one-dimensional model (blue).

c) Rotational electret transducer: For a rotational electret transducer, the width of an electrode segment is not constant, but can instead be approximated by viewing the electrode as an isosceles trapezium, as can be seen in Figure 9. This assumption neglects the effects of the circular segments at the inner and outer radius, but these effects are small when the angle of the electrode segment is small, which is the case for micro-electret transducers as the number of electret segments is large in order to maximize the output power.

In such a case, the width increases linearly with the radius from w_i at the inner radius r_i, to w_o at the outer radius r_o. The average charge amplitude is calculated by integrating the expression for the charge amplitude over the electrode length as follows.

$$\frac{\tilde{A}}{\sigma_0} = \frac{1}{\frac{w_o}{z} - \frac{w_i}{z}} \int_{\frac{w_i}{z}}^{\frac{w_o}{z}} \frac{A}{\sigma_0} = \frac{1}{2} - \frac{1}{\frac{w_o}{z} - \frac{w_i}{z}} \frac{11}{8} \log\left(\frac{\frac{w_o}{z} + \frac{7}{4}}{\frac{w_i}{z} + \frac{7}{4}}\right) \tag{32}$$

Where $\tilde{A}$ is the average charge amplitude along the radius of a rotational electrode segment.

d) Dynamic model: When the relative movement between the electret and the electrodes is taken into account, the following traveling wave represents the charge on a location on the electrode at a certain location x and time t on the electrode.

$$\sigma(x,t) = \sigma_{avg} + Acos(\frac{\pi x}{w} - n\omega t) \tag{33}$$

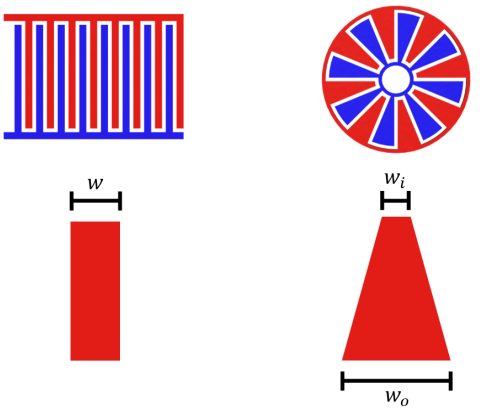

a. b.

Fig. 9: The difference in the electrode shape of a translational (a) and a rotational (b) interdigitated electrode configuration.

The total charge on one electrode segment can be calculated by integrating the charge distribution over the width of the electrode, and assuming that fringing fields in the lengthwise direction of the electrode are small due to the relatively large length L of the electrode relative to the width w.

$$Q_E = \iint_S \sigma(x,t)dS = S_0(\sigma_{avg} + \frac{2A}{\pi}cos(n\omega t)) \quad (34)$$

To calculate the current flowing across the electrode, the electrode charge can be differentiated with respect to time.

$$\frac{dQ_E}{dt} = -\frac{2AS_0n\omega}{\pi}sin(n\omega t) \quad (35)$$

The current flowing across the electrode is then plugged into Equation 5 which results in the following differential equation for the current across the load resistance.

$$i(t) = -\frac{dQ_E}{dt} - RC\frac{di}{dt} = \frac{2AS_0n\omega}{\pi}sin(n\omega t) - RC\frac{di}{dt} \quad (36)$$

Solving this differential equation using the initial boundary condition $i|_{t=0} + i|_{t=\frac{\pi}{n\omega}} = 0$ leads to the following result for the current through the load resistance.

$$i(t) = \frac{2AS_0n\omega}{\pi R^2C^2n^2\omega^2 + \pi}(n\omega RCcos(n\omega t) - sin(n\omega t)) \quad (37)$$

The voltage $u(t)$ can be found by multiplying the current by the load resistance.

$$u(t) = i(t)R = \frac{2AS_0n\omega R}{\pi R^2C^2n^2\omega^2 + \pi}(n\omega RCcos(n\omega t) - sin(n\omega t)) \quad (38)$$

The open circuit voltage u_{os} can be found by setting R to ∞, resulting in the following expression.

$$u_{os}(t) = -\frac{2AS_0}{\pi C}cos(n\omega t) \quad (39)$$

The short circuit current i_{ss} can be found by setting R to 0, resulting in the following expression.

$$i_{ss}(t) = \frac{2AS_0n\omega}{\pi}sin(n\omega t) \quad (40)$$

The output power P can be calculated by multiplying the current squared with the load resistance.

$$P = i(t)^2R \quad (41)$$

The average output power P_{avg} can be calculated by integrating the power over one period and then dividing it by said period.

$$P_{avg} = \frac{1}{T}\int_0^T i(t)^2R \quad , \quad T = \frac{2\pi}{n\omega} \quad (42)$$

This results in the following expression for the average output power.

$$P_{avg} = \frac{2A^2RS_0^2n^2\omega^2}{\pi^2\left(C^2R^2n^2\omega^2 + 1\right)} \quad (43)$$

The matched load R_m that leads to the highest output power can be easily found by taking the derivative of the power with respect to the load resistance and equating this to zero.

$$\frac{dP_{avg}}{dR} = 0 \quad (44)$$

The matched load is then found to be equal to the following expression.

$$R_m = \frac{1}{Cn\omega} \quad (45)$$

Plugging this result into Equation 43 results in the following expression for the average output power at matched load $P_{m.avg}$.

$$P_{m.avg} = \frac{A^2S_0^2n\omega}{\pi^2C} \quad (46)$$

III. RESULTS AND DISCUSSION

To verify the novel model, a comparison can be made between the novel model, the conventional model, and the experimental results of published electret transducers. In Table I, the parameters of an electret transducer fabricated by Bi et al. are shown.

TABLE I: Parameters of the electret transducer of Bi et al. [20].

Parameter	Value	Description
z	300 $[\mu m]$	Gap between the rotor and stator
g	500 $[\mu m]$	Gap between electrodes
n	16 [-]	Number of electret segments
r_i	7.5 $[mm]$	Inner radius electret rotor
r_o	50 $[mm]$	Outer radius electret rotor
σ	0.045 $[mC/m^2]$	Surface charge density
C	70 $[pF]$	Capacitance

Using the parameters of the electret transducer, the charge amplitude and the total electret area can be calculated. The electret area is equal to half the rotor area.

$$S_0 = \frac{\pi(r_o^2 - r_i^2)}{2} = 3800mm^2 \tag{47}$$

By filling in Equation 32 with the parameters stated in Table I, the following charge amplitude is found.

$$\frac{\tilde{A}}{\sigma_0} \approx 0.407 \Longrightarrow A \approx 18.3\mu C/m^2 \tag{48}$$

If the values of S_0 and A, together with the capacitance C and the number of electret segments n noted in Table I are plugged into Equation 43, the output power as a function of the load resistance can be calculated and compared to the conventional model and the experimental results published by Bi et al.

In Figure 10, the conventional model prediction versus the experimental measurements can be seen for two fixed rotational velocities of 750 rpm and 375 An average overestimation of the output power of 54% is found.

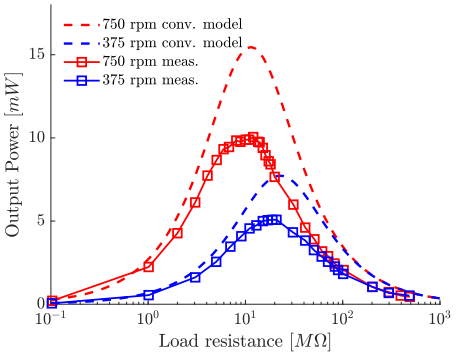

Fig. 10: RMS Power as a function of load resistance at a fixed angular velocity of 750 (red) and 375 (blue) rad/s according to the conventional model predictions (dashed line) and measurements (markers).

In Figure 11, the novel model prediction versus the experimental measurements can be seen for two fixed rotational velocities of 750 rpm and 375 rpm. The novel model predictions are very accurate, with an average underestimation of the output power of just 11%. The model underestimates the output power since the charge distribution is assumed to be a sine fit. Whereas, for this transducer with a relatively large ratio of r, the charge distribution is somewhere in between a square wave and a sine wave.

IV. CONCLUSION

A novel two-dimensional model is proposed which can be used to accurately predict the output power characteristics of micro-electret transducers. The novel model is conceived as the conventional one-dimensional models for electret

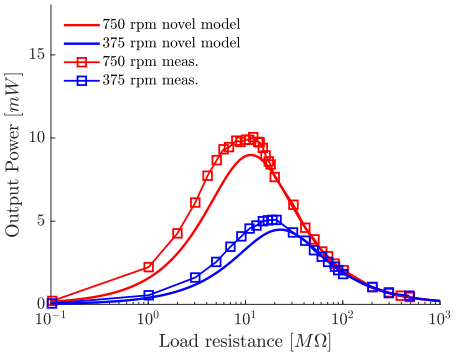

Fig. 11: RMS Power as a function of the load resistance at a fixed angular velocity of 750 (red) and 375 (blue) rad/s according to the novel model predictions (solid line) and measurements (markers).

transducers assume that fringing fields can be neglected when calculating the magnitude of the charge which is induced by an electret. For micro-electret transducers, this assumption does not hold, as the distance between the electret and the electrodes is on the same order of magnitude as the width of the electret segments.

The novel model includes the effects of fringing electric fields by applying the method of image charges in a numerical model. An analytical fit for the charge amplitude as a function of the transducer parameters is made which is used to calculate the output power characteristics of the micro-electret transducer. The model is straightforward to apply and allows for taking fringing fields into account in the early design phase. This means that no iterative design processes using finite element analyses are necessary, which has been the standard method of accounting for fringing fields. The novel model significantly simplifies the process of designing micro-electret transducers.

To verify the novel two-dimensional model, a comparison is made between the novel two-dimensional model predictions, the conventional one-dimensional model predictions, and the output power characteristics of an electret transducer reported by Bi et. al. It is found that the model accurately predicts the output power characteristics of the reported electret transducer, with an average deviation of 11 % in RMS output power for the novel two-dimensional model, compared to a 54 % deviation for the conventional one-dimensional model.

REFERENCES

[1] M. Kiziroglou, C. He, and E. Yeatman, "Non-resonant electrostatic energy harvesting from a rolling mass," pp. 318 – 321, 07 2008.

[2] H. C.-H. K. H.-D. . Y. J.-B. Choi, Dong-Hoon, "Liquid-based electrostatic energy harvester with high sensitivity to human physical motion.," *Smart Materials and Structures*, vol. 20, 2011.

[3] P. Basset, D. Galayko, F. Cottone, R. Guillemet, E. Blokhina, F. Marty, and T. Bourouina, "Electrostatic vibration energy harvester with combined effect of electrical nonlinearities and mechanical impact," *Journal of Micromechanics and Microengineering*, vol. 24, 02 2014.

[4] L. Bu, X. Wu, X. Wang, and L. Liu, "Non-resonant electrostatic energy harvester for wideband applications," *Micro & Nano Letters*, vol. 8, no. 3, pp. 135–137, 2013.

[5] H. Fu and E. M. Yeatman, "A methodology for low-speed broadband rotational energy harvesting using piezoelectric transduction and frequency up-conversion," *Energy*, vol. 125, no. C, pp. 152–161, 2017.

[6] K. Fan, Z. Liu, H. Liu, L. Wang, Y. Zhu, and B. Yu, "Scavenging energy from human walking through a shoe-mounted piezoelectric harvester," *Applied Physics Letters*, vol. 110, p. 143902, 04 2017.

[7] L. Gu, "Low-frequency piezoelectric energy harvesting prototype suitable for the mems implementation," *Microelectron. J.*, vol. 42, pp. 277–282, 2011.

[8] H. Liu, S. Gudla, F. A. Hassani, C.-H. Heng, Y. Lian, and C. Lee, "Investigation of the nonlinear electromagnetic energy harvesters from hand shaking," *IEEE Sensors Journal*, vol. 15, pp. 2356–2364, 2015.

[9] H. Liu, C. Hou, J. Lin, Y. Li, Q. Shi, L. Sun, and C. Lee, "A non-resonant rotational electromagnetic energy harvester for low-frequency and irregular human motion," *Applied Physics Letters*, vol. 113, p. 203901, 11 2018.

[10] M. A. Halim, H. Cho, M. Salauddin, and J. Y. Park, "A miniaturized electromagnetic vibration energy harvester using flux-guided magnet stacks for human-body-induced motion," *Sensors and Actuators A: Physical*, vol. 249, pp. 23–31, 2016.

[11] M. Geisler, S. Boisseau, P. Gasnier, J. Willemin, C. Gobbo, G. Despesse, I. Ait-Ali, and S. Perraud, "Looped energy harvester for human motion," *Smart Materials and Structures*, vol. 26, 08 2017.

[12] S. Beeby and N. White, "Energy harvesting for autonomous systems," vol. 308, 01 2010.

[13] S. Roundy, "Energy scavenging for wireless sensor nodes with a focus on vibration to electricity conversion," 01 2003.

[14] S. Boisseau, G. Despesse, T. Ricart, E. Defay, and A. Sylvestre, "Cantilever-based electret energy harvesters," *Smart Materials and Structures*, vol. 20, no. 10, p. 105013, 2011.

[15] Y. Suzuki, "Recent progress in mems electret generator for energy harvesting," *IEEJ Transactions on Electrical and Electronic Engineering*, vol. 6, no. 2, pp. 101–111, 2011.

[16] S. Boisseau, G. Despesse, and B. Seddik, "Electrostatic conversion for vibration energy harvesting," *Intech*, 10 2012.

[17] D. Qiao, G. Pang, M. Kit, and D. Lam, "A new pcb-based low-cost accelerometer for human motion sensing," pp. 56 – 60, 10 2008.

[18] D. Miki, M. Honzumi, Y. Suzuki, and N. Kasagi, "Mems electret generator with electrostatic levitation," 2009.

[19] T. Miyoshi, M. Adachi, K. Suzuki, Y. Liu, and Y. Suzuki, "Low-profile rotational electret generator using print circuit board for energy harvesting from arm swing," *2018 IEEE Micro Electro Mechanical Systems (MEMS)*, pp. 230–232, 2018.

[20] M. Bi, S. Wang, X. Wang, and X. Ye, "Freestanding-electret rotary generator at an average conversion efficiency of 56studies," *Nano Energy*, vol. 41, pp. 434–442, 2017.

[21] R. Igreja and C. Dias, "Analytical evaluation of the interdigital electrodes capacitance for a multi-layered structure," *Sensors and Actuators A: Physical*, vol. 112, no. 2, pp. 291–301, 2004.

5

IMPROVED ELECTRET TRANSDUCER PERFORMANCE THROUGH NOVEL UNIPOLAR ELECTRET

In this chapter, the performance of electret transducers is improved through a novel 'unipolar' electret design. Conventional electret transducers only induce a fraction of their embedded charge on the counter electrodes. In conventional electrets, the electret is deposited and charged on a conductive substrate. As a result, most of the charge is induced on this conductive substrate. This charge is 'idle' and does not aid in energy transduction. It is important to maximize the induced charge on the counter electrodes, as the power output of an electret transducer scales quadratically with the induced charge. In the novel unipolar electret design, the conductive substrate is replaced with a thin dielectric substrate. As a result, charges of only one polarity are embedded, maximizing the charge the electret can induce and thus increasing the power output of the electret transducer. The novel unipolar micro-electret transducer is found to achieve a power output that is twice as high, and better charge stability compared to conventional electret transducers.

Improved electret transducer performance through novel unipolar electret

F. Schilperoort

***Abstract*— Electret transducers are a class of transducers that utilize the electric field generated by an electret to induce a charge on an electrode. When the electret is moved relative to the electrode, the induced charge magnitude changes and this generates a current that can be used to convert mechanical energy into electrical energy.**

Conventional electrets consist of a thin electret layer on top of a conductive substrate. As a result of this, most of the charge induced by the electret is induced on this conductive substrate. This means that the charge induced on a counter electrode is only a fraction of the embedded charge of the electret.

For electret transducers, the induced charge on the substrate is 'idle' and is not used in energy transduction. In this work, a novel electret design is proposed, consisting of a patterned electret on ultra-thin glass. The novel electret design does not have a conductive substrate as the electret layers are deposited on a dielectric. Because of this, the electret only contains charges of one polarity, and is thus 'unipolar', as opposed to conventional bipolar electrets. This unipolar electret design achieves a higher induced charge on the electrodes, as the electric field will be fully directed toward the counter electrodes. Because the power of an electret transducer scales quadratically with the magnitude of the induced charge, the new design leads to a significantly improved output power. The new unipolar electret design also has other benefits, such as higher charge stability, and a decreased need for accurate gap control. Keywords: Energy harvesting, Electret, Electrostatic transduction, Unipolar electret, Freestanding electret

I. INTRODUCTION

To facilitate the development of the internet of things (IoT), and industry 4.0, more data from our surroundings needs to be collected. This results in the production of more and more wireless sensors and small-scale devices. The conventional method of powering these devices is through connection to a central power supply or by battery connectivity. Both of these methods have considerable downsides, namely a reduction in flexibility and an increase in cost, size, and maintenance [1, 2].

Mechanical energy harvesting can be a solution for the power supply of small-scale devices. In mechanical energy harvesting, ambient energy from the surroundings is converted to electrical energy and supplied to a device. This allows for the device to work decoupled from a central power grid indefinitely.

For micro-energy harvesters, electromagnetic transduction, the most well-established transduction method, does not perform well [3, 4]. For electromagnetic transducers, the voltage scales proportionally with the magnet velocity and the number of coil turns squared. Due to size limitations, the number of coil turns is limited. This means that the magnet velocity needs to be extremely large to achieve a sufficient output potential.

While piezo-based energy harvesters have enjoyed much attention [5, 6], the electret has also attracted interest as a method of transduction [7, 8]. Electrets are materials that have a quasi-permanent embedded charge. In other fields, electrets have been widely used for decades, such as in microphones [9].

In the last decade, electret-based energy harvesting has garnered attention. This is due to its attractive properties, such as high lifetime, ability to be manufactured with traditional micro-machining technologies, high output voltage, and a high electro-mechanical coupling [10]–[13]. However, the reported electret energy harvesters are lacking in their output power due to the low amount of charge that is induced on the electrodes using the conventional electret transducer designs.

To maximize the output power of an electret transducer, the induced charge on the electrode has to be maximized, as the output power scales quadratically with the induced charge magnitude [14]. In most research describing electret transducers, the focus is on increasing the surface charge density of the electret. However, in the context of electret transducers, this focus on surface charge density is misleading. For electret transducers, the charge induced on the counter electrode, not the surface charge of the electret, is to be maximized. For conventional electrets that use a conductive substrate, most of the charge is induced on the substrate, instead of on the counter electrodes. This induced charge is 'idle' and does not aid power generation.

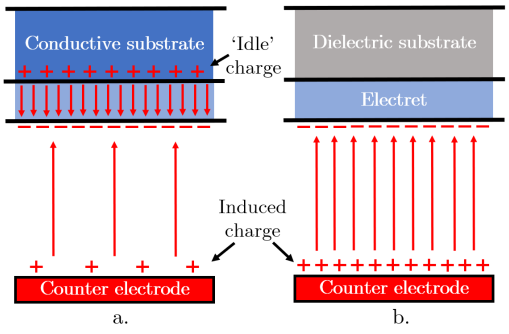

Fig. 1: (a) Conventional electret design. **(b)** The novel unipolar electret design. The red arrows represent the electric field lines and the minus and plus signs represent the negative and positive charges respectively.

In this work, an improved electret transducer design is

proposed that fully utilizes the embedded charge in the electret. This is done by depositing the electret on a thin dielectric substrate, instead of on a conductive substrate, as is the case in conventional electret transducers. The result of this can be seen schematically in Figure 1. The novel unipolar electret design has no 'idle charge' and thus induces a larger amount of charge on the counter electrodes. To verify the concept, an experimental transducer is fabricated using the novel unipolar electret design.

II. THEORY

A. Theoretical background

The charge induced by a conventional electret on a conductive substrate is graphically represented in Figure 2.

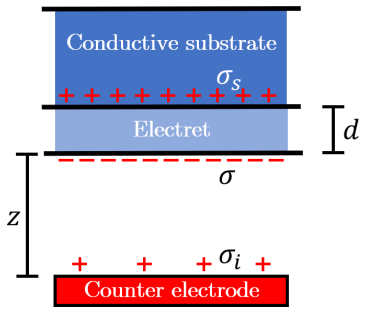

Fig. 2: Schematic showing the main dimensions and variables of the conventional electret transducer design.

Where z is the distance between the electret surface and the counter electrode, d is the electret thickness, σ is the electret charge density, σ_i is the counter electrode charge density, and σ_s is the substrate charge density.

An analytical expression for the induced charge can be made by assuming that the electric field outside of this system is zero, $\hat{\mathbf{E}} = 0$. This means that the substrate and the counter electrode are at ground potential. If this hypothesis is not met, analytical modelling is not possible as the induced charges will be ill-defined. To ensure that the substrate and the counter electrode are at ground potential, they can be grounded together, ensuring that the analytical expression is accurate.

When looking at a 1-dimensional situation, the contribution of each charge density to the field in air is equal to the following expression.

$$E_{\sigma_x} = \frac{\sigma_x}{2\epsilon_0} \tag{1}$$

Where E_{σ_x} is the electric field caused by charge density σ_x, and ϵ_0 is the vacuum permittivity. Using this equation, an expression for the net field outside the system E_o can be made.

$$E_o = \frac{\sigma + \sigma_s + \sigma_i}{2\epsilon_0} \tag{2}$$

As the electric field is zero outside the system, the sum of all charge densities is equal to zero.

$$\sigma + \sigma_s + \sigma_i = 0 \tag{3}$$

Equation 1 can now be used to calculate the electric field inside the electret, E_d, and the electric field inside the air E_a

$$E_d = \frac{\sigma_s - \sigma - \sigma_i}{2\epsilon_0\epsilon_d} \quad , \quad E_a = \frac{\sigma_i - \sigma - \sigma_s}{2\epsilon_0} \tag{4}$$

Where ϵ_d is the relative permittivity of the electret. Because the substrate and the counter electrode are grounded, their potentials are equal. An expression can be made for the induced charge by equating the potential drop in air and the potential drop inside the electret.

$$V_a = V_d \Longrightarrow E_a \cdot z = E_d \cdot d \Longrightarrow \sigma_i = -\frac{\sigma d}{d + \epsilon_d z} \tag{5}$$

Where V_a is the voltage drop inside the air, and V_d is the voltage drop inside the electret.

By filling in Equation 5 using data from reported electret transducers, the induced charge density as a factor of the electret charge density can be calculated. For the analyzed electret transducers, the induced charge is a factor 14-21 times smaller than the surface charge of the electret [15]–[17].

B. Corona charging

The most common method to manufacture electrets is through corona charging. This is due to the simple set-up, low cost, and reliable results. In Figure 3, a schematic of a corona charging set-up can be seen.

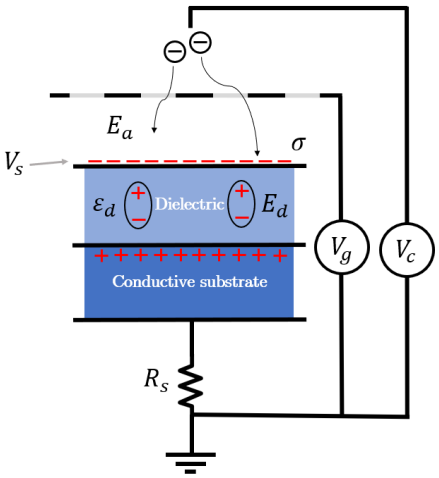

Fig. 3: Schematic of corona charging showing the main variables.

A needle at a high voltage V_c is used to generate corona discharge. This ionizes the air. The ions of the same polarity

as the needle are then accelerated through a grid at a potential V_g towards the electret surface on top of a grounded plate due to the electric field. These ions are then embedded into the surface of the electret, increasing the surface voltage V_s. When the surface voltage V_s approaches the grid voltage V_g, the electric field E_a between the grid and the electret surface decreases, and the ions stop being accelerated towards the electret surface. The final surface charge of the electret can be easily found using the following equation.

$$\sigma = \frac{\epsilon_0 \epsilon_d V_s}{d} \tag{6}$$

C. Limits to induced charge

There are two limits to the induced charge, namely **dielectric breakdown** and **external breakdown in air**. **Dielectric breakdown** occurs when the surface charge of the electret induces a sufficiently strong electric field E_d, causing the electret to conduct and allowing the charge to escape. In Table I, the relative permittivity and dielectric breakdown strength are shown for several common electret materials.

TABLE I: Parameters of common electret materials [18].

Material	Relative permittivity	Dielectric strength $(V/\mu m)$
PTFE	2.1	11.22
SiO_x/SiN_x	3.9/7.5	500
CYTOP	2.1	110
Parylene-HT	2.17	204.58

External breakdown in air happens when the surface voltage of the electrode exceeds Paschen's limit. Paschen's law states that discharge between two electrodes happens when the surface voltage of the electrode exceeds a certain voltage. The maximum voltage as a function of the gap size in air at atmospheric pressure is shown in Figure 4.

The induced charge in most conventional electret transducers is limited by dielectric breakdown. There are numerous downsides to this.

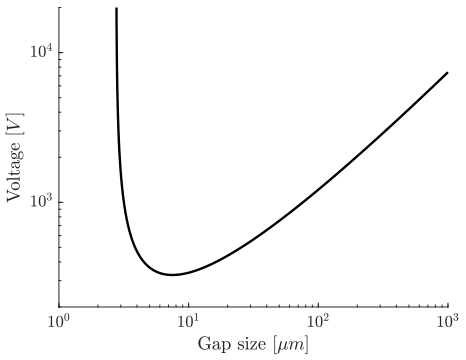

Fig. 4: Paschen's law in air at atmospheric pressure as a function of gap size.

- When the induced charge is limited by dielectric breakdown of the electret, the output power will be lower than when Paschen's limit for breakdown in air is reached, which is the upper limit for the induced charge.
- It is well-reported that charging to the dielectric breakdown limit results in a sharp initial decay of charge and the stable surface charge density achieved by charging up to the dielectric limit is significantly lower than the initial surface charge density [14, 19].
- To achieve a high induced charge with the conventional design, an extremely high electret surface charge is needed, on the order of 14-21 times higher than the induced charge as stated in a section I. It has been shown by Olthuis et al. that a higher electret charge density, and thus higher potential gradients lead to an increased charge decay, and thus a decreased lifetime of the device [20].

Even if a high enough stable surface charge of the electret can be achieved such that the induced charge on the counter electrode is limited by the external breakdown in air as stated by Paschen's law, the conventional design still has a major downside. Namely that the electric field strength inside the air is a function of the gap size, as can be seen when looking at the expression for the electric field in air in Equation 7.

$$E_a = -\frac{\sigma d}{\epsilon_0(d + \epsilon_d z)} \approx -\frac{\sigma d}{\epsilon_0 \epsilon_d z} \Longrightarrow E_a \propto \frac{1}{z} \tag{7}$$

The magnitude of the electric field scales inversely proportionally with the gap size. As a result of this, small changes in gap size could lead to a higher electric field strength in air, which causes a discharge of the electret. In Table II, the power decrease due to electret discharging as a function of parasitic motion in the z-direction is shown. What can be seen is that a larger parasitic motion leads to a significant decrease in output power. For a robust design where breakdown cannot occur regardless of parasitic motion, a decrease in output power of 90% is expected.

TABLE II: Output power decrease for conventional electret transducer as a function of parasitic motion of the electret in the out-of-plane direction for a design gap size of $100\mu m$.

Deflection $[\mu m]$	Performance decrease [%]
0	0
10	9.1
20	19
50	52
No chance of breakdown	90

D. The unipolar electret concept

The conventional electret design is thus limited in performance and is not robust when having to account for tolerances, manufacturing defects, and parasitic motion in the out-of-plane direction.

To improve the performance of conventional electret transducers, Boland et al. suggested increasing the thickness of the electret for an increased performance [21]. Increasing the thickness is not a viable solution, as it leads to

larger stresses, risk of cracking, bad charge stability when charging up to the breakdown limit [14, 19], more expensive fabrication, and does not solve the issues with discharge in air due to tolerances, manufacturing defects, and parasitic motion.

An alternative method to increase the maximum surface charge is by removing the conductive substrate from the electret. By removing the conductive substrate, σ_s will be equal to 0 and all the charge will be induced on the counter electrode. this leads to a higher induced charge, which is independent of the gap size. In such a situation, $\sigma_i = -\sigma$. This type of electret design is called 'unipolar', as the electret only contains charges of one polarity. Because of this, the electric field inside the air will be constant, irrespective of gap size, as is shown in Equation 8.

$$E_a = \frac{\sigma}{2\epsilon_0} - \frac{\sigma_i}{2\epsilon_0} = \frac{\sigma}{\epsilon_0} \tag{8}$$

This means that dielectric breakdown in air will not occur due to parasitic motion of the electret in the out-of-plane direction, and the decrease in output power due to parasitic motion is greatly diminished. This allows for electret transducer designs with larger tolerances, a necessity for electret transducers with large mover displacements such as rotational electret transducers.

Another important benefit is that with the novel unipolar electret concept, there is no direct path for the electret charges to recombine with charges of opposite polarity. For conventional electrets, charges can more easily recombine with free charges of opposite polarity in the conductive substrate, leading to charge decay. This effect is minimized in the novel unipolar electret as there is no conductive material in contact with the electret.

Several attempts have been made to fabricate a unipolar electret by peeling off the electret layer [14, 22] from its conductive substrate. However, this is not a method compatible with microfabrication processes, is costly and time-consuming, and is thus not suitable for large-scale fabrication. Furthermore, in the charging process, opposite charges are embedded in the back of the electret that is in contact with the conductive substrate. This reduces the induced charge on the counter electrodes considerably [14].

E. Proposed concept

A new method is proposed by depositing the electret on a dielectric substrate. This method uses MEMS-compatible fabrication, and in this method, no charge will be embedded into the backside of the electret. This is because the backside of the electret is not in contact with the conductive backplate. In Figure 5, a schematic of the novel electret design can be seen.

Where d_s is the substrate thickness. By replacing the conductive backplate with a dielectric substrate, the electric field generated by the electret is fully directed towards the counter electrode.

During corona charging, the surface charge can be calculated according to the same method as in Equation 6,

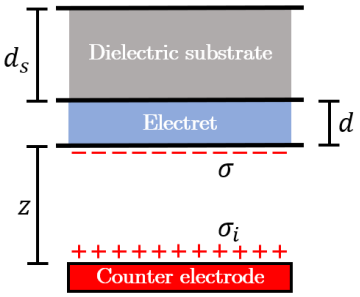

Fig. 5: Schematic showing the main dimensions of the unipolar electret transducer design.

but now the effect of the dielectric substrate on the capacitance has to be taken into account. When this is done, the following expression for the surface charge is found.

$$\sigma_i = -\sigma = -\frac{V_s \epsilon_0 \epsilon_d \epsilon_s}{d\epsilon_s + d_s \epsilon_0} \tag{9}$$

Where ϵ_s is the substrate dielectric constant. What can be seen from Equation 9 is that when assuming that the electret layer is significantly thinner than the dielectric substrate, the induced charge scales according to the following equation.

$$\sigma_i \propto \frac{V_s}{d_s} \tag{10}$$

This shows that when the substrate thickness increases, a larger surface voltage is needed to achieve the same induced charge. Furthermore, Zhang et al. have shown that implanting charge on a thick dielectric layer can be difficult, potentially due to the decreased electric field strength in the electret layer E_d during charging [23].

To ensure that charge implantation is not impaired and that the grid voltage V_g does not exceed the corona discharge voltage V_c, a thin dielectric substrate should be used.

F. Implementation of the concept

A freestanding rotational micro-electret transducer is designed according to the unipolar electret concept. An exploded view of the main components of the electret transducer can be seen in Figure 6.

For the electret material, an organic electret is chosen, as organic electrets have reliable electret properties. With inorganic electrets, the electret properties depend greatly on the deposition parameters. CYTOP (CTL-809M), hereafter abbreviated to CYTOP, is chosen as it has superior charge stability [24].

The rotor consists of a glass substrate with CYTOP segments oriented radially. The rotor is charged using a corona charging set-up. During charging, charge will be deposited on the glass substrate as well as on the CYTOP segments, but because the glass substrate does not contain any trap sites, charge will not be trapped and will stay 'floating' on the surface during charging, and dissipate

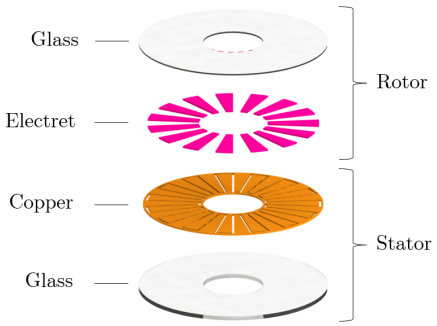

Fig. 6: Exploded schematic view of the freestanding electret transducer showing the main components comprising the rotor and the stator.

quickly thereafter. This leaves only the embedded charge on the CYTOP segments. During operation, the rotor rotates relative to the stator, consisting of a pair of interdigitated copper electrodes on glass as seen in the section view in Figure 7. By doing so, the induced charge on the counter electrodes will alternate between electrode 1 and electrode 2 as it rotates. This generates a current that can be used to harvest energy.

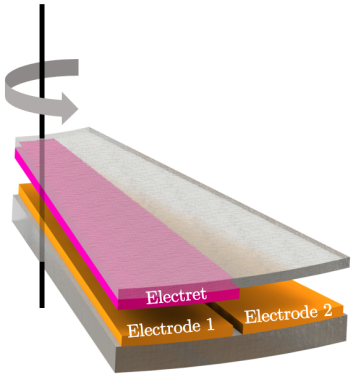

Fig. 7: Section view showing one 'unit cell' of a freestanding rotational electret transducer with the electret segment (pink) on the rotor and the two electrodes (orange).

The most important parameters that are used in the design of the electret-based transducer are shown in Table III.

TABLE III: Parameters of the micro-electret transducer.

Parameter	Value	Description
z	100 [μm]	Gap between the rotor and stator
d	4 [μm]	Electret thickness
n	57 [-]	Number of electret segments
r_i	4 [mm]	Inner radius electret rotor
r_o	10 [mm]	Outer radius electret rotor
ϵ_d	2 [-]	Relative permittivity of the electret
d_s	100 [μm]	Glass substrate thickness
ϵ_s	4.6 [-]	Glass substrate relative permittivity

III. FABRICATION

Figure 8 shows the simplified microfabrication process of the electret rotor and the electrode stator.

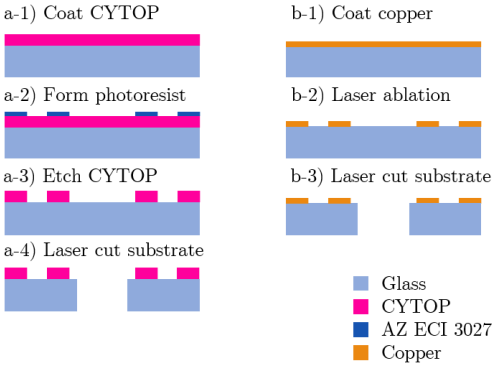

Fig. 8: Simplified microfabrication process flow of the electret rotor **(a)** and the electrode stator **(b)** for the micro-electret transducer.

A. Electret rotor

1) Electret deposition & patterning: A 100 mm diameter Borofloat 33 glass wafer with a thickness of 100 μm is used as a substrate. The low thickness wafer allows the electret to achieve a high charge density during charging.

- a-1) CYTOP is spin-coated on top of the glass wafer.
- a-2) AZ ECI 3027 positive photoresist is spin-coated on top of the CYTOP layer. A photomask is used in the lithography of the photoresist.
- a-3) Reactive ion etching (RIE) is performed. After etching, the average CYTOP layer thickness is 4 μm.
- a-4) The rotors are diced out of the wafer using a femtosecond laser. The dicing is performed before charging to ensure that the charge lost due to handling of the rotor is minimized. A laser is used for dicing as the circular shape of the rotor could not be achieved with conventional saw dicing. For laser dicing, a Lasea femtosecond laser is used. A photo of the fabricated electret rotor is shown in Figure 9.

The photomask which is used in the lithography consists of the rotor segments, as well as a set of linearly and logarithmically decreasing electret segments. The photomask is shown in Figure 15. The linear and logarithmic sets

of electret segments serve the purpose of measuring and verifying the charge density and stability after charging, which will be explained in more detail in section V.

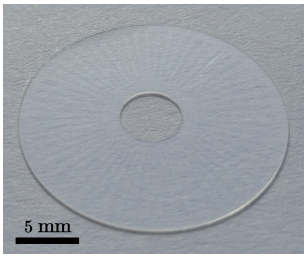

Fig. 9: Photo of the fabricated electret rotor. The segments of CYTOP are faintly visible.

2) Corona charging: The wafers are charged using a corona charging set-up. A schematic of the corona charging set-up is shown in Figure 11. The corona needle potential is equal to -8 kV, the grid potential is used as a variable to control the final charge density. The wafers are charged for 30 minutes. The distance between the needle and the grid and the distance between the grid and the electret surface is approximately 15 mm and 5 mm respectively. To ensure that the charge distribution across the wafer is homogeneous, an array of 37 needles is used, spaced 15 mm apart in a hexagonal pattern.

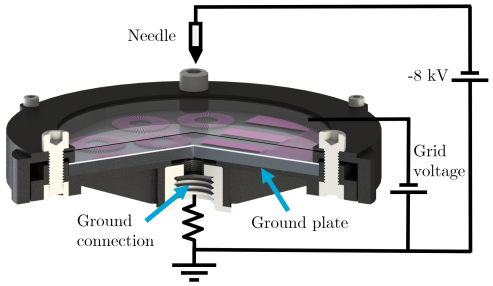

Fig. 10: Schematic section view of the corona charging set-up.

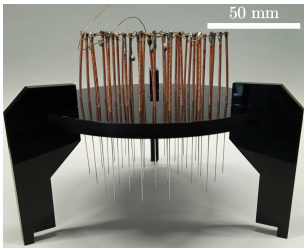

Fig. 11: Photo of the needle array that is used to create a homogeneous charge distribution.

B. Electrode stator

- b-1) The stator is fabricated by sputtering a 312 nm thick layer of high-density copper layer on glass.
- b-2) The interdigitated electrode pattern is then etched in the copper layer by femtosecond laser ablation. This results in a gap size g between the electrode pairs of 24 μm.
- b-3) Finally, the electrode is diced using a femtosecond laser in a similar way as is done for the electret rotor. A photo of the fabricated electrode stator is shown in Figure 12.

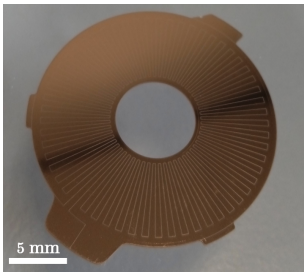

Fig. 12: Photo of the fabricated electrode stator showing the interdigitated pattern.

C. Assembly

The total assembly consists of the electret rotor, the electrode stator, a micro-ball bearing to suspend the rotor, and a base that connects the micro-ball bearing and the stator. An exploded view of all the components of the assembly is shown in Figure 13.

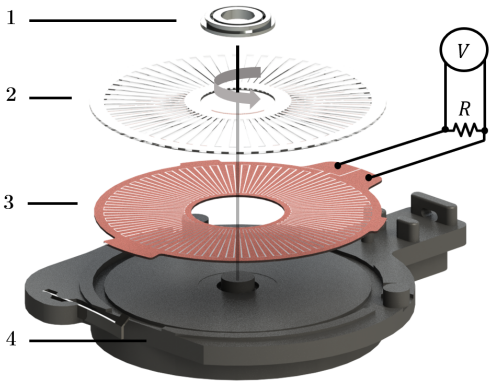

Fig. 13: Exploded view of the assembly with the ball bearing (1), the electret rotor (2), the electrode (3), and the base (4).

IV. Measurements

a) Capacitance: To measure the capacitance of the electrodes, a Voltcraft LCR-300 LCR meter is used. The

measured capacitance of the electrode is equal to 64.2 pF, in agreement with calculations performed following the analytical formula proposed by Igreja et al. for interdigitated electrodes [25]. The calculated value deviates only 11.1% from the measured value. The deviation can be attributed to the excess capacitance of the soldered connections.

b) Charge distribution and stability: To verify the charge distribution and stability, a manually operated scanning probe stage is made. The probe stage is shown in Figure 14. The TREK 341B electrostatic volt meter is used to measure the surface voltage of the electret surface after charging.

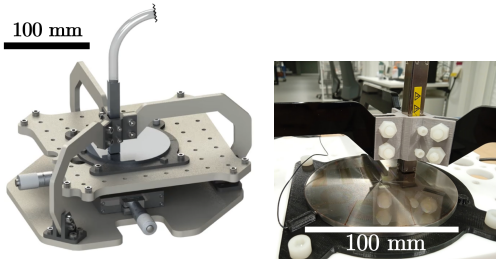

a. b.

Fig. 14: (a) Probe stage render. **(b)** Close-up photo during measurements (b).

The wafer with the patterned CYTOP electret layer is positioned on top of a Thorlabs manual XY-motion stage, allowing the wafer to move relative to the electrostatic voltmeter probe. The distance between the electrostatic voltmeter probe and the wafer surface is equal to $0.4mm \pm 0.1mm$.

As can be seen in Figure 15, the wafer consists of 5 electret rotor patterns (lower half), and two sets of electret segments that decrease in width linearly and logarithmically respectively (top half).

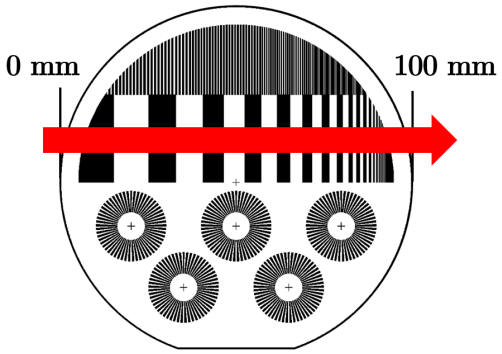

Fig. 15: Mask layout showing the electret segments (black) and the scanning direction during surface voltage measurements of the set of logarithmic electret segments (red arrow).

The sets of electret segments of widths varying from 10 mm to 25 μm allow for investigating the relation between the width of the electret segment and the chargeability and charge decay. Chargeability is defined as the affinity of electret segments to embed stable charge. The charge decay is determined by performing several measurements over time and looking at the decrease in measured surface voltage. The wafer is stored inside a wafer box in between measurements, at ambient temperature of around $21°C$ and ambient humidity of up to 70%.

By measuring the surface voltage of the sets of electret segments, the chargeability and decay of the rotor electret segments can be deduced. Because the distance between the electrostatic voltmeter probe and the electret surface is on the same order of magnitude as the width of the electret segments on the rotor, fringing fields play a role when measuring the surface voltage. Because of this, the voltmeter cannot distinguish between narrow features. The resultant measured surface voltage of narrow features will thus be an average of the surface voltage on the glass and the surface voltage on the electret segments.

c) Output power characteristics: To measure the output power characteristics of the electret transducer, wires are soldered to the contact pads of the electrodes and connected using a decade box that provides the necessary load resistance. A rheometer is then used to induce rotation of the electret rotor. A USB-6211 DAQ by National Instruments is used to record the output voltage across the load resistance. Using the output voltage and the load resistance, the power and current across the load resistance can be calculated.

V. RESULTS AND DISCUSSION

A. Corona charging of wafer

The electret wafer is first charged with the charging recipe is shown in Table IV.

TABLE IV: Corona charging recipe.

Parameter	Value	Unit
Needle Voltage	-8	kV
Grid Voltage	-300	V
Charging time	30	mins

In Figure 16, the measured surface voltage of the set of logarithmic CYTOP electret segments for several moments in time after charging is shown. What can be seen is that a stable pattern of charge is achieved successfully. The surface voltage of the electret segments is approximately equal to -100 V. For an electret width equal to or narrower than 500 μm, the voltmeter cannot distinguish between features and the measured surface voltage is the average voltage of the glass surface and the electret segment, as described in paragraph IV-.0.b.

The stable surface voltage of the electret is significantly lower than the grid voltage. The reason for the lower stable surface voltage of the unipolar electret is most likely due to the phenomenon of floating charge, as described by Zhang et al. [23]. Floating charge is charge that is loosely deposited

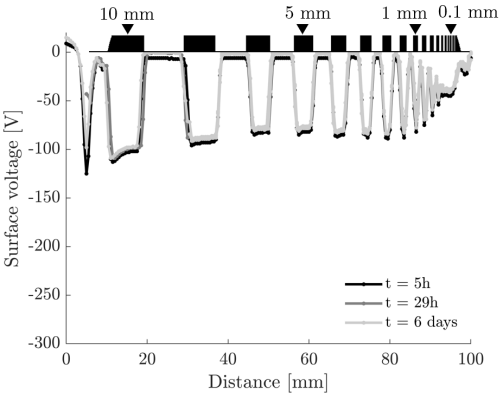

Fig. 16: Surface voltage at several moments in time of the set of logarithmic electret segments. A stable pattern of charge is achieved successfully.

on top of the electret surface and thus does not penetrate the electret. This floating charge masks the electret and prevents further charging. This floating charge does not occur with conventional electrets. The reason that floating charge occurs during the charging of the unipolar electret and not during the charging of conventional electrets is theorized to be caused by the lower electric field strength inside the unipolar electret during charging. The dielectric substrate increases the total dielectric thickness and thus decreases electric field strength inside the electret. For an identical grid voltage, the electric field inside the unipolar electret is approximately five times lower than that of a conventional electret.

$$\frac{E_{d.uni}}{E_{d.conv}} = \frac{\epsilon_s d}{\epsilon_s d + \epsilon_d d_s} = 0.19 \tag{11}$$

Where $E_{d.uni}$ is the electric field inside the unipolar electret during charging and $E_{d.conv}$ is the electric field inside the conventional electret during charging.

B. Corona charging with revised charging recipe

Figure 16 shows that charge patterning is possible, but to achieve an electret transducer with the maximum possible output power, a higher charge density is necessary. To achieve this higher charge density, a revised charging recipe is used, that uses a higher grid voltage, as can be seen in Table V.

TABLE V: Revised corona charging recipe.

Parameter	Value	Unit
Needle Voltage	-8	kV
Grid Voltage	-1.5	kV
Charging time	30	mins

The grid voltage is increased fivefold to achieve as high of an electric field as with the conventional electret as shown in Equation 11. If the decreased chargeability of the unipolar electret can indeed be attributed to a lower electric field strength, increasing the electric field should result in an improved chargeability.

The measured surface voltage after charging according to the revised recipe is shown in Figure 17. Electret segments down to a width of $100\mu m$ are effectively charged. With a higher grid voltage, a higher stable surface voltage is achieved. The ratio between the stable surface voltage and the grid voltage is equal to what was found in subsection V-A, and approximately one third. This indicates that the electric field strength inside the electret is not the sole reason for the occurrence of floating charge, as the electric field strength inside the electret during charging is as high as in the conventional electret design, but floating charge still occurs. This suggests that the implantation of charges of opposite polarity is an important factor in the chargeability of an electret, but further research is necessary to fully explain the phenomenon of floating charge.

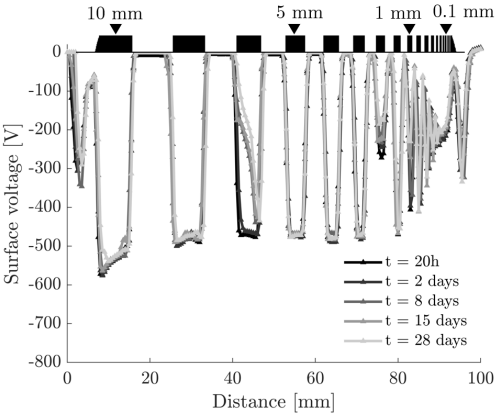

Fig. 17: Surface voltage at several moments in time of the set of logarithmic electret segments after charging with the revised charging recipe.

What can also be seen in Figure 17 is that there is a peak in surface voltage at the edge of the wafer, at around 5 mm and 95 mm. The reason for this is that during charging, ions are accelerated to the edge of the wafer as here there is a small gap between the charging housing and the wafer, allowing the ions to go directly to the ground. This leads to a high density of ions here, resulting in more charge implantation near the edge of the wafer. For several electret segments, at around 50 mm, and 75 mm, an increased rate of discharge occurs. This can most likely be attributed to contamination of the wafer during surface voltage measurements.

In Figure 18, the difference in chargeability as a function of the width of the electret segments can be seen for electret segments ranging from a width of $500\mu m$ down to $100\mu m$. There is a weak dependency of the chargeability as a result of the electret segment width. As the electret segments get more narrow, their stable surface voltage decreases.

In Figure 19, the average surface voltage over time,

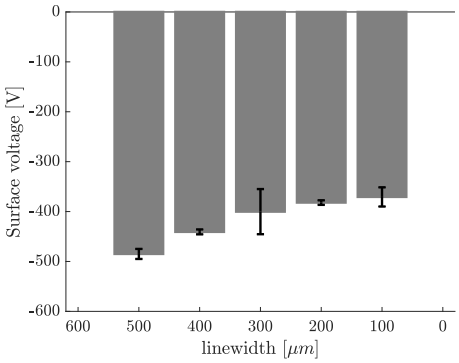

Fig. 18: Surface voltage of narrow electret segments after charging with the revised recipe. The error bars indicate the standard deviation of each measurement.

normalized to the initial surface voltage of the set of electret segments is shown. What can be seen is that a logarithmic decreasing trend is visible, with the rate of charge decay decreasing over time. The small uptick in surface voltage at 15 days is most likely due to a deviation of the measurements, and not an actual increase of surface voltage. A relation between the electret segment width and charge decay cannot be statistically proven with the unipolar electret concept. The voltage decreases by no more than 5 % over a period of 28 days, which is significantly better than the results for conventional patterned electrets of previous published work, such as the work by Crovetto et. al [17]. Crovetto et. al found a decrease in surface voltage of 83% over the course of 21 days for conventional patterned CYTOP (CTL-M) electret of a width of 200 μm.

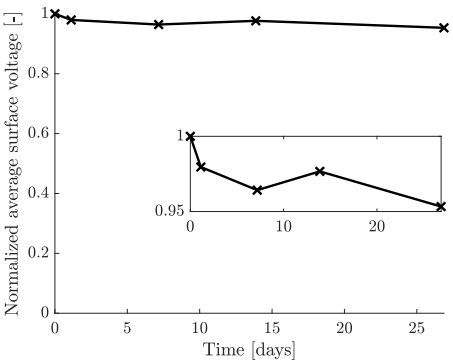

Fig. 19: Normalized average surface voltage across the set of logarithmic electret segments. In the center right of the figure, a close-up can be seen. The total charge decay is not more than 5% over the course of 28 days at ambient temperature and humidity.

C. Corona charging of individual rotor

Individual rotors are charged according to the revised charging recipe as stated in Table V. An adapted aluminium ground plate is fabricated for the charging of individua lrotors. The part of the ground plate which is not covered by the electret rotor is shielded using PMMA inserts, preventing a direct path to the ground during charging. A schematic section view of the aluminium ground plate with the PMMA inserts is shown in Figure 20.

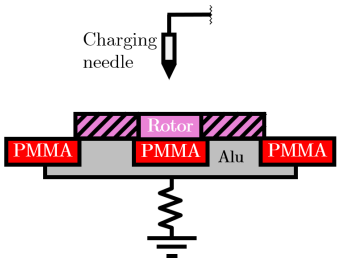

Fig. 20: Schematic showing a section view of the electret rotor (pink) on top of the aluminium ground plate (grey) with the PMMA inserts (red) used to shield the ground plate.

The scanning probe stage is used to scan the surface of the electret rotor after charging. The rotor surface is raster scanned and the voltage is recorded every 2 mm. The result of the raster scan is shown in Figure 24. When comparing the pattern of electret segments shown in Figure 21a with the measured surface voltage shown in Figure 23c, it is clear that the voltmeter cannot distinguish between individual features.

The average measured voltage across rotor is 177 V. This means that the average electret voltage, which is approximately equal to twice the average voltage, as only the electret segments contain stable charge, is 354 V. This is slightly lower than the results in Figure 18. This can be attributed to small gaps between the electret rotor and the aluminium ground ring, creating a direct path to ground for the ions during charging, reducing the local chargeability of the electret segments. As a result, the surface voltage is not homogeneous across the rotor.

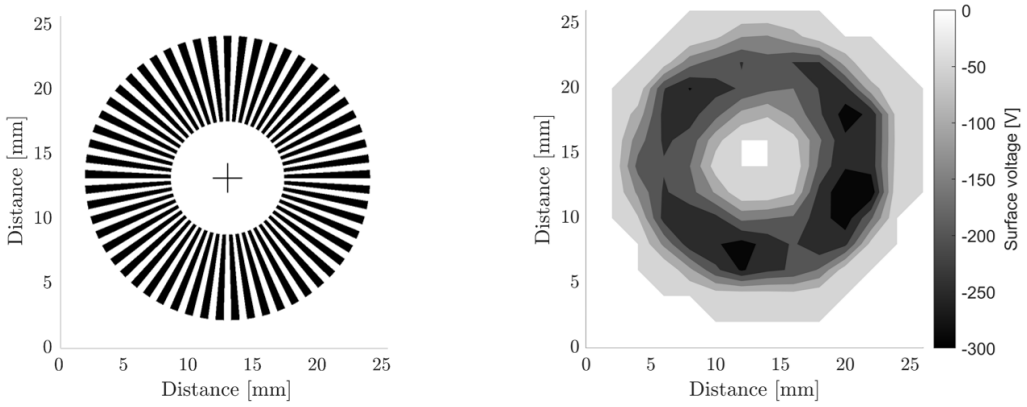

(a) **(b)**

Fig. 21: **(a)** Rotor CYTOP segments shown in black for reference. **(b)** Measured surface voltage across the rotor.

D. Calculation results of the output characteristics

Using the parameters of the fabricated micro-electret transducer as stated in Table III, the amplitude of the charge distribution can be calculated. This results in the following charge amplitude.

$$\frac{\tilde{A}}{\sigma_0} \approx 0.237 \tag{12}$$

Using the charge amplitude, the transducer parameters stated in Table III, and the surface charge density calculated using the voltmeter measurements in Equation 9, the output power characteristics of the micro-electret transducer can be determined.

1) Comparison of the novel unipolar electret transducer and a conventional electret transducer: In Figure 22, the predicted RMS output power as a function of the load resistance at a fixed angular velocity of 20π rad/s of the designed unipolar electret transducer is compared with the predicted output power of a conventional electret charged to the same surface voltage of 354 V. What is found is that the novel unipolar electret outperforms the conventional electret when it comes to output power by a factor of four.

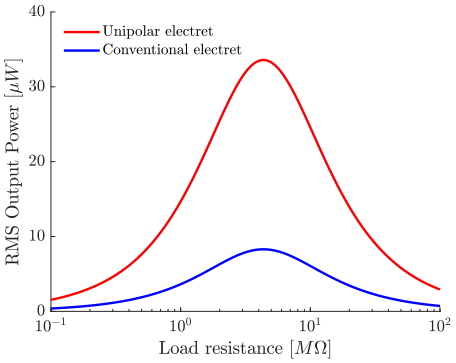

Fig. 22: Predicted RMS output power, as a function of the load resistance at a fixed angular velocity of 20π rad/s for the novel unipolar electret (red) and a conventional electret (blue) charged to the same surface voltage of 354 V according to the novel model.

2) Comparison of the novel model and the conventional model predictions: In Figure 23a, the voltage waveform of the conventional model and the novel model are plotted for a rotational velocity ω of 20π rad/s and a matched load resistance of $R_m = \frac{1}{\omega n C} = 2.733 M\Omega$. This calculation result is then compared with the conventional model predictions. What can be seen is that the conventional model shows a significantly higher peak-to-peak output voltage.

In Figure 23b, the calculated maximum RMS output power is shown as a function of the load resistance, at a fixed angular velocity of 20π rad/s. The maximum output power occurs when the load resistance is equal to the matched load resistance R_m. When comparing the output power

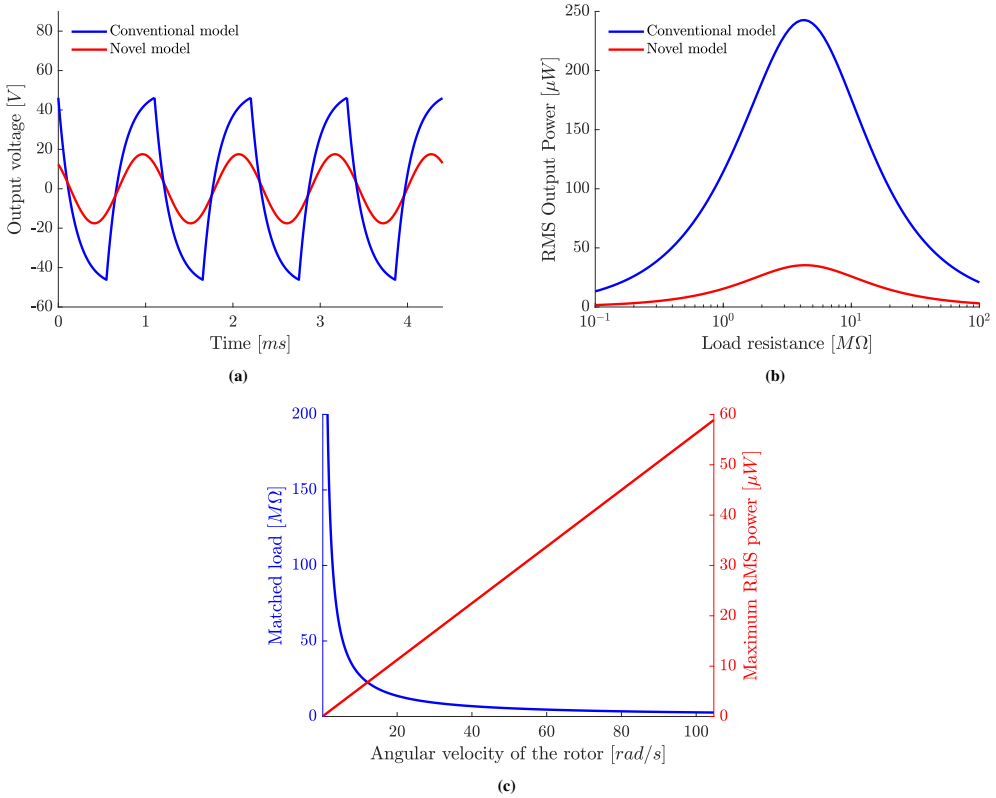

Fig. 23: Calculated output power characteristics of the fabricated unipolar micro-electret transducer. **(a)** Output voltage waveform at matched load for a rotational velocity of 20 π rad/s at matched load according to the conventional model (blue) and the novel model (red). **(b)** RMS output power according to the conventional model (blue) and the novel model (red), as a function of the load resistance for a rotational velocity of 20π rad/s. **(c)** RMS output power, as a function of the rotational velocity for matched load.

predictions of the conventional and the novel model, a similar trend can be seen, with a peak in output power at the same load resistance. The difference being that the maximum calculated output power of the device is a factor 7.4 higher using the conventional model.

In Figure 23, the calculated RMS output power at matched load is shown as a function of the angular velocity of the rotor. What can be seen is that at matched load, the output power scales proportionally with the angular velocity. The matched load scales inversely proportional to the rotational velocity.

E. Measurement results of the output power characteristics

In Figure 24a, the output voltage waveform of the assembled transducer at 100 rad/s and a matched load resistance of 2.733 $M\Omega$ is shown contrasted with the novel model. The shape of the waveform closely resembles the sinusoidal output voltage of the model. The amplitude of the measurement waveform is approximately 64% of the amplitude of the novel model prediction. The measured voltage amplitude is equal to $10.8V$.

In Figure 24b, the measured maximum RMS output power as a function of the load resistance at a fixed angular velocity of 20π rad/s is shown. When comparing the output power measurement with the predictions of the novel model, a similar trend can be seen, with a peak in output power at the same load resistance. The measured output power of 17.7 μW is approximately half the magnitude of the novel model prediction, which is 33.6 μW at a load resistance of 4.349 $M\Omega$. When comparing the measurement results in Figure 24b with the conventional model predictions in Figure 23b, it can be seen that the conventional model overestimates the output power of the electret transducer by a factor of 15. This shows that the novel model is significantly more accurate.

In Figure 24c, the measured RMS output power at

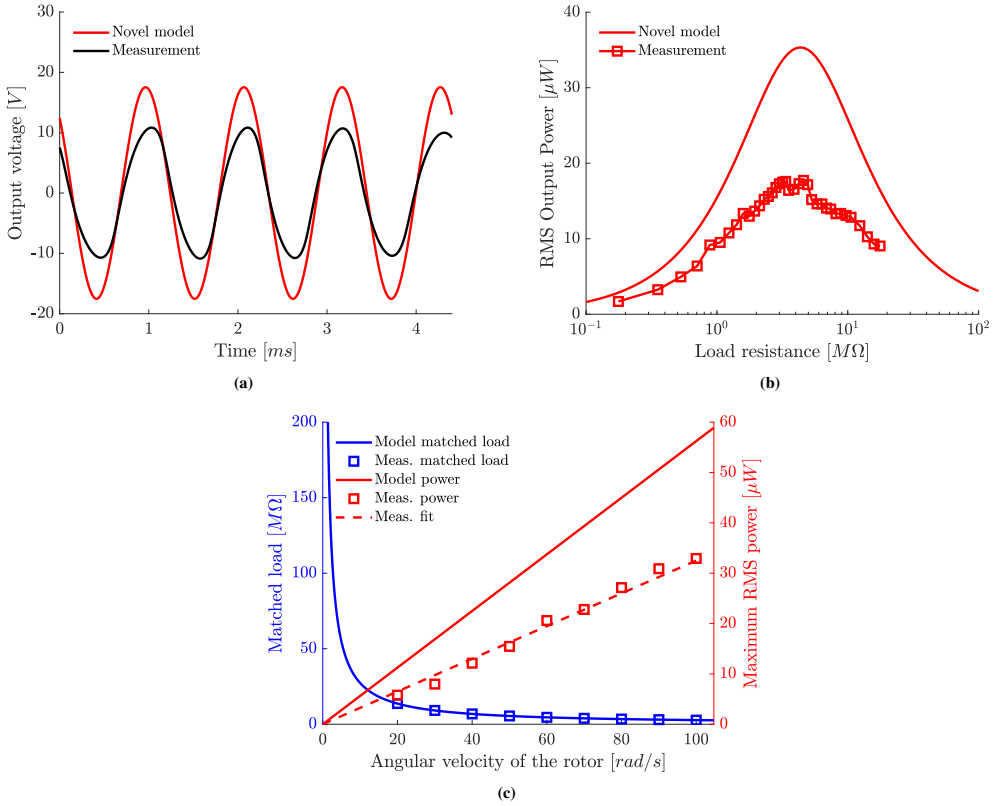

Fig. 24: Comparison between the novel model output power characteristics and the measured output power characteristics. **(a)** Voltage waveform according to the novel model (red) and measurements (black) at a fixed angular velocity of 100 rad/s and a matched load resistance of 2.733 $M\Omega$. **(b)** RMS output power as function of the load resistance at a fixed angular velocity of 20π rad/s according to the novel model (solid line) and measurements (markers). **(c)** RMS output power, as a function of the rotational velocity at matched load according to the novel model (solid line) and measurements (markers).

matched load is shown as a function of the angular velocity of the rotor. The measured RMS output power scales proportionally with the angular velocity of the rotor, just like the model prediction. Again, the measured output power is approximately half the magnitude of the novel model prediction.

F. Factors causing overestimation of the output power

The reason for the consistent overestimation of the output power by the novel model can be attributed to several factors.

- **Difference in gap between rotor and stator:** A deviation in effective gap size from the design gap size of $100\mu m$ can result in a larger value of r, and thus a smaller charge amplitude A. The following factors can attribute to this difference in gap size.
  1) Angular misalignment: Because the gap size is only 100 μm and the rotor has a diameter of $20mm$, a slight angular misalignment can lead to a large deviation in gap size.
  2) Axial misalignment: Due to the limited resolution of the 3D printer, a deviation of up to $28\mu m$ in axial alignment is expected, leading to a deviation in gap size.
  3) Warp of the rotor: Due to the extremely thin substrate, the rotor is not very stiff. Stresses induced by the CYTOP coating and the laser cutting have been seen to lead to warp of the rotor. This rotor warp results in a deviation in effective gap size.
- **Parallel misalignment:** Due to the limited resolution of the 3D printer, up to $42\mu m$ in parallel misalignment is expected. This parallel misalignment leads to a decreased charge difference between the electrodes, reducing the output power.

- **Charge loss during handling and assembly:** During handling and assembly, the rotor has to be manipulated and carefully attached to the micro-ball bearing. As the surface voltage is measured before assembly, the effects of charge loss during handling and assembly are not taken into account.

To get a quantitative insight into the influence of these factors, the output power as a function of the load resistance at an angular velocity of 20π rad/s is compared between the model predictions for several values of the gap size z and the surface voltage V_s and the measurements in Figure 25. An increase in effective gap size of $50\mu m$, a decrease in surface voltage of 30%, or a combination of the two results in a model prediction that very closely follows the measurements.

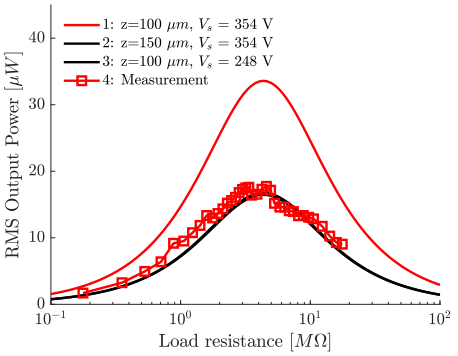

Fig. 25: RMS output power, as a function of the load resistance at a fixed angular velocity of 20π rad/s.
1: According to the novel model predictions for the design gap size (z=100 μm) and the surface voltage as measured ($V_s = 354V$).
2: According to the novel model predictions for a 50 μm increase in gap size (z=150 μm) and the surface voltage as measured ($V_s = 354V$).
3: According to the novel model predictions for the design gap size (z=100 μm) and a 30% decrease in surface voltage ($V_s = 248V$).
4: Measurements.

VI. CONCLUSION

In this work, a novel unipolar electret design is proposed. In this novel design, the electret is deposited on a dielectric substrate. This allows the electret to contain charges of only one polarity, as opposed to the conventional bipolar electrets. This unipolar electret can be used to significantly improve the magnitude of charge it can induce on a counter electrode, as its generated electric field is fully directed towards the counter electrodes. This increased induced charge magnitude results in a higher output power of an electret transducer. Further benefits include better charge stability, simple fabrication, and reduced risk of dielectric breakdown in air.

The unipolar electret concept is verified in two ways. First, a glass wafer with CYTOP electret segments of widths varying from 10 mm to 25 μm is fabricated. This wafer is charged using a corona charging set-up. By measuring its surface voltage, the relation between electret segment width, chargeability, and charge stability is explored. Stable charge has been achieved for electret segments with a width down to 100 μm. The chargeability of the unipolar electret is lower than the conventional electret design, with a stable surface voltage of approximately one-third of the grid voltage. This reduced chargeability can be compensated by applying a higher grid voltage during charging. The reason for this worse chargeability of the unipolar electret concept cannot be attributed to the electric field strength in the electret during charging and should be explored further.

The charge stability of the patterned unipolar electret is found to outperform comparable conventional patterned electrets, losing less than 5 % of its charge after a period of 28 days. A relation between the electret width and charge stability could not be statistically proven. The improved charge stability of the novel unipolar electret can be attributed to more efficient use of the charge embedded in the electret and to the omission of a conductive substrate, which in the conventional electret leads to a high electric field resulting in charge mobility and recombination of charges.

The second way in which the unipolar electret concept is verified is through the fabrication of a rotational micro-electret transducer consisting of 57 electret segments using the unipolar electret design. The fabricated micro-electret transducer achieves a voltage amplitude of 10.8 V at an angular velocity of 100 rad/s and a matched load resistance of 2.733 $M\Omega$, and an RMS output power of 17.7 μW at an angular velocity of 20π rad/s and a matched load resistance of 4.349 $M\Omega$. The fabricated micro-electret transducer shows that a unipolar micro-electret transducer can successfully generate power.

REFERENCES

[1] T. Fernández-Caramés and P. Fraga-Lamas, "Towards the internet of smart clothing: A review on iot wearables and garments for creating intelligent connected e-textiles," vol. 7, p. 405, 12 2018.
[2] A. Mohanty, S. Parida, R. Behera, and T. Roy, "Vibration energy harvesting; a review," *Journal of Advanced Dielectrics*, vol. 9, 08 2019.
[3] S. Beeby and N. White, "Energy harvesting for autonomous systems," vol. 308, 01 2010.
[4] S. Roundy, "Energy scavenging for wireless sensor nodes with a focus on vibration to electricity conversion," 01 2003.
[5] H. S. Kim, J.-H. Kim, and J. Kim, "A review of piezoelectric energy harvesting based on vibration," *International journal of precision engineering and manufacturing*, vol. 12, no. 6, pp. 1129–1141, 2011.
[6] A. Toprak and O. Tigli, "Piezoelectric energy harvesting: State-of-the-art and challenges," *Applied Physics Reviews*, vol. 1, no. 3, p. 031104, 2014.
[7] S. Boisseau, G. Despesse, T. Ricart, E. Defay, and A. Sylvestre, "Cantilever-based electret energy harvesters," *Smart Materials and Structures*, vol. 20, no. 10, p. 105013, 2011.
[8] Y. Suzuki, "Recent progress in mems electret generator for energy harvesting," *IEEJ Transactions on Electrical and Electronic Engineering*, vol. 6, no. 2, pp. 101–111, 2011.
[9] G. M. Sessler and J. E. West, "Electroacoustic transducer," Jan 1964.
[10] M. Kiziroglou, C. He, and E. Yeatman, "Non-resonant electrostatic energy harvesting from a rolling mass," pp. 318 – 321, 07 2008.
[11] H. C.-H. K. H.-D. . Y. J.-B. Choi, Dong-Hoon, "Liquid-based electrostatic energy harvester with high sensitivity to human physical motion.," *Smart Materials and Structures*, vol. 20, 2011.

[12] P. Basset, D. Galayko, F. Cottone, R. Guillemet, E. Blokhina, F. Marty, and T. Bourouina, "Electrostatic vibration energy harvester with combined effect of electrical nonlinearities and mechanical impact," *Journal of Micromechanics and Microengineering*, vol. 24, 02 2014.
[13] L. Bu, X. Wu, X. Wang, and L. Liu, "Non-resonant electrostatic energy harvester for wideband applications," *Micro & Nano Letters*, vol. 8, no. 3, pp. 135–137, 2013.
[14] M. Bi, S. Wang, X. Wang, and X. Ye, "Freestanding-electret rotary generator at an average conversion efficiency of 56%: Theoretical and experimental studies," *Nano Energy*, vol. 41, pp. 434–442, 2017.
[15] J. Nakano, K. Komori, Y. Hattori, and Y. Suzuki, "MEMS rotational electret energy harvester for human motion," *Journal of Physics: Conference Series*, vol. 660, p. 012052, dec 2015.
[16] Y. Suzuki, D. Miki, M. Edamoto, and M. Honzumi, "A MEMS electret generator with electrostatic levitation for vibration-driven energy-harvesting applications," *Journal of Micromechanics and Microengineering*, vol. 20, p. 104002, sep 2010.
[17] A. Crovetto, F. Wang, and O. Hansen, "An electret-based energy harvesting device with a wafer-level fabrication process," *Journal of Micromechanics and Microengineering*, vol. 23, p. 114010, oct 2013.
[18] K. C. Kao, "Dielectric phenomena in solids : with emphasis on physical concepts of electronic processes," 2004.
[19] T. Tsutsumino, Y. Suzuki, N. Kasagi, and Y. Sakane, "Seismic power generator using high-performance polymer electret," vol. 2006, pp. 98 – 101, 02 2006.
[20] W. Olthuis and P. Bergveld, "On the charge storage and decay mechanism in silicon dioxide electrets," *IEEE Transactions on Electrical Insulation*, vol. 27, no. 4, pp. 691–697, 1992.
[21] J. Boland, Y.-H. Chao, Y. Suzuki, and Y. Tai, "Micro electret power generator," in *The Sixteenth Annual International Conference on Micro Electro Mechanical Systems, 2003. MEMS-03 Kyoto. IEEE*, pp. 538–541, IEEE, 2003.
[22] H. Okamoto, T. Onuki, and H. Kuwano, "Improving an electret transducer by fully utilizing the implanted charge," *Applied Physics Letters*, vol. 93, pp. 122901–122901, 09 2008.
[23] J. Zhang, X. Zou, and Y. Zhang, "Improvement of the performance of the pecvd sio2/si3n4 double-layer electrets," *IEEE Transactions on Dielectrics and Electrical Insulation*, vol. 18, no. 2, pp. 456–462, 2011.
[24] Y. Wada, Y. Hamate, S. Nagasawa, and H. Kuwano, "Aging characteristics of electret used in a vibration-based electrostatic induction energy harvester," *2011 16th International Solid-State Sensors, Actuators and Microsystems Conference*, pp. 2626–2629, 2011.
[25] R. Igreja and C. Dias, "Analytical evaluation of the interdigital electrodes capacitance for a multi-layered structure," *Sensors and Actuators A: Physical*, vol. 112, no. 2, pp. 291–301, 2004.

6

OUTLOOK

In this chapter, a design for an entire energy harvester is proposed, incorporating a unipolar micro-electret transducer. First, changes to the micro-electret transducer design are proposed based on the findings of chapter 4 and chapter 5. Then, the novel electrostatic model verified in chapter 4 will be incorporated into a dynamic model. Accelerations from computer work, walking, and running will be used as the input motion for the energy harvester model. The dynamic model solves the equations of motion, which include the influence of the micro-electret transducer. The output power characteristics of the micro-electret transducer are then calculated as a result of these wearer activities. The dynamic model shows that it is feasible to generate approximately twice as much energy as a quartz watch consumes for a day of the median wearer.

6.1. ADAPTATIONS TO THE EXPERIMENTAL PROTOTYPE

The findings of chapter 4 and chapter 5 show that the experimental prototype of the micro-electret transducer works in line with model expectations. However, in its current design, it is not yet directly applicable as a transducer inside a quartz watch. To get closer to a design of an electret transducer that can be applied inside quartz watches, several changes have to be made to the experimental prototype.

6.1.1. SUSPENSION

The experimental verification thus far is limited to the transducer itself. The mechanical design has not been taken into account, and thus the experimental verification does not include a watch rotor. The watch rotor is the component of a watch that consists of an eccentric mass that rotates due to the motion of the wearer. An example of a watch rotor can be seen in Figure 6.1. Watch rotors are usually suspended using small ball bearings. These ball bearings are relatively cheap components that have large tolerances.

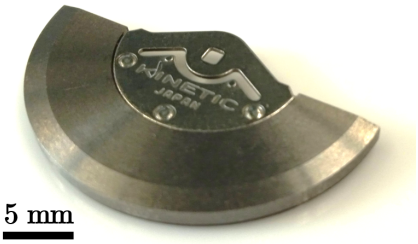

Figure 6.1: Photo of a Seiko AGS watch rotor.

As the tolerances of the electret transducer rotor need to be small, it would be good to decouple the suspension of the watch rotor from the suspension of the electret rotor. This can be done by connecting the watch rotor with the electret rotor through a gear transmission. An added benefit is that the gear transmission can be used to amplify the angular velocity of the electret rotor. A higher angular velocity of the electret rotor leads to higher output power, as shown in chapter 4. Efforts can also be made to better integrate the electret transducer inside a watch movement. In the experimental prototype, the electret rotor is suspended using a micro ball bearing. Ball bearings are relatively large and have large tolerances. For the forenamed reasons, jewel bearings should be used to suspend the electret rotor. Jewel bearings are plain bearings made out of synthetic sapphire or synthetic ruby. Jewel bearings are used in precision instruments where low friction, long life, and dimensional accuracy are important, and have thus been used in the watch industry for centuries to suspend moving parts. In Figure 6.2, a close-up photo of a jewel bearing, and jewel bearings inside a mechanical watch is shown.

6.1.2. ELECTRODE SUBSTRATE

The substrate material of the prototype electrode is D263M glass. D263M glass has a relative permittivity of 6.7, resulting in high capacitance. Replacing the substrate with a

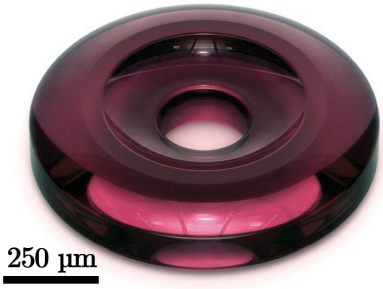

a.

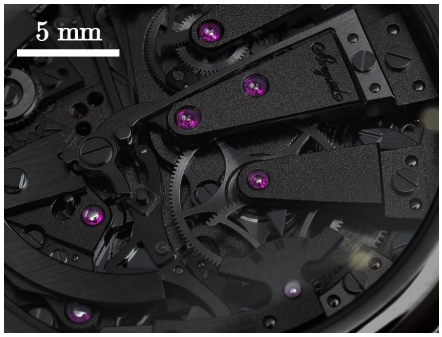

b.

Figure 6.2: Close-up photo of a jewel bearing made from synthetic sapphire (a) and jewel bearings inside a mechanical watch movement (b). (Courtesy of Monochrome Watches [25])

high-frequency PTFE PCB substrate with a relative permittivity of 2 can reduce the capacitance by a factor of 2.6 [26]. The output power of electret transducers scales inversely proportional to the capacitance, increasing the output power by a factor of 2.6 as well.

6.1.3. GRID VOLTAGE

Finally, a higher grid voltage can be used to increase the surface voltage of the electret, and thus the electret charge density. This would result in Paschen's limited design, the ultimate limit of the induced charge. Maximizing the induced charge will lead to a higher electromechanical coupling, and thus a larger output power.

6.2. DYNAMIC MODEL

A dynamic model is made to simulate how the unipolar micro-electret transducer would perform inside a watch in combination with the mechanical design. The dynamic model is structured around the equations of motion for the watch rotor. The watch rotor parameters of interest are the mass m, the eccentricity of the center of mass r_m, and the moment of inertia around its point of rotation I_m. For the watch rotor parameters, the Seiko AGS eccentric proof mass is used as a reference. The parameters are shown in Table 6.1.

Table 6.1: Rotor parameters used in the dynamic model.

Parameter	Value	Description
m	4.66 $[g]$	Mass
r_m	7.01 $[mm]$	Center of mass relative to point of rotation
I_m	293 $[g \cdot mm^2]$	moment of inertia

The following equation of motion is to be solved.

$$I_m \cdot \alpha = m \cdot r_m \cdot cos(\theta) \cdot a_y - sin(\theta) \cdot a_x - (c(\omega, t) + c_m) \cdot sgn(\omega) \tag{6.1}$$

Where α is the angular acceleration, θ is the angle of the proof mass, a_y is the acceleration in the y-direction, and a_x is the acceleration in the x-direction. The x- and y-directions are defined according to the axis system fixed to the wrist shown in Figure 6.3. $c(\omega, t)$ is the electromechanical coupling, $c_m(\omega)$ is the mechanical damping, and ω is the angular velocity.

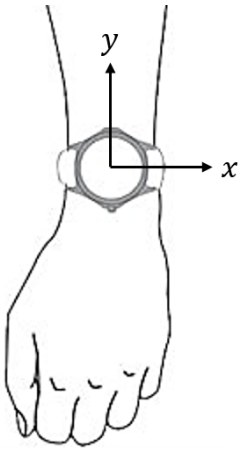

Figure 6.3: Axis system used in the dynamic model.

The acceleration data are collected using accelerometers attached to the wrist of a test subject. Acceleration data acquired from computer work, walking, and running are used to give an overview of the performance under different wearer activities. The electromechanical coupling can be calculated using the power extracted from the system by the transducer.

$$c(\omega, t) = \frac{P(\omega, t)}{\omega} \tag{6.2}$$

The output power can be calculated for a given value of ω and t by plugging these values into the transducer output current equation in chapter 4, adapted to include the transmission ratio ρ. From this expression for the output current, the output power can be calculated.

$$i(\omega, t) = \frac{2AS_0 n\omega\rho}{\pi R^2 C^2 n^2 \omega^2 \rho^2 + \pi}(n\omega\rho RCcos(n\omega\rho t) - sin(n\omega\rho t)) \Longrightarrow P(\omega, t) = i(\omega, t)^2 R \tag{6.3}$$

c_m is the mechanical friction due to friction losses in the system, which is approximated by comparing the impulse response of a watch rotor with the impulse response of the model. In this way, a coulomb friction value of $15\mu Nm$ is found.

By numerically integrating Equation 6.1 with respect to time, ω and θ can be calculated. The numerical model is graphically shown in a flowchart in Figure 6.4. The goal of this model is to find the transducer parameters that result in the largest output power and to quantify this output power. There are several constraints to the design.

- The outer radius of the generator r_o should stay below 6 mm to ensure that the transducer fits inside a watch movement.

- The gap distance z between the electret and the electrode should not be smaller than $50\mu m$ to ensure that tolerances necessary to manufacture the transducer are not excessively stringent.

- The gear ratio ρ should stay below 20 to ensure that the gear transmission is not excessively large or expensive to fabricate.

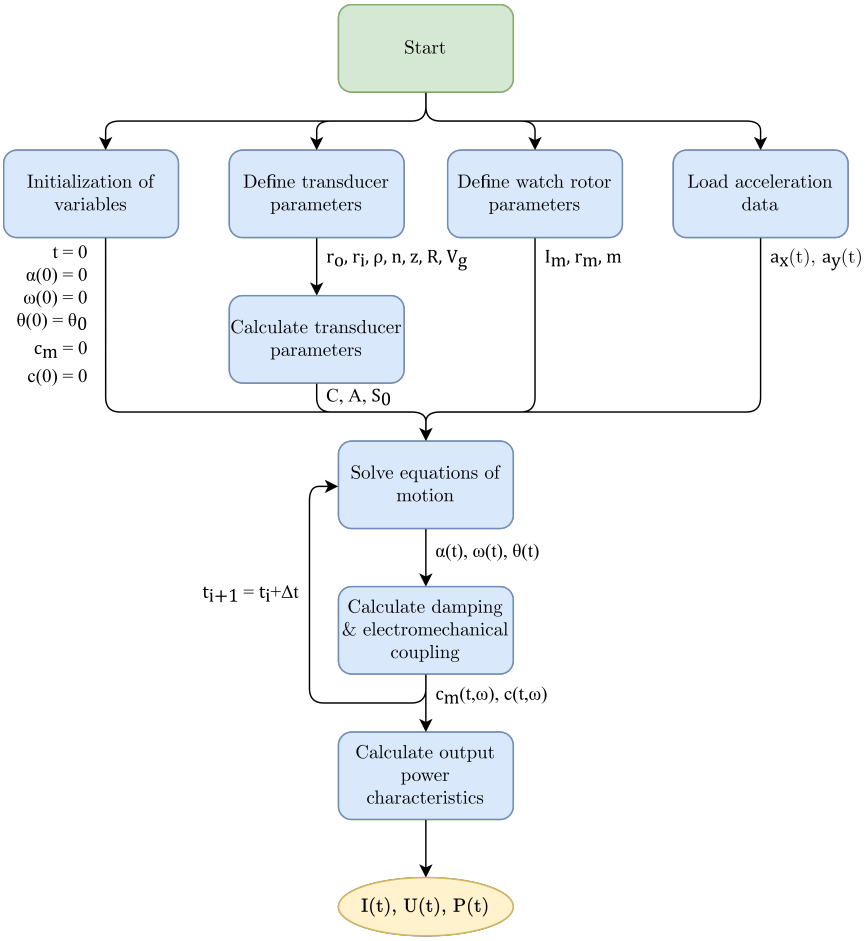

Figure 6.4: Flowchart showing the operations performed in the numerical model necessary to calculate the output power characteristics.

6.3. MODEL RESULTS

Through iteration, the micro-electret transducer parameters are adjusted between said constraints to maximize the output power. The parameters that result in the highest output power can be found in Table 6.2.

Table 6.2: Generator parameters that result in highest output power.

Parameter	Value	Description
r_o	6 $[mm]$	Outer radius generator
r_i	2 $[mm]$	Inner radius generator
g	10 $[\mu m]$	Gap between electrode pairs
ρ	20 [-]	Gear ratio
n	50 [-]	Number of electret segments
z	50 $[\mu m]$	Distance between electret and electrodes
R	1 $[M\Omega]$	Load resistance
V_s	600 $[V]$	Electret surface voltage

In Figure 6.5, the voltage-time signal of the transducer can be seen for a ten-second time signal of walking accelerations.

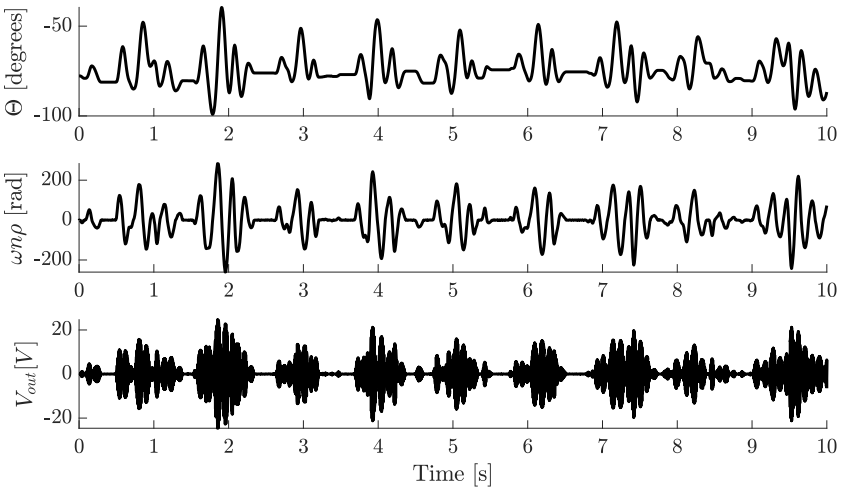

Figure 6.5: Time signals of the optimized electret transducer during the walking motion. Top: Angular displacement of the watch rotor (Θ). Middle: Angular velocity of the electret rotor ($\omega n\rho$). Bottom: output voltage of the electret transducer (V_{out}).

A quartz watch movement uses approximately $3\mu W$ of power [8]. This amounts to an energy usage of 259 mJ per day. This means that the electret transducer should generate 259 mJ in a day on average to ensure that the watch will keep running. Using these data, the time it takes to practice activity to recharge the watch battery can be determined. The result can be seen in Table 6.3.

Table 6.3: Output power and time to recharge the battery per day based on the wearer's activity .

Activity	**Output power** [μW]	**Time to recharge battery** *hours per day*
Computer work	8.78	6.3
Walking	22.3	2.5
Running	447	0.12

Johansson et al. studied the time spent on certain activities through a cross-sectional analysis of accelerometer data from 1670 adults. It was found that the median time walking, running, standing, and sedentary was 82.6, 0.1, 182.5, and 579.1 min/day, respectively [27]. If it is assumed that the power generated by the transducer during computer work is the same as for standing and sedentary, a calculation can be made of the total energy generated in a day.

$$E_{day} = P_{comp.} \cdot t_{comp.} + P_{walk.} \cdot t_{walk.} + P_{run.} \cdot t_{run.} = 514 mJ \tag{6.4}$$

Where E_{day} is the energy generated in an average day of wearing the watch, $P_{comp.}$, $P_{walk.}$, and $P_{run.}$ is the average power generated whilst doing computer work, walking, and running respectively. $t_{comp.}$, $t_{walk.}$, and $t_{run.}$ are the average times spent doing computer work, walking, and running respectively.

It is found that an average of 514 mJ is generated, which is approximately double the necessary energy to power a quartz watch. This shows that the unipolar micro-electret transducer is a viable transducer for powering quartz watches. In Figure 6.6, a visualization of the electret transducer including the watch rotor, the gear transmission, and the jewel bearing suspension is shown. The outline of the total size of the watch movement is shown as the semi-transparent footprint.

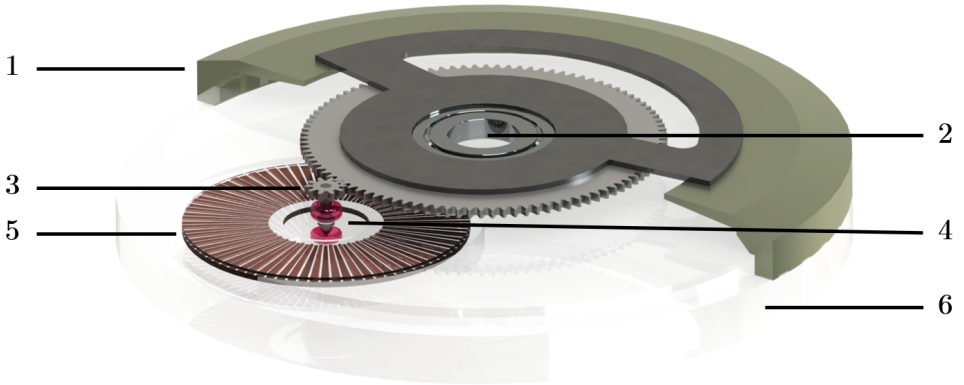

Figure 6.6: Render of the energy harvester containing the micro-electret transducer using optimized parameters highlighting the component showing the watch rotor (1), the micro-ball bearing (2), the gear transmission (3), the jewel bearing suspension of the electret rotor (4), the electret rotor & electrode stator (5) and the outline of the whole watch movement (6).

7

Reflection, Conclusions, and Recommendations

This chapter provides an overview of all activities performed throughout this research. The entire process is being reflected upon and the most important conclusions are drawn. Furthermore, future research recommendations are listed.

7.1. PROJECT OVERVIEW

To get a clear overview of the entire process of this thesis, the main research activities and their relations are shown in an overview in Figure 7.1.

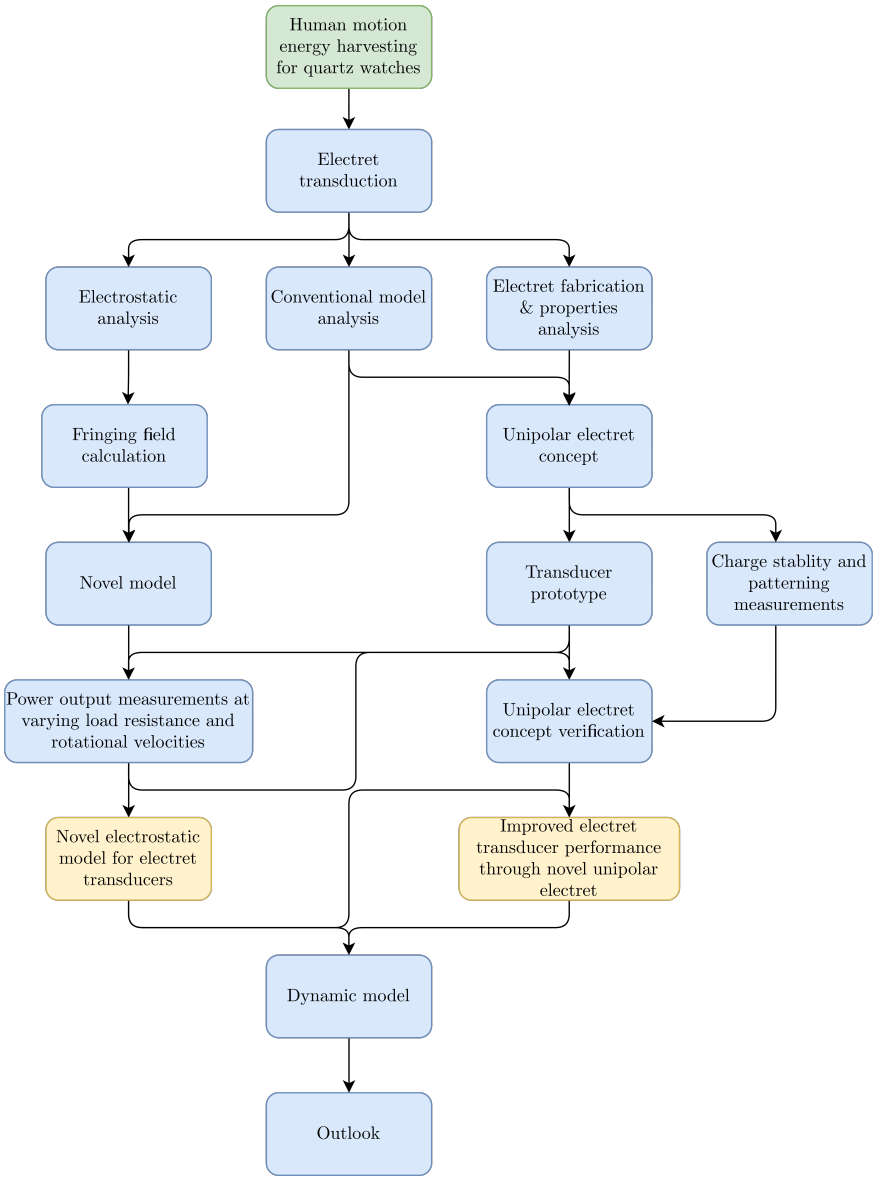

Figure 7.1: Overview of activities during the project. Green indicates the main focus of this thesis, which is also the topic of the literature review, blue indicates the research activities, and yellow indicates articles.

7.2. LEARNING PROCESS

The start of the thesis project was difficult. The topic for the literature review was human motion energy harvesting for quartz watches. During the literature review, an effort was made to categorize energy harvesters and describe the essence of their working principles. Very quickly it was found that the field of energy harvesting is broad, and further sectioning of the thesis works had to be done. The decision was made to focus on the transduction mechanism, as this is the most fundamental component of an energy harvester, and because there are clear limitations of the current designs that could be improved upon.

From the literature review, electret transduction was identified as a promising alternative to conventional electromagnetic transduction. As electret transduction was only a small part of the literature review, a lot of time was spent getting familiar with the theory and the state of the art of electret transduction. If a narrower focus was made earlier in the thesis project, a lot of time could have been saved, as much of the research performed for the literature review was not directly applied in the thesis.

A start was made by finding an accurate way to model the performance of electret transducers to see whether they would be promising alternatives for the electromagnetic transducer. The limitations of the conventional models for micro-electret transducers quickly became apparent. This led me to develop the novel model. This was a relatively straightforward process. Developing the unipolar electret concept, and then verifying it experimentally through a prototype was significantly more challenging. Going from concept to prototype took numerous changes to the design, experimental set-ups, and changes to the manufacturing process.

7.3. UNSUCCESSFUL ATTEMPTS

There were several unsuccessful attempts in fabricating the corona charging set-up. First, a corona charging set-up was made in which the steel ground plate could not be removed from the charging set-up. This made removing the charged sample very difficult, as the electrostatic forces attracted it to the ground plate. The ground plate was also not smooth enough to ensure that no air gaps were present between the sample and the ground plate during charging, which is why a silicon wafer was added between the charged sample and the steel ground plate. It was also found that one needle does not lead to an equal charge distribution on the sample, which is why an array of needles was used instead. Finally, to charge individual rotors, the set-up had to be altered again to ensure the ground on which the rotor was charged was shielded off to prevent a direct path to the ground for the corona discharge ions.

For the electret rotor, an attempt was first made to use a silicon oxide/silicon nitride double layer as an electret, as it showed promising results in published literature. There was no success in replicating the reported results, and the electret properties of the fabricated silicon oxide/silicon nitride double layer were disappointing. This caused a lot of delays, as the time it took to go from a concept to a fabricated wafer took months. After the initial failure, CYTOP was used instead. Luckily, the results using CYTOP were promising, and the unipolar electret concept using CYTOP was successful.

For the electrode rotor, a lot of trial and error was necessary to find the exact laser

parameters to pattern the copper layer. This was a time-consuming and headache-inducing process. A lot of samples were damaged in the process and thus not useful.

When making the 3D-printed base, multiple prototypes were necessary to reach a final design. First, a base was designed in which the electrode stator would be press-fitted. This was unsuccessful, as the electrode stator is too fragile to be press-fitted. Then, a small spring steel flexure was fabricated instead and form-fitted into the base. The steel flexure delivers a nesting force, wedging the stator in place against two pins.

When measuring the output power characteristics of the micro-electret transducer, a stepper motor was first used to induce the rotation of the electret rotor. This stepper motor created a lot of noise in the output voltage signal. Therefore, a rheometer was used instead, as it uses a motor that can induce a very smooth and precise rotation of the electret rotor. This removed the noise in the measured signal.

An oscilloscope was used to measure the output voltage. However, because the internal resistance of the oscilloscope was just $1M\Omega$, which is in the same order as the load resistance, accurate measurements were not possible. For this reason, a USB-6211 DAQ by National Instruments was used to record the output voltage, which has an internal resistance of more than $10G\Omega$. The DAQ allowed for successfully logging the voltage output of the micro-electret transducer.

7.4. CONCLUSIONS

The research objective as stated in the introduction is as follows.

Design, model, and experimentally verify *a microfabricated electret transducer that can be used to power a quartz watch.*

The research objective has been achieved, by answering the two research questions. The first research question is as follows.

How to accurately model and predict the output power characteristics of a micro-electret transducer?

- One-dimensional electrostatic models have been developed to predict the output power of electret transducers. However, for micro-electret transducers, fringing fields play a large role in the electrostatic domain. To be able to more accurately predict the output characteristics of micro-electret transducers, a novel electrostatic **model** has been proposed which accounts for fringing fields. The novel model is **verified experimentally** by comparing the novel model predictions with the output power characteristics of a fabricated micro-electret transducer for various angular velocities and load resistances. There is a close resemblance of the time signals, and the magnitude of the RMS output power is overestimated by a factor of two. This is a significant improvement compared with the conventional model, which overestimates the output power of the same micro-electret transducer by a factor of fifteen.

The output power of an electret transducer needs to be maximized to ensure that the transducer can generate enough energy to power a quartz watch. This led to the second research question.

How to maximize the output power of a micro-electret transducer?

- A **design** of a novel unipolar micro-electret transducer is proposed. The novel unipolar concept allows the micro-electret transducer to embed charges of only one polarity, increasing the output power of the micro-electret transducer. The unipolar electret concept is **verified experimentally** by measuring the chargeability and decay over time. Charge patterning with the unipolar electret has been successful and stable charge on electret segments down to a width of 100 μm has been achieved. An electret rotor is charged to 354 V on average, resulting in an average charge density of approximately $62 \mu C/m^2$. The average charge decay over a period of 28 days is found to be less than 5%, outperforming conventional electrets. A micro-electret transducer is fabricated according to the unipolar electret concept. The fabricated micro-electret transducer achieves a voltage amplitude of 10.8 V and an RMS output power of 17.7 μW at an angular velocity of 20π rad/s at matched load.

Finally, to see whether the unipolar micro-electret transducer can perform well inside a quartz watch, a dynamic model is made which uses the accelerations of a wearer as input. The dynamic model shows that a unipolar micro-electret transducer can generate an average of 514 mJ per day, which is approximately double the necessary energy to power a quartz watch. This shows that the unipolar micro-electret transducer is a viable transducer for powering quartz watches.

7.5. FUTURE RESEARCH RECOMMENDATIONS

When it comes to micro-electret transducers, there is much work to do before they have practical implementations. Several research topics are listed below, that have been identified throughout the thesis project.

7.5.1. NOVEL MODEL

- **Increase the applicability of the novel model:** The novel model is found to make significantly more accurate predictions of the output power characteristics of micro-transducers where the value of r is smaller than ten. When the value of r gets larger, the sine fit is not a good approximation of the charge distribution. To make the model more broadly applicable, several Fourier series terms can be taken into account with an amplitude dependent on the value of r. This would result in a charge distribution waveform that changes shape from a sine wave to a square wave as the value of r increases, making the model applicable for electret transducers of all values of r.

7.5.2. ELECTRET

- **Investigate the cause of the initial charge decay of the unipolar electret:** It was found that after charging unipolar electrets, a very rapid charge decay occurs, resulting in a stable surface voltage of about one-third of the grid voltage. The reason for this initial charge decay cannot be attributed to the electric field strength, as discussed in chapter 5. More work has to be done to understand what is the cause of this 'floating charge' and how to mitigate it.

- **Research of long-term charge stability:** Charge stability has been explored over a time period of about one month. This is not representative of the intended lifetime of the electret transducer, which should be several years. Longer-term testing of the charge stability, or accelerating the charge decay through thermally simulated discharge (TSD) can be performed to get a better insight into the long-term charge stability of the unipolar electret.

- **Explore alternative applications of unipolar electret application:** The unipolar electret concept has been applied for the purpose of micro-electret transducers, but a unipolar electret could be applied in other fields as well, such as sensing, air filters, and grippers utilizing the electrostatic force.

7.5.3. TRANSDUCER DESIGN

- **Parameter optimization:** Most of the effort in the design of the micro-electret transducer has gone into maximizing the induced charge, in order to achieve the highest possible output power of the transducer. One element which has not been covered extensively in this thesis is the optimization of the dimensional parameters of the electret transducer. A significant increase in output power is expected when the dimensional parameters of the electret-transducer design are optimized in combination with the mechanical design of the energy harvester.

- **Experimental set-up incorporating the mechanical design:** In chapter 6, the output power of the energy harvester consisting of the transducer in combination with the mechanical design is predicted through means of a numerical model. Only the transducer has been experimentally verified. In the numerical model, several simplifications are made, regarding frictional losses for example. The impact of these simplifications on the resulting output power has not been checked. An experimental set-up incorporating the mechanical design would allow for a better prediction of the output power of the energy harvester.

7.5.4. LARGE SCALE FABRICATION

- The findings of the dynamic model show that the energy harvester containing the micro-electret transducer has an output power high enough to power a quartz watch. But before the micro-electret transducer can be successfully applied to power quartz watches, low-cost large-scale fabrication needs to be possible. This is not the case with the manufacturing methods used in the prototype.

  - For the **electrode stator**, the problem with the prototype fabrication method is the need for expensive laser cutting equipment and the bad scalability due

to long laser cutting times, on the order of an hour per electrode. PCB fabrication methods can be used to fabricate interdigitated electrodes at high throughput at low cost. This would omit the time-intensive laser ablation step. This would also improve the performance by reducing the parasitic capacitance, as stated in section 6.1

- For the **electret rotor**, there are multiple problems with the prototype fabrication method.
  1. The expensive substrate material: The borofloat 33 ultra-thin glass wafers are expensive at 52.01$ per wafer [28].
  2. Time-consuming cleanroom fabrication: Coating and patterning of the CYTOP electret layer is time-consuming and expensive. Due to the transparent substrate, manual loading of the wafer is necessary, resulting in a lot of expensive manual labour. The need for multiple layers of spin coating CYTOP in combination with the long baking time also results in a long processing time.

  instead of spin coating CYTOP on ultra-thin glass wafers in a cleanroom, and then patterning using lithography and etching, polymer inkjet-printing can be used. This would allow for printing of CYTOP on glass sheets in mere seconds, instead of a fabrication time of multiple hours per wafer. An important dimensionless number for inkjet printing is the Ohnesorge number. In inkjet printing, liquids whose Ohnesorge number is less than 1 and greater than 0.1 are jettable.

$$Oh = \frac{\mu_d}{\sqrt{\rho \sigma D_d}} \tag{7.1}$$

Where Oh is the Ohnesorge number, μ_D is the dynamic viscosity of the liquid, ρ is the density of the liquid, σ is the surface tension and D_d is the droplet diameter. In Table 7.1, the properties of CYTOP solution are shown.

Table 7.1: CYTOP solution properties.

Parameter	Value	Description
μ_d	20-2000 [mPa s] [29]	Dynamic viscosity
ρ	2 $[kg/m^3]$ [29]	Density
σ	13.4 $[mN/m]$ [30]	Surface tension

When 20 $mPas$ is taken for the dynamic viscosity, and a droplet diameter D_d of 100 μm is chosen, the Ohnesorge number is 0.3835. This shows that inkjet printing is a promising alternative production method and should be explored further.

ACKNOWLEDGEMENTS

Firstly, I would like to thank my thesis supervisor from the TU Delft, Murali Ghatkesar. I value the regular meetings and his critical attitude, which pushed me to perform well. I would also like to thank my supervisors from Kinergizer, Gerard Dunning and Erik van de Wetering. Gerard Dunning has helped me with the feasibility of manufacturing the prototype. Erik van de Wetering was my go-to supervisor for questions regarding the measurement set-ups, LaTeX help, data acquisition, and basically any other question I could think of. I would also like to thank assistant professor Mohamad Ghaffarian Niasar and dr. Luis Castro Heredia for their help, lab space, and the equipment they let me use for the corona charging set-up. Without their help, fabricating the electret would have been impossible. I would like to thank Guido Janssen and Gideon Emmaneel for their help in the fabrication of the electrode stator. Guido Janssen was kind enough to sputter coat my samples with copper, and Gideon Emmaneel helped me a lot with laser cutting. I would like to thank Merlin Palmar and Aleksandar Jovic from Flexous for their knowledge and feedback regarding the manufacturing of the prototype, and their work in the cleanroom. Lastly, I would like to thank the Taylor board members, my parents, and my girlfriend, Cait O'Regan for their support which allowed me to continue the thesis project.

APPENDICES

A

THEORY AND MODELLING

In this chapter of the appendix, the background theory used to develop the novel model and the detailed design of the micro-electret transducer is discussed more extensively. First, the properties of electrets are discussed. Then, methods of charging electrets are covered. Finally, the theory governing the electrostatic domain is explained in detail.

A.1. PROPERTIES OF ELECTRETS

An electret is a dielectric material able to hold a quasi-permanent electrical charge. If there is a non-zero charge, or if charges are not compensated everywhere in the material, the electret produces an external electric field. This field can be used to induce a charge on a conductor. Many different types of electrets, electret materials, and charging methods exist. In this section, the properties of electrets are explained.

A.1.1. TYPES OF ELECTRETS

Electrets can be subdivided into several categories, based on the way they influence the electric field.

- **Real charges**: Real charge electrets are electrets that have an excess implanted real charge. These can be either positive or negative charge carriers. These implanted charges are trapped in so-called energy traps. A trap consists of either a chemical impurity or an imperfection in the regular spacing of the atoms that make up the solid. The depth of this trap is the height of the energy barrier that the charge carrier has to overcome to escape the trap. Real charges are typically trapped in surface or bulk levels located in the energy gap between the valence and conduction band. The implanted charges can occur at the surface of an electret, in the volume, or a combination of the two.
- **Polarization charges**:
  - **Molecular polarization charges**: When a dielectric is composed of polar molecules, they are randomly oriented in the absence of an electric field. If an electric field is applied, polar molecules will align with the field against the thermal drifts. To create permanent polarization, an electric field has to be applied whilst the temperature is increased to above the glass-transition temperature. This will cause the molecules to align with the electric field. If the temperature is then decreased again whilst still applying the electric field, the polarization is frozen and shows slow thermal decay [31]. In the early days, electrets were made of wax-based materials, such as carnauba wax, which were poor in thermal stability [32].
  - **Electronic polarization charges**: Non-polar materials can be polarized by the electric field produced by their own real charge distributions. This field-induced polarization is due to the orientation of atomic dipoles in the dielectric. This is the reason why the relative permittivity ϵ_r is always greater than 1, even in non-polar materials.

For all types of electrets, the general expression for the electric displacement is the following.

$$\hat{\mathbf{D}} \equiv \epsilon_0 \hat{\mathbf{E}} + \hat{\mathbf{P}} \tag{A.1}$$

Where $\hat{\mathbf{D}}$ is the electric displacement field, $\hat{\mathbf{E}}$ is the electric field, and $\hat{\mathbf{P}}$ is the polarization. $\hat{\mathbf{P}}$ is a result of the permanent field-independent polarization $\hat{\mathbf{P}}_{perm}$, and the induced polarization $\hat{\mathbf{P}}_{ind}$.

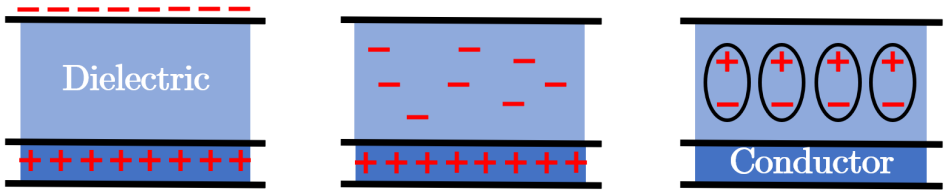

(a) Surface charge. (b) Volume charge. (c) Polarization charge.

Figure A.1: Schematic representation showing several different types of electrets.

$$\hat{\mathbf{P}} = \hat{\mathbf{P}}_{perm} + \hat{\mathbf{P}}_{ind} \tag{A.2}$$

The field in an electret $\hat{\mathbf{E}}$ can thus be found by knowing $\hat{\mathbf{P}}_{perm}$ and $\hat{\mathbf{P}}_{ind}$, and by applying Gauss' law for a dielectric.

$$\oint \hat{\mathbf{D}} dS = Q_{enc} \tag{A.3}$$

Where Q_{enc} is the sum of all the real enclosed charges. For electrets that only have real charges, all polarization charges are self-induced, and when assuming that the electret is a homogeneous, linear, non-dispersive, and isotropic dielectric medium, the self-induced polarization can be found using the following equation:

$$\hat{\mathbf{P}}_{ind} = \chi \epsilon_0 \hat{\mathbf{E}} \tag{A.4}$$

Where χ is the electric susceptibility, defined as $\chi = \epsilon_r - 1$. This means that for real charge electrets, the electric displacement can be easily found, as the permanent polarization charge is equal to zero: $\hat{\mathbf{P}}_{perm} = 0$.

$$\hat{\mathbf{D}} = \epsilon_0 \hat{\mathbf{E}} + \hat{\mathbf{P}}_{ind} = \epsilon_0 \hat{\mathbf{E}} + (\epsilon_r - 1)\epsilon_0 \hat{\mathbf{E}} = \epsilon_0 \epsilon_r \hat{\mathbf{E}} \tag{A.5}$$

Equation A.5 can be used to find an expression for the charge as a function of the electric field at the interface between two different materials. The difference between the electric displacement at the interface between the two materials is equal to the charge:

$$\hat{\mathbf{D}}_1 - \hat{\mathbf{D}}_2 = \epsilon_0 \epsilon_{r,1} \hat{\mathbf{E}}_1 - \epsilon_0 \epsilon_{r,2} \hat{\mathbf{E}}_2 = \sigma_{1,2} \hat{\mathbf{u}}_{n,1} \tag{A.6}$$

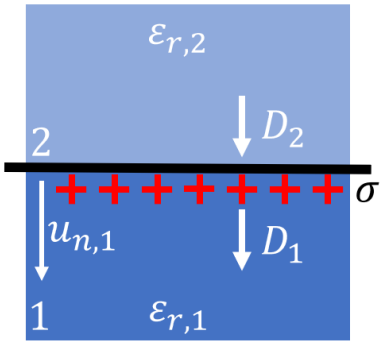

Figure A.2: Materials of different relative permittivity ϵ_r with a surface charge at the interface.

Equation A.6 is applied in section A.2 to derive the electric fields in the regions around real charge electrets with surface charge density.

A.1.2. ELECTRET MATERIALS

Many types of dielectric materials can be employed as electrets. Electret materials can be broadly divided into two categories; organic and inorganic electrets.

- **Organic electrets** consist of organic molecules, usually polymers. The charge storage capacity is determined by the chemical structures, composite ratio, and morphology of the charge trapping electrets [33]. A few examples are organic polymer electrets such as PTFE (Teflon), Cytop, and Parylene HT.
- **Inorganic electrets** are a more novel field of research. Two of the most promising inorganic electret materials are silicon oxide, and silicon nitride, or a multilayer combination of said materials. In inorganic electrets, the charge traps are associated with defects in the electret layer [34].

Electrets are typically thin films, ranging from 100 nm to 100 μm in thickness, depending on the material and the deposition method used. Organic electrets are usually spin-coated onto a conductive substrate. Inorganic electrets such as silicon oxide and silicon nitride are deposited using chemical vapor deposition (CVD). Some popular dielectric materials with relevant properties are shown in Table A.1. In the following sections, the properties will be explained in more detail.

Because the energy harvester will be fabricated using MEMS-compatible cleanroom processes, inorganic electret materials are seen as favorable. Namely the SiO_x/SiN_x double layer electret. The properties of such inorganic electrets will be explained further.

A.1.3. CHARGE DENSITY

The charge density is an expression of the amount of charge that can be stored in an electret. When talking about surface charges, the unit is C/m^2. When talking about volume charges, the unit is defined as C/m^3. The maximum charge density that can be achieved is constrained by several limits.

Table A.1: Parameters of several electret materials [32].

Material	**Dielectric Constant**	**Dielectric Strength** ($V/\mu m$)	**Max. Operating Temperature** (C)	**Surface Charge Density** (mC/m^2)
PTFE	2.1	11.22	260	0.1
SiO_x/SiN_x	3.9/7.5	500	1700	13.5
Cytop	2.1	110	350	1.5
Parylene-HT	2.17	204.58	500	3.69

- **Dielectric breakdown**: The dielectric strength of the electret poses an upper limit on the charge density. When the electric field that results from the charge exceeds the dielectric strength of the material, the electrical current breaks through the material and the charge escapes the electret.
- **External breakdown**: Electrets are used in freestanding energy harvesters to induce a charge on an electrode. This is done by generating an electric field in the space between the electret and the opposing electrode. When this electric field becomes too large, the air will break down and the electret will discharge. Paschen's law describes this phenomenon, and the breakdown voltage as a function of the gap distance can be seen in Figure A.3. The equation for the breakdown voltage can be seen below.

$$V_{max} = \frac{\alpha pg}{ln(pg) + \beta} \tag{A.7}$$

Where V_{max} is the breakdown voltage, α, and β are two constants depending on the composition of the gas, p is the atmospheric pressure, g is the gap size. For ambient atmospheric conditions (ambient air O_2(20%), N_2(80%)), the pressure p is equal to 1 atmosphere, α is equal to $43.6E6V/(atm \cdot m)$, and $\beta = 12.8$ [35, 36].

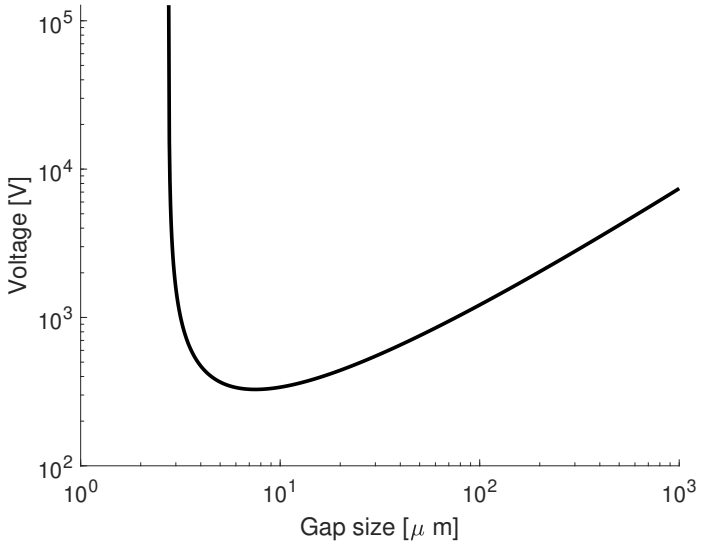

Figure A.3: External breakdown voltage as a function of the gap size, according to Paschen's law in air at atmospheric pressure.

A.1.4. CHARGE STABILITY

An important metric for the performance of an electret is charge stability. The time scale of the discharge of the electret needs to be larger than that of the lifetime of the device to function properly. When this is not the case, the performance of the device degrades during use. Charge stability of electrets is a large focus and many papers have been published reporting on the discharge mechanisms, and the methods to improve charge stability.

To understand charge stability, one must first look at the ways for an electret to discharge. At room temperature, the thermal energy alone is not enough for charge carriers to escape their charge traps. However, all electrets still slowly discharge, with half-lives ranging from several days to hundreds of years [37]. This discharge at room temperature is mainly due to two processes.

- **Humidity**: Water vapor in the air is attracted to the electret surface. This is due to two reasons. Water is attracted to hydrophilic silicon oxide bonds at the surface of the electret and due to the electric field that attracts water due to its bipolarity. This water is then absorbed by the electret surface and increases the surface conductivity. This increased surface conductivity decreases the energy trap depth which causes the charge carriers to move into the conduction band and dissipate [34, 38].

- **Air ions**: Ions in the air with an opposite charge of the electret surface are attracted due to the generated electric field. The ions with opposite charges in turn mask the charge and thus neutralize the electric field.

A.2. ELECTRET CHARGING

A.2.1. CHARGING METHODS

There are multiple methods that can be used to charge an electret. The methods covered in this section are methods that are compatible with MEMS fabricated micro-electrets, in a highly controlled environment.

- **Corona charging**: The most well-established and reported method to fabricate electrets is through corona charging. This method uses a needle at a high voltage (on the scale of multiple kVs) to create a corona discharge. Corona discharge is the creation of plasma due to the high electric field in the vicinity of the needle. The plasma zone of the corona extends only a few millimeters in the direction of the electric field. Outside this region, uni-polar ions produced in the plasma are transported by the electric field [39].

  If the electret is positioned between the ground and the needle, the uni-polar ions generated by corona discharge are accelerated to the surface of the electret due to the electric field. These ions then come into contact with the surface, and the charge is embedded in the surface of the material.

  The corona charging method has merits including a simple set-up and a short time for reaching the desired surface potential.

- **Electron beam**: One method to manufacture an electret is through the injection of a monoenergetic particle beam (e.g., electron beam) that has a smaller wavelength than the thickness of electret films. This method has been shown to produce reliable electrets. The high resolution that can be achieved makes electron-beam charging a more reliable and also more convenient method of obtaining electrets with better control over charge density, lateral charge position, and most importantly its control over the depth of the charge in the electret. The latter is related to the range of the electrons in a material which, in turn, depends on the beam energy. The depth of the charge is an important factor with respect to charge lifetime [40, 41].

- **Soft X-ray charging**: A novel charging method has been proposed to improve the compatibility of electret-based devices with available MEMS techniques. Soft X-ray radiation of high energy (up to tens of keV) can be used to charge electrets inside MEMS devices after fabrication. Soft x-rays can penetrate the assembled device and ionize the air inside the device. These ions are then attracted to the surface of the electret by applying a bias voltage across the electret [42, 43]. The method with which the charges are trapped inside the electret is similar to corona charging.

All the methods mentioned above are suitable methods to embed the charge in the electret for the application of electret-based energy harvesters. For the reasons of simplicity and the availability of the equipment, corona charging is chosen as the most favorable method.

A.2.2. PHYSICS OF CORONA CHARGING

In this section, the theory that dictates the properties of electrets when manufactured using corona charging will be explained in depth. As mentioned in subsection A.2.1, corona charging is performed by applying a large voltage to a needle leading to corona discharge. When the electret is then put on a grounded substrate, the ions generated by the corona discharge are accelerated towards the electret surface by the electric field. To generate corona discharge, a large voltage has to be applied (on the scale of several to tens of kVs). If the charging would be left to go uninterrupted, the charge density and the charge uniformity will be difficult to control.

To improve the charge distribution uniformity and to have better control of the magnitude of the charge density, a grid is inserted between the discharge needle and the sample. A potential V_g is applied to the grid, which is lower than the corona discharge needle potential V_c. A schematic of the charging set-up is shown in Figure A.4.

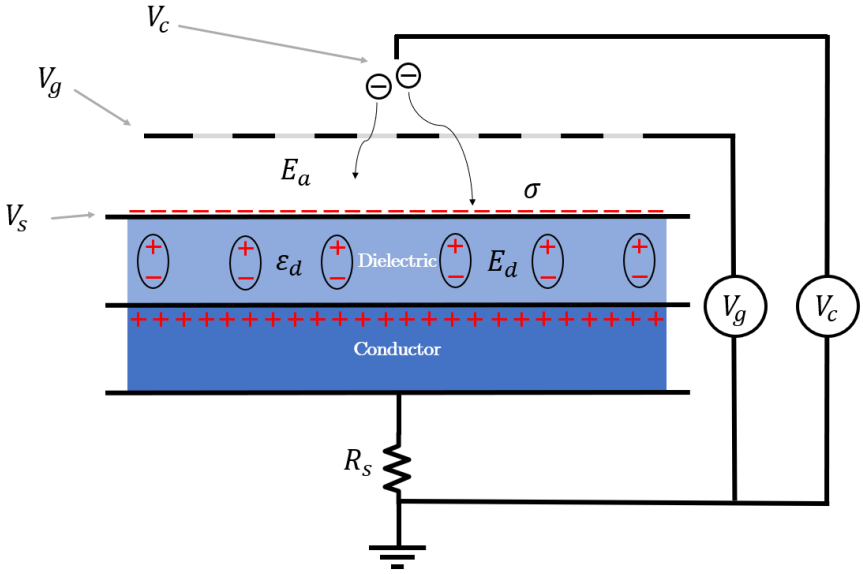

Figure A.4: Corona charging.

The role of the grid is to regulate the charge density on the surface of the electret. During charging, ions are accelerated from the needle through the grid towards the surface of the electret. But as the surface of the electret charges, the surface voltage V_s increases. When the surface voltage of the electret approaches the grid voltage, the electric field E_a between the grid and the electret approaches 0, and ions stop being accelerated towards the surface. This ensures that the surface voltage of the electret is equal to the grid voltage after significant charging time.

$$V_s = V_g \tag{A.8}$$

The relation between the surface voltage V_s of the electret after charging and the surface charge density of the electret σ can be easily found by applying Equation A.6.

$$\epsilon_0 \epsilon_d E_d - \epsilon_0 E_a = \sigma \tag{A.9}$$

Where ϵ_d is the relative permittivity of the dielectric and E_d is the electric field inside the dielectric. As E_a is zero and E_d is equal to $\frac{V_s}{d}$, Equation A.30 reduces to the following equation:

$$\epsilon_0 \epsilon_d E_d = \frac{\epsilon_0 \epsilon_r V_s}{d} = \sigma \Longrightarrow \sigma = \frac{\epsilon_0 \epsilon_d V_s}{d} \approx \frac{\epsilon_0 \epsilon_r V_g}{d} \tag{A.10}$$

Rearranging this gives an expression for the surface charge density, as a function of the relative permittivity of the dielectric ϵ_d, the grid voltage V_g, and the electret thickness d.

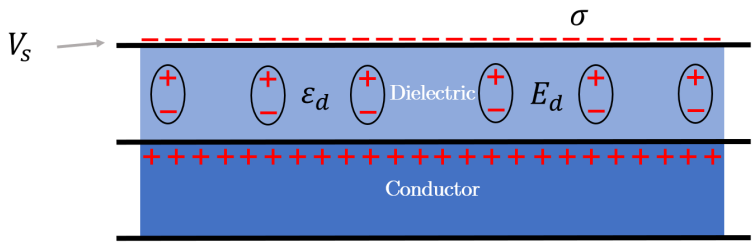

Figure A.5: After Corona charging.

A.2.3. MEASUREMENT OF IMPLANTED CHARGES

The surface potential measurement is done using an electrostatic voltmeter (ESVM). An ESVM is used as it allows for measuring the surface potential without being in physical contact with the electret. This non-invasive measurement method allows for surface potential measurements without discharging the electret. Electric potential and/or charge is detected by the voltmeter by the means of non-contact capacitive coupling between the voltmeter electrode and the electret surface. A vast majority of ESVMs use a vibrating grounded conductor that periodically shields the probe electrode from the electric field generated by the electret. This causes the induced charges on the probe electrode to be modulated, and an AC voltage signal is created in the probe. This technique is used since it allows for fast and accurate measurements. A DC voltage V_m is applied to the probe electrode, which is increased until the probe electrode is at the same potential as the electret surface. When this happens, the electric field in air E_a drops to zero, and no more charge is induced on the probe electrode, so no AC voltage is observed. According to Kirchhoff's voltage law, the ESVM measurement voltage V_m is then equal to the surface voltage of the electret V_s. In Figure A.6, a schematic of the ESVM measurement set-up is shown.

If the distance between the probe electrode and the electret surface z increases, fringing fields start to play more and more of a role in measuring the surface charge of small features, such as narrow patterns of charge. A general rule for accurate measurement is

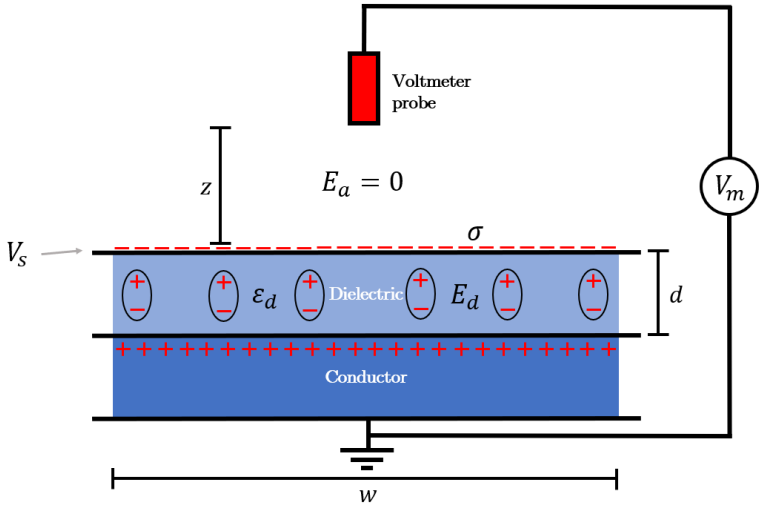

Figure A.6: Electrostatic voltmeter.

that the distance z much be significantly smaller than the size w of the feature that you try to measure, in order to get an accurate reading.

$$if\ w \gg z, V_s \approx V_m \tag{A.11}$$

A.3. ELECTRODE CAPACITANCE CALCULATION

The electrode capacitance is an important parameter for the performance of an electret transducer. It is important to be able to make an accurate estimation of the electrode capacitance in the early design phase. To be able to do this, the conformal mapping method as described by Igreja et al. is adapted to fit rotational interdigitated electrodes [44].

An important parameter, for the electrode capacitance, the 'metalization factor' η, is the ratio of the surface which is covered by electrodes and can be calculated as follows.

$$\eta = \frac{w}{w+g} \tag{A.12}$$

Where w is the width of an electrode strip and g is the gap between the electrodes. Because the width of an electrode strip w is not constant for rotational electret transducers, as is also shown in chapter 4, this equation has to be adapted.

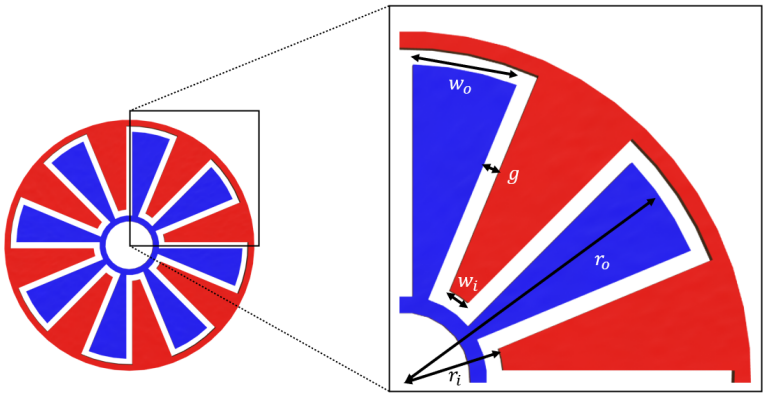

Figure A.7: Parameters used to calculate the capacitance for a rotational interdigitated electrode.

First, the inner and outer width w_i and w_i of the individual electrode segments can be calculated respectively using the number of electrode pairs n, the gap size g, and the inner and outer radius r_i and r_o. The parameters necessary in the calculation can be seen in Figure A.7.

$$w_i = \frac{2\pi r_i}{2n} - g \quad w_o = \frac{2\pi r_o}{2n} - g \tag{A.13}$$

Using the inner electrode width and the outer electrode width, the metalization can be calculated by integrating the expression for η along the width of the electrode segment.

$$\eta = \frac{1}{w_o - w_i}\int_{w_i}^{w_o} \eta dw = 1 + \frac{g}{w_o - w_i} log(\frac{g+w_i}{g+w_o}) \tag{A.14}$$

Then, the modulus of the elliptical integral can be calculated for the internal and external capacitance contribution.

$$k = sin(\frac{\pi\eta}{2}) \tag{A.15}$$

Using the elliptical integral, C_I, half the capacitance of one interior electrode relative to the ground potential can be calculated.

$$C_I = \epsilon_0(\epsilon_d + 1)L\frac{K(k)}{K(k')} \tag{A.16}$$

Where $K(k)$ is the complete elliptic integral of the first kind with modulus k, k' the complementary modulus, $k' = \sqrt{(1-k^2)}$ and L is the length of the interdigitated electrodes, which is equal to the outer radius minus the inner radius: $L = r_o - r_i$. Using network analysis to evaluate the equivalent circuit, one finds the total capacitance between the two electrodes is found to be equal to the following expression.

$$C = nC_I \tag{A.17}$$

Where n is the number of electrode pairs.

A.4. INDUCED CHARGE

A.4.1. CONVENTIONAL ELECTRETS

In most research describing electret transducers, the focus is on increasing the surface charge density of the electret. However, in the context of electret transducers, this focus on surface charge density is misleading. For electret transducers, the charge induced by the electret, not the surface charge of the electret, is to be maximized. For conventional electrets that use a conductive substrate, most of the charge is induced on the silicon base electrode, instead of on the counter electrodes. This induced charge is 'idle' and does not aid power generation. The charge induced by a conventional electret on a conductive substrate is graphically represented in Figure A.8.

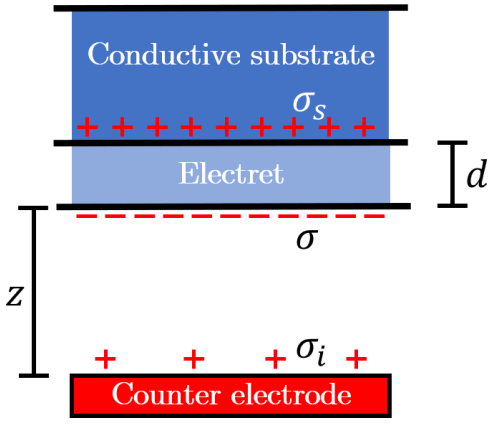

Figure A.8: Conventional electret.

Where z is the distance between the electret surface and the counter electrode, d is the electret thickness, σ is the electret surface charge density, σ_i is the counter electrode surface charge density and σ_s is the substrate charge density.

An analytical expression for the induced charge can be made by assuming that the electric field outside of this system is zero, $\hat{\mathbf{E}} = 0$. This means that the substrate and the counter electrode are at ground potential. If this hypothesis is not met, analytical modeling is not possible as the induced charges will be ill-defined. To ensure that the substrate and the counter electrode are at ground potential, they can be grounded together, ensuring that the analytical expression is accurate.

When looking at a 1-Dimensional situation, the contribution of each charge density to the field in air is equal to the following expression.

$$E_{\sigma_x} = \frac{\sigma_x}{2\epsilon_0} \tag{A.18}$$

Using this expression, the net field outside the system can be calculated

$$E_o = \frac{\sigma + \sigma_s + \sigma_i}{2\epsilon_0} \tag{A.19}$$

As the electric field is zero outside the system, the sum of all charge densities is equal to zero.

$$\sigma + \sigma_s + \sigma_i = 0 \tag{A.20}$$

Equation A.18 can now be used to calculate the electric field inside the electret, E_d, and the electric field inside the air E_a

$$E_d = \frac{\sigma_s - \sigma - \sigma_i}{2\epsilon_0\epsilon_d} \tag{A.21}$$

$$E_a = \frac{\sigma_i - \sigma - \sigma_s}{2\epsilon_0} \tag{A.22}$$

By filling in Equation A.27 into Equation A.21 and Equation A.29 and rearranging, the following expressions can be found for the electric fields.

$$E_d = \frac{\sigma_s}{\epsilon_0\epsilon_d} = \frac{-\sigma - \sigma_i}{\epsilon_0\epsilon_d} \tag{A.23}$$

$$E_a = \frac{\sigma_i}{\epsilon_0} \tag{A.24}$$

Because the substrate and the counter electrode are grounded, their potentials are equal. From this, an expression can be made for the induced charge.

$$V_i = V_d \Longrightarrow E_a \cdot z = E_d \cdot d \Longrightarrow \sigma_i = -\frac{\sigma d}{d + \epsilon_d z} \tag{A.25}$$

For the analyzed electret energy harvesters, the induced charge is a factor 14-21 smaller than the surface charge of the electret [45–47].

A.4.2. UNIPOLAR ELECTRET CONCEPT

To improve the performance of conventional electret transducers, Boland et al. suggested increasing the thickness of the electret for an increased performance [48]. Increasing the thickness is not a good idea, as it leads to larger stresses, risk of cracking, bad charge stability when charging up to the breakdown limit [49, 50], and does not solve the issues with discharge in air due to tolerances, manufacturing defects, and deflections.

A better method to increase the maximum surface charge is by removing the conductive back plate from the electret. By removing the conductive backplate, σ_s will be equal to 0 and all the charge will be induced on the counter electrode. In such a situation, $\sigma_i = -\sigma$. An added benefit of this is that the electric field inside the air will be constant, irrespective of gap size.

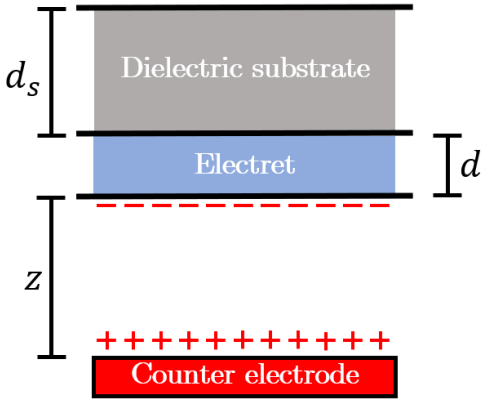

Figure A.9: Novel electret schematic.

For the unipolar electret concept, the induced charge σ_i can be calculated as a function of the electret surface charge σ using Equation A.18 as is done for the conventional method. The difference this time is that there is no substrate charge σ_s. s

Using Equation A.18, the net field outside the system is equal to

$$E_o = \frac{\sigma + \sigma_i}{2\epsilon_0} \tag{A.26}$$

As the electric field is zero outside the system, the sum of all charge densities is equal to zero.

$$\sigma + \sigma_i = 0 \tag{A.27}$$

Rearranging, shows that the induced charge is equal and opposite from the electret surface charge:

$$\sigma_i = -\sigma \tag{A.28}$$

Equation A.18 can now be used to calculate the electric field inside air E_a

$$E_a = \frac{\sigma_i - \sigma}{2\epsilon_0} = \frac{\sigma_i}{\epsilon_0} \tag{A.29}$$

During corona charging, the surface charge can be calculated according to the same method as in subsection A.2.2, but now we have to account for the effect of the dielectric substrate.

The relation between the surface voltage V_s of the electret after charging and the surface charge density of the electret σ can be easily found by applying Equation A.6.

$$\epsilon_0 \epsilon_d E_d - \epsilon_0 E_a = \sigma \tag{A.30}$$

Where ϵ_d is the relative permittivity of the electret and E_d is the electric field inside the electret. As E_a is zero, Equation A.30 reduces to the following equation:

$$\sigma = \epsilon_0 \epsilon_d E_d \tag{A.31}$$

Where V_{ss} is the substrate voltage, the only unknown in the equation. An expression can be found for V_{ss} when looking at electric displacement at the interface between the electret and substrate. The difference between the electric displacement at the interface between the two materials is equal to the charge, which for the interface between the dielectric substrate and the electret substrate gives the following expression:

$$\epsilon_0 \epsilon_d E_d - \epsilon_0 \epsilon_s E_{ss} = \sigma_{ss} \Longrightarrow \epsilon_0 \epsilon_d E_d = \epsilon_0 \epsilon_s E_{ss} \Longrightarrow \sigma = \epsilon_0 \epsilon_d \frac{V_{ss}}{d_s} \tag{A.32}$$

As there is no charge σ_{ss} at the interface between the electret and the substrate, the electric displacement fields are equal in both layers. Where ϵ_s is the substrate relative permittivity and E_{ss} is the electric field inside the substrate. Replacing the expressions for the electric field with the potential difference divided by the layer thickness, the following equation is found.

$$\epsilon_0 \epsilon_d \frac{V_g - V_{ss}}{d} = \epsilon_0 \epsilon_s \frac{V_{ss}}{d_s} \tag{A.33}$$

Rearranging gives the following expression for the substrate voltage V_{ss}

$$V_{ss} = \frac{\epsilon_0 \epsilon_d V_g}{d(\frac{\epsilon_0 \epsilon_d}{d_s} + \frac{\epsilon_0 \epsilon_s}{d})} \tag{A.34}$$

Plugging this result into Equation A.32, yields the following expression for the electret surface charge σ, as a function of the electret and substrate thickness and properties.

$$\sigma = \frac{V_g \epsilon_0 \epsilon_d \epsilon_s}{d\epsilon_s + d_s \epsilon_d} \tag{A.35}$$

B

DETAILED DESIGN AND FABRICATION

In this chapter, several design and fabrication details will be covered which have not been discussed in the main body but are still useful to people interested in designing and fabricating electret-transducers.

B.1. ELECTRET MATERIAL

Initially, a silicon oxide/silicon nitride (SiO_x/SiN_x) double layer was chosen as electret material. This decision was made due to the high charge stability, MEMS-compatible manufacturing, and straightforward fabrication. However, the chargeability and the charge stability of the fabricated SiO_x/SiN_x electret layers were found to be insufficient. The reason for the bad performance can most likely be attributed to the material properties of the deposited layers, which are highly dependent on the deposition parameters. The electret properties of the layers are largely dependent on the material properties.

After recognizing the shortcomings of the fabricated SiO_x/SiN_x electret, CYTOP (CTL-M), hereafter abbreviated to CYTOP, is chosen as the electret material due to the reliable electret properties of CYTOP, including high charge stability. CYTOP is a fluoropolymer and can be spin-coated on top of the substrate. In CYTOP, the charge trapping capability is strongly related to the end group [51]. Multiple types of CYTOP exist, with the difference being the end group. Kim et al. have shown that CYTOP has superior charge stability and chargeability, owing to the deeper charge traps [52]. For this reason, CYTOP is selected. The molecular structure of CYTOP can be seen in Figure B.1.

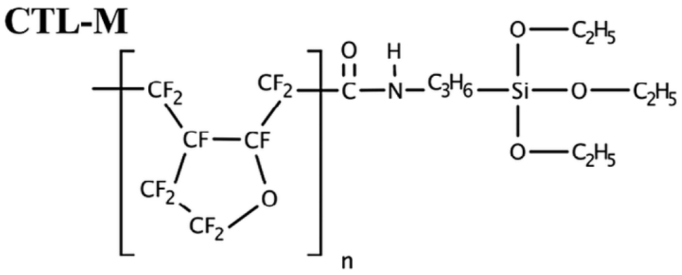

Figure B.1: Molecular structure of CYTOP (CTL-M). (Courtesy of Kim et. al [52])

The rotor consists of a glass substrate wafer of a thickness of only 100 μm with 4μm thick CYTOP segments oriented radially. The rotor is charged using a corona charging set-up. During charging, charge will be deposited on the glass substrate as well as the CYTOP segments, but because the glass substrate has a very low trap density and a relatively high conductivity, the charge will dissipate quickly. This leaves only the embedded charge on the CYTOP segments.

This is shown in graphically in Figure B.2. Right after charging, the surface voltage V_S is equal, and because of this, the CYTOP and the glass have surface charge σ and σ_{ss} respectively, which can be calculated according to Equation A.35 and Equation A.10 respectively. Because the capacitance of the substrate layer is thinner than that of the CYTOP-substrate double layer, σ_{ss} has a sligthly higher charge density, this unstable charge dissipates quickly however.

B.2. ELECTRET CHARGING

A render of the charging set-up of the wafer is shown in Figure B.3. The wafer is clamped onto a ground plate by a sleeve that also holds the grid. This ensures a good connection

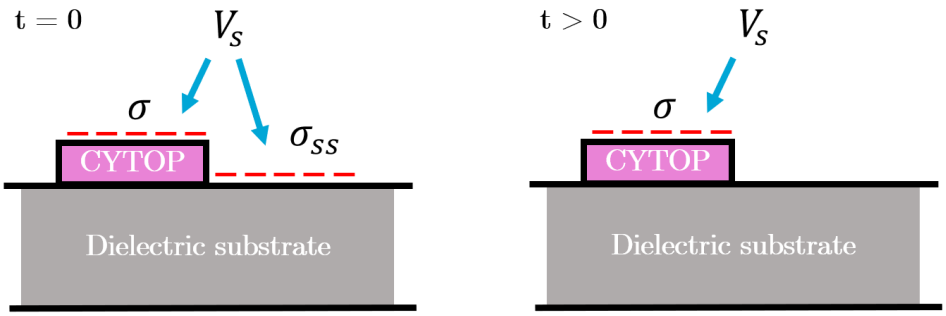

(a) Directly after charging.

(b) When all the floating charge has dissipated.

Figure B.2: Surface charge of the CYTOP electret segments on top of a dielectric substrate.

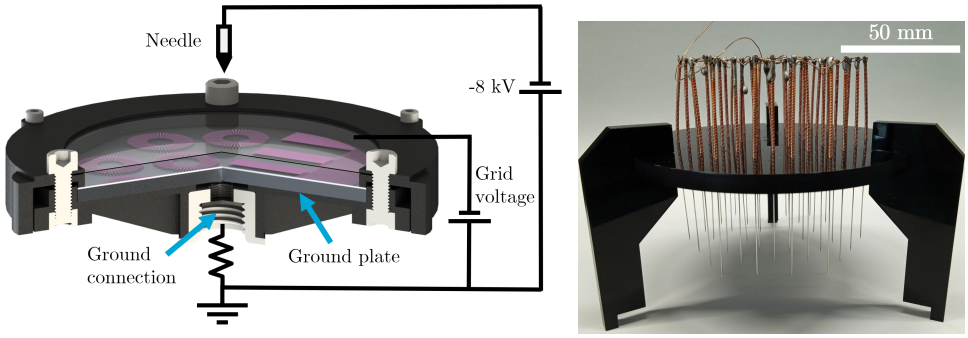

a. b.

Figure B.3: **(a)** Schematic of the charging set-up showing the main components. **(b)** photo of the needle array.

between the wafer and the ground plate. The ground plate is connected to the ground through a spring that comes into contact with threaded ground connection. d

To ensure a constant distribution of charge across the whole surface of the wafer, it was found that one needle was not sufficient, as this leads to a concentration of charges on the surface of the wafer directly below the needle. Instead, an array of needles is used, spaced 15 mm apart in a hexagonal pattern, as is shown in Figure B.3. The needles are connected to each other by soldering them to a copper wire. This ensures that the resistance between the voltage source and each needle tip is approximately equal. Therefore, when applying a high potential, the corona discharge current is equal at all needles. This is necessary to achieve an equal surface voltage across the sample. Two HCN 35 - 12500 FuG Elektronik power supplies are used that apply a voltage to the grid and the needle.

B.3. COPPER SPUTTERING OF THE ELECTRODE

For the electrode, D 263 M borosilicate glass is used as a substrate. Copper is sputter coated on top of the glass substrate using an AJA sputter coater. An average thickness of

312 nm was achieved, with a standard deviation of 38 nm over 10 samples.

B.4. LASER CUTTING

The laser cutting settings used in laser ablation and laser cutting be found in Table B.1. The laser power must be low enough to ensure that the sample does not heat past 350 °C. At this temperature, thermal decomposition of CYTOP occurs and this may generate hazardous substances such as hydrofluoric acid [29].

Table B.1: Lasea laser settings.

Substrate	Lens	Speed [mm/s]	Jump Speed [mm/s]	Burst rate [Hz]	Burst time [fs]	Repetitions [-]	Pulse rate [Hz]	Laser power [%] (of 3 W)
Copper electrode patterning	F-theta 515	100	100	25000	10	20	75018	1
Borofloat 33 dicing	F-theta 515	200	200	25000	10	1000	75018	40
D 263 M dicing	F-theta 515	200	200	25000	10	1600	15003	80

C

Measurements and results

In this chapter, measurements and results that have not been covered in the previous chapters will be shown and elaborated upon.

C.1. MEASUREMENTS

C.1.1. ELECTRODE MEASUREMENTS

To verify that the electrode works as intended, the resistance and the capacitance are measured using the Voltcraft LCR-300 LCR meter. First, the electrode is cleaned using a cotton swab with isopropanol.

- To verify that there are no shorts between the two electrode pairs, the resistance is measured. A resistance that is lower than tens of $M\Omega$ suggests that there are shorts between the two electrode pairs.
- To verify that the wires make electrical contact with the contact pads and that there are no breaks in the electrode, the capacitance is measured. A capacitance that is in line with the measurements ($\approx 57.7pF$), means that the soldered connections make contact and that the interdigitated electrodes function are successfully fabricated. The measured capacitance is equal to $64.2 \pm 0.4pF$. The capacitance calculation underestimates the capacitance by only 11.1%. This can be attributed to the excess capacitance of the soldered connections.

C.1.2. POWER OUTPUT MEASUREMENT SET-UP

In Figure C.1, the measurement set-up which is used to record the power output characteristics of the micro-electret transducer is shown.

- One wire is soldered to the contact pads of each electrode. These wires are connected to a TENMA 72-7270 decade box. This allows for quick adjustment of the load resistance ranging from 1 to 10 $M\Omega$.
- The NI-USB 6211 DAQ is used as its high input resistance ($> 10G\Omega$) means that the influence of the input resistance on the measured signal is minimal. The input capacitance is on the same order of magnitude as the capacitance of the electrode. The total capacitance of the DAQ and the decade box is measured to be 49 pF, and independent of the resistance of the decade box. This capacitance has to be taken into account and corrected for in the measurements.
- The rotation of the electret rotor is induced using the HR10 rheometer by TA instruments. A flexible coupling comprising a spring is used to allow for slight misalignment between the suspension of the electret and the axis of rotation of the rheometer.

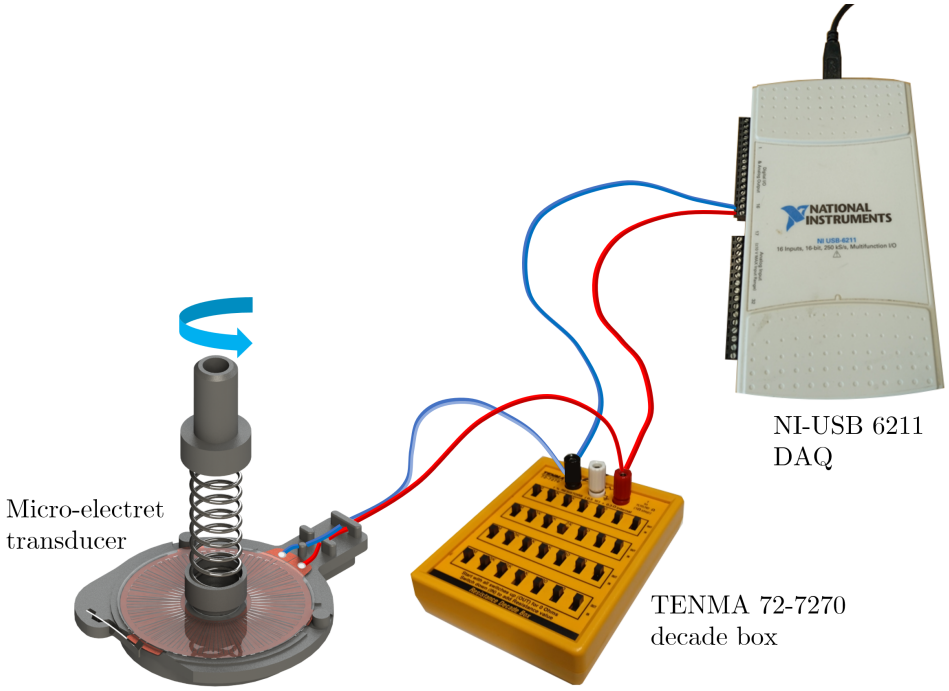

Figure C.1: Schematic of the measurement set-up used to record the power output characteristics of the micro-electret transducer.

C.2. RESULTS

As mentioned in section B.1, an effort was first made to verify the unipolar electret concept using a SiO_x/SiN_x double-layer electret. A borofloat 33 glass wafer was fabricated with patterned SiO_x/SiN_x double-layer electret segments using the same electret pattern layout as can be seen in chapter 5. In Figure C.2, the surface voltage after charging the set of logarithmic SiO_x/SiN_x double-layer electret segments is shown. The wafer is charged for 30 minutes with a needle voltage of -8 kV and a grid voltage of -300 V. It is not possible to distinguish between the electret segments and the glass wafer, showing that the SiO_x/SiN_x double layer electret cannot trap charges. After just two days, the surface voltage was reduced to 0 V across the entire wafer.

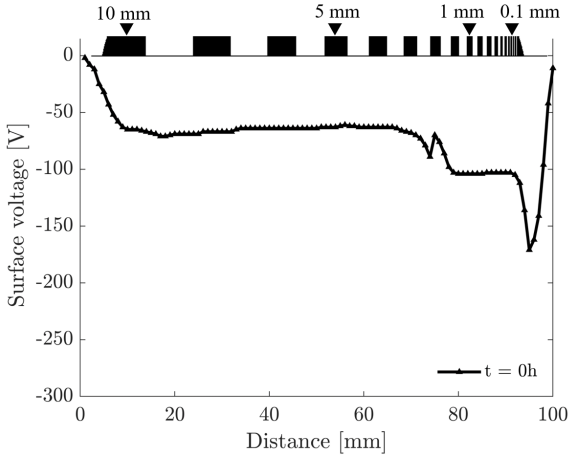

Figure C.2: Surface voltage directly after charging of the set of logarithmic SiO_x/SiN_x double layer electret segments after charging.

In order to find the right etching parameters to successfully fabricate patterned CYTOP electret segments, a conventional CYTOP on silicon patterned wafer was fabricated first. This silicon wafer also doubles as a baseline measurement to verify whether charging is successful. In Figure C.3, the surface voltage at several moments in time of the set of logarithmic CYTOP electret segments on top of a silicon wafer is shown. The wafer is charged for 30 minutes with a needle voltage of -8 kV and a grid voltage of -300 V. As predicted, the chargeability of narrow electret segments is poor due to the direct path of ions to the silicon ground during charging. The chargeability decreases proportionally with the electret segment width.

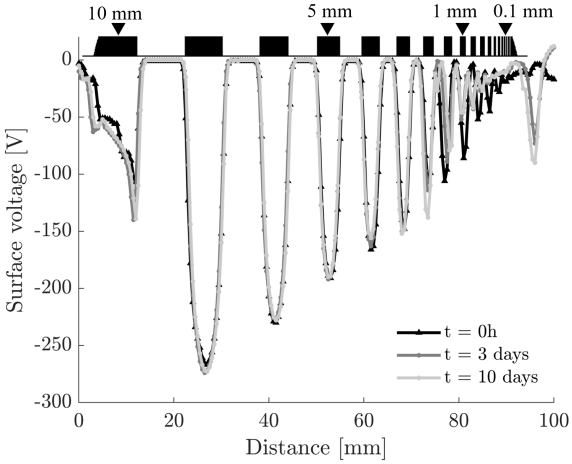

Figure C.3: Surface voltage at several moments in time of the set of logarithmic electret segments on silicon after charging.

What can also be seen is that the chargeability of the wider electret segments is very high, with a stable surface voltage which is almost as high as the grid voltage. In Figure C.4, the chargeability is compared between the electret segments of a width of 7.74 mm for the conventional CYTOP on silicon electret and the novel unipolar electret. As stated in chapter 5, the chargeability of the unipolar electret is relatively poor, with the stable surface voltage being about one-third of the conventional electret.

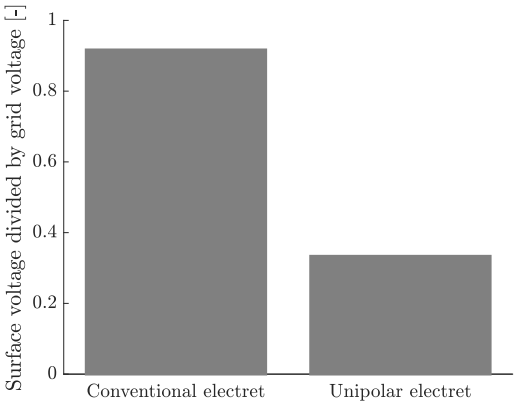

Figure C.4: The stable surface voltage divided by the grid voltage of an electret segment with a width of 7.74 mm for the conventional electret and the unipolar electret.

In Figure C.6, the surface voltage of charging an individual rotor on top of the original charging ground plate can be seen. The rotor is charged for 30 minutes with a needle voltage of -8 kV and a grid voltage of -1.5 kV. The schematic layout of the original charging ground plate can be seen in Figure C.6. The charging is unsuccessful due to the direct path to the ground for the corona discharge ions. The direct path to the ground prevents them from embedding inside the CYTOP electret segments on the rotor. Therefore, the charging ground plate is adapted. The adapted charging ground plate comprises an aluminium ground plate on which the rotor is placed. The part of the ground plate which is not covered by the electret rotor is shielded using PMMA inserts, preventing a direct path to the ground during charging. The successful charging result of an individual rotor is shown in chapter 5. A photo of the fabricated ground plate including the PMMA inserts is shown in Figure C.7

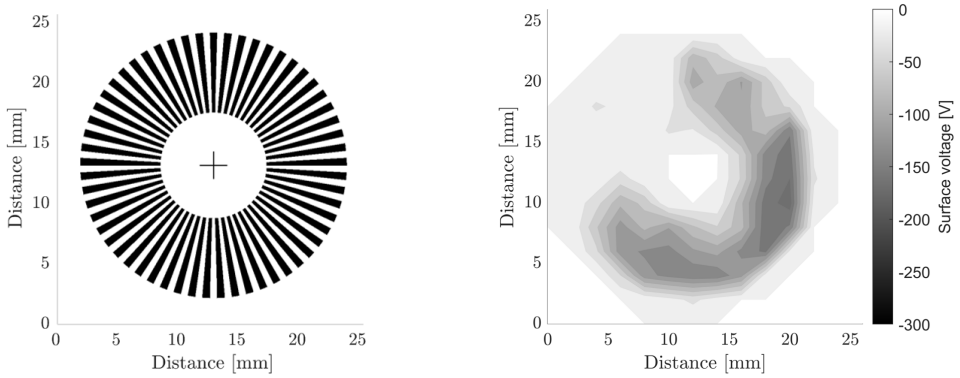

(a) (b)

Figure C.5: **(a)** Rotor CYTOP segments shown in black for reference. **(b)** Measured surface voltage across the rotor when charged using the original charging ground plate.

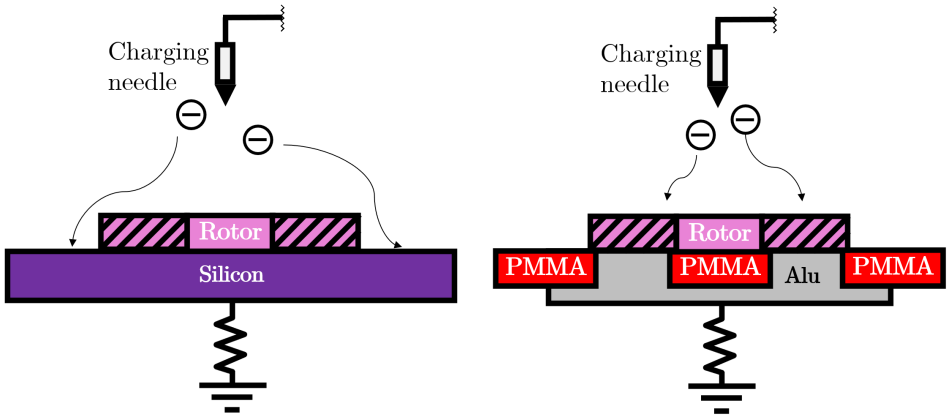

(a) (b)

Figure C.6: **(a)** Original charging ground plate used to charge an entire wafer showing that when charging rotors in this way, there is a direct path for the ions to the ground. **(b)** Adapted charging ground plate to effectively charge individual rotors with a shielded ground.

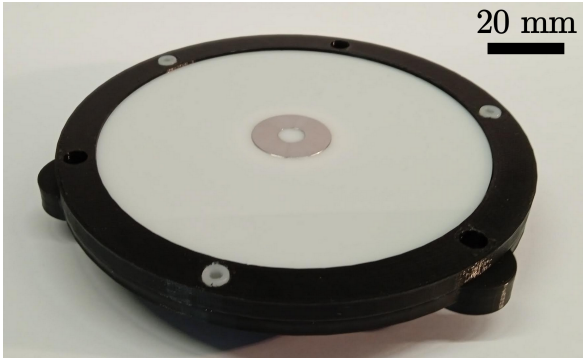

Figure C.7: Photo of the adapted ground plate comprising an aluminium ring with PMMA inserts (white).

BIBLIOGRAPHY

[1] Tiago Fernández-Caramés and Paula Fraga-Lamas. "Towards The Internet of Smart Clothing: A Review on IoT Wearables and Garments for Creating Intelligent Connected E-Textiles". In: 7 (Dec. 2018), p. 405. DOI: 10.3390/electronics7120405.

[2] Anwesa Mohanty et al. "Vibration Energy Harvesting; A Review". In: *Journal of Advanced Dielectrics* 9 (Aug. 2019). DOI: 10.1142/S2010135X19300019.

[3] Paul D. Mitcheson et al. "Energy Harvesting From Human and Machine Motion for Wireless Electronic Devices". In: *Proceedings of the IEEE* 96 (2008), pp. 1457–1486.

[4] Andreas Haeberlin et al. "Successful pacing using a batteryless sunlight-powered pacemaker". In: *EP Europace* 16.10 (June 2014), pp. 1534–1539. ISSN: 1099-5129. DOI: 10.1093/europace/euu127. eprint: https://academic.oup.com/europace/article-pdf/16/10/1534/17428205/euu127.pdf. URL: https://doi.org/10.1093/europace/euu127.

[5] Piotr Augustyniak. "Wearable wireless heart rate monitor for continuous long-term variability studies". In: *Journal of Electrocardiology* 44.2 (2011), pp. 195–200. ISSN: 0022-0736. DOI: https://doi.org/10.1016/j.jelectrocard.2010.11.014. URL: https://www.sciencedirect.com/science/article/pii/S0022073610006126.

[6] Hans Craen. *Phasing out primary batteries will go against green deal*. Sept. 2020. URL: https://www.politico.eu/sponsored-content/phasing-out-primary-batteries-will-go-against-green-deal/.

[7] Heinz Albert Kiehne. *Battery technology handbook*. Vol. 118. CRC Press, 2003.

[8] Great British Watch Company. *Watch Batteries*. 2016. URL: https://www.great-british-watch.co.uk/watch-batteries/.

[9] Thad Starner and Joseph Paradiso. "Human Generated Power for Mobile Electronics". In: *Low Power Electron. Des.* 1990 (Nov. 2003). DOI: 10.1201/9781420039559.ch45.

[10] Günter Görge, Michael Kirstein, and Raimund Erbel. "Microgenerators for Energy Autarkic Pacemakers and Defibrillators: Fact or Fiction?" In: *Herz* 26 (2001), pp. 64–68.

[11] Joseph Paradiso and Thad Starner. "Energy Scavenging for Mobile and Wireless Electronics". In: *Pervasive Computing, IEEE* 4 (Feb. 2005), pp. 18–27. DOI: 10.1109/MPRV.2005.9.

[12] Yukikazu Hirashima. "Reduction and elimination of watch batteries". In: *Proceedings Second International Symposium on Environmentally Conscious Design and Inverse Manufacturing* (2001), pp. 832–835.

[13] The Seiko Museum. *Spring Drive*. URL: https://museum.seiko.co.jp/en/seiko_history/milestone/a6946f3e0078a97d44d08dd303293ba0d8ca8430/.

[14] H. Goto, T. Sugiura, and T. Kazui. "Feasibility of the automatic generating system (AGS) for quartz watches as a leadless pacemaker power source: a preliminary report". In: *Proceedings of the 20th Annual International Conference of the IEEE Engineering in Medicine and Biology Society. Vol.20 Biomedical Engineering Towards the Year 2000 and Beyond (Cat. No.98CH36286)*. 1998, 417–419 vol.1. DOI: 10.1109/IEMBS.1998.745933.

[15] Et al. "SPRING DRIVE". In: 46.1 (2002), pp. 10–15. DOI: 10.20805/micromechatronics.46.1_10.

[16] Jean Kumagai. "Kunio Koike Real Time". In: *IEEE Spectrum* 46.2 (2009), pp. 35–36.

[17] Shad Roundy. "Energy Scavenging for Wireless Sensor Nodes with a Focus on Vibration to Electricity Conversion". In: (Jan. 2003).

[18] Payasada Kotrappa. "Long term stability of electrets used in electret ion chambers". In: *Journal of Electrostatics - J ELECTROSTAT* 66 (July 2008), pp. 407–409. DOI: 10.1016/j.elstat.2008.04.008.

[19] Zibo Wu et al. "Largely enhanced electrostatic generator based on a bipolar electret charged by patterned contact micro-discharge and optimized substrates". In: *Nano Energy* 71 (2020), p. 104602. ISSN: 2211-2855. DOI: https://doi.org/10.1016/j.nanoen.2020.104602. URL: https://www.sciencedirect.com/science/article/pii/S2211285520301609.

[20] T. Miyoshi et al. "Low-profile rotational electret generator using print circuit board for energy harvesting from arm swing". In: *2018 IEEE Micro Electro Mechanical Systems (MEMS)* (2018), pp. 230–232.

[21] Zibo Wu et al. "Rotary disk multi-phase freestanding-electret generator with enhanced power and low ripple output". In: *Nano Energy* 83 (2021), p. 105787. ISSN: 2211-2855. DOI: https://doi.org/10.1016/j.nanoen.2021.105787. URL: https://www.sciencedirect.com/science/article/pii/S2211285521000458.

[22] Takumi Tsutsumino et al. "High-Performance Polymer Electret for Micro Seismic Generator". In: 2005.

[23] U. Bartsch, J. Gaspar, and O. Paul. "A 2D Electret-Based Resonant Micro Energy Harvester". In: *2009 IEEE 22nd International Conference on Micro Electro Mechanical Systems*. 2009, pp. 1043–1046. DOI: 10.1109/MEMSYS.2009.4805565.

[24] Eric Yeatman. "Energy harvesting from motion using rotating and gyroscopic proof masses". In: *Proceedings of The Institution of Mechanical Engineers Part C-journal of Mechanical Engineering Science - PROC INST MECH ENG C-J MECH E* 222 (Jan. 2008). DOI: 10.1243/09544062JMES701.

[25] *A Technical Perspective - What are Jewel Bearings in a watch and why are they crucial?* [Accessed 12-Sep-2022]. URL: https://monochrome-watches.com/technical-perspective-jewel-bearings-watch-movement-rubies/.

[26] iPCB. *Teflon PCB*. URL: https://www.ipcb.com/rfpcb/698.html/.

[27] Melker Staffan Johansson et al. “Time spent cycling, walking, running, standing and sedentary: a cross-sectional analysis of accelerometer-data from 1670 adults in the Copenhagen City Heart Study”. In: *BMC Public Health* 19 (2019).

[28] *100mm Borofloat 33 Glass Wafer*. [Accessed 07-Nov-2022]. URL: https://order.universitywafer.com/default.aspx?cat=Borofloat%2033%20Glass&diam=100mm.

[29] *CYTOP Technical Brochure Request - AGC Chemicals Europe*. [Accessed 01-Sep-2022]. URL: https://www.agcce.com/cytop-technical-brochure.

[30] Hao Wu et al. “Influence of fluoropolymer surface wettability on electrowetting display performance”. In: *Displays* 53 (2018), pp. 47–53. ISSN: 0141-9382. DOI: https://doi.org/10.1016/j.displa.2018.02.002. URL: https://www.sciencedirect.com/science/article/pii/S0141938217301282.

[31] G. M. Sessler. “Physical principles of electrets”. In: *Electrets*. Ed. by Gerhard M. Sessler. Berlin, Heidelberg: Springer Berlin Heidelberg, 1987, pp. 13–80. ISBN: 978-3-540-70750-9. DOI: 10.1007/3540173358_10. URL: https://doi.org/10.1007/3540173358_10.

[32] Kwan Chi Kao. “5 - Electrets”. In: *Dielectric Phenomena in Solids*. Ed. by Kwan Chi Kao. San Diego: Academic Press, 2004, pp. 283–326. ISBN: 978-0-12-396561-5. DOI: https://doi.org/10.1016/B978-012396561-5/50015-3. URL: https://www.sciencedirect.com/science/article/pii/B9780123965615500153.

[33] Ying-Hsuan Chou et al. “Polymeric charge storage electrets for non-volatile organic field effect transistor memory devices”. In: *Polymer Chemistry* 6.3 (2015), pp. 341–352.

[34] W. Olthuis and P. Bergveld. “On the charge storage and decay mechanism in silicon dioxide electrets”. In: *IEEE Transactions on Electrical Insulation* 27.4 (1992), pp. 691–697. DOI: 10.1109/14.155784.

[35] Friedrich Paschen. “Ueber die zum Funkenübergang in Luft, Wasserstoff und Kohlensäure bei verschiedenen Drucken erforderliche Potentialdifferenz”. In: *Annalen der Physik* 273.5 (1889), pp. 69–96. DOI: https://doi.org/10.1002/andp.18892730505. eprint: https://onlinelibrary.wiley.com/doi/pdf/10.1002/andp.18892730505.

[36] Sebastien Boisseau, Ghislain Despesse, and Alain Sylvestre. “Optimization of an electret-based energy harvester”. In: *Smart Materials Structures - SMART MATER STRUCT* 19 (Nov. 2011). DOI: 10.1088/0964-1726/19/7/075015.

[37] Xin Li et al. “Polymer electrets and their applications”. In: *Journal of Applied Polymer Science* 138.19 (2021), p. 50406. DOI: https://doi.org/10.1002/app.50406. eprint: https://onlinelibrary.wiley.com/doi/pdf/10.1002/app.50406. URL: https://onlinelibrary.wiley.com/doi/abs/10.1002/app.50406.

[38] H. Amjadi and C. Thielemann. “Silicon-based inorganic electrets for application in micromachined devices”. In: *IEEE Transactions on Dielectrics and Electrical Insulation* 3.4 (1996), pp. 494–498. DOI: 10.1109/94.536727.

[39] Jose A Giacometti and Osvaldo N Oliveira. “Corona charging of polymers”. In: *IEEE Transactions on Electrical Insulation* 27.5 (1992), pp. 924–943.

[40] G. M. Sessler and J. E. West. “Electret transducers: a review”. In: *The Journal of the Acoustical Society of America* 53.6 (1973), pp. 1589–1600. DOI: 10.1121/1.1913507. eprint: https://doi.org/10.1121/1.1913507. URL: https://doi.org/10.1121/1.1913507.

[41] B. Gross, G. M. Sessler, and J. E. West. “Charge dynamics for electron-irradiated polymer-foil electrets”. In: *Journal of Applied Physics* 45.7 (1974), pp. 2841–2851. DOI: 10.1063/1.1663689. eprint: https://doi.org/10.1063/1.1663689. URL: https://doi.org/10.1063/1.1663689.

[42] Kei Hagiwara et al. “Soft X-ray Charging Method for a Silicon Electret Condenser Microphone”. In: *Applied Physics Express* 3.9 (Sept. 2010), p. 091502. DOI: 10.1143/apex.3.091502. URL: https://doi.org/10.1143/apex.3.091502.

[43] Kei Hagiwara et al. “Electret charging method based on soft X-ray photoionization for MEMS transducers”. In: *IEEE Transactions on Dielectrics and Electrical Insulation* 19.4 (2012), pp. 1291–1298. DOI: 10.1109/TDEI.2012.6260003.

[44] Rui Igreja and C.J. Dias. “Analytical evaluation of the interdigital electrodes capacitance for a multi-layered structure”. In: *Sensors and Actuators A: Physical* 112.2 (2004), pp. 291–301. ISSN: 0924-4247. DOI: https://doi.org/10.1016/j.sna.2004.01.040. URL: https://www.sciencedirect.com/science/article/pii/S0924424704000779.

[45] J Nakano et al. “MEMS Rotational Electret Energy Harvester for Human Motion”. In: *Journal of Physics: Conference Series* 660 (Dec. 2015), p. 012052. DOI: 10.1088/1742-6596/660/1/012052.

[46] Yuji Suzuki et al. “A MEMS electret generator with electrostatic levitation for vibration-driven energy-harvesting applications”. In: *Journal of Micromechanics and Microengineering* 20.10 (Sept. 2010), p. 104002. DOI: 10.1088/0960-1317/20/10/104002. URL: https://doi.org/10.1088/0960-1317/20/10/104002.

[47] Andrea Crovetto, Fei Wang, and Ole Hansen. “An electret-based energy harvesting device with a wafer-level fabrication process”. In: *Journal of Micromechanics and Microengineering* 23.11 (Oct. 2013), p. 114010. DOI: 10.1088/0960-1317/23/11/114010. URL: https://doi.org/10.1088/0960-1317/23/11/114010.

[48] Justin Boland et al. “Micro electret power generator”. In: *The Sixteenth Annual International Conference on Micro Electro Mechanical Systems, 2003. MEMS-03 Kyoto. IEEE*. IEEE. 2003, pp. 538–541.

[49] Mingzhao Bi et al. “Freestanding-electret rotary generator at an average conversion efficiency of 56%: Theoretical and experimental studies”. In: *Nano Energy* 41 (2017), pp. 434–442. ISSN: 2211-2855. DOI: https://doi.org/10.1016/j.nanoen.2017.09.057.

[50] Takumi Tsutsumino et al. “Seismic Power Generator Using High-Performance Polymer Electret”. In: vol. 2006. Feb. 2006, pp. 98–101. ISBN: 0-7803-9475-5. DOI: 10.1109/MEMSYS.2006.1627745.

[51] S Kim et al. “Investigation of Charge Stability in Amorphous Fluorinated Polymer Using Quantum Chemical Analysis”. In: Oct. 2019. DOI: 10.1109/CEIDP47102.2019.9009906.

[52] Seonwoo Kim et al. “Effect of end group of amorphous perfluoro-polymer electrets on electron trapping”. In: *Science and Technology of Advanced Materials* 19.1 (2018). PMID: 29915625, pp. 486–494. DOI: 10.1080/14686996.2018.1477395. eprint: https://doi.org/10.1080/14686996.2018.1477395. URL: https://doi.org/10.1080/14686996.2018.1477395.

[53] Wei Zhao et al. “Field-Based Capacitance Modeling for Sub-65-nm On-Chip Interconnect”. In: *IEEE Transactions on Electron Devices* 56.9 (2009), pp. 1862–1872. DOI: 10.1109/TED.2009.2026162.

[54] Andrea Crovetto. “Modeling and Fabrication of Electret-based 2D Micro Energy Harvester”. PhD thesis. Sept. 2012. DOI: 10.13140/2.1.2458.2402.

[55] Huicong Liu et al. “A non-resonant rotational electromagnetic energy harvester for low-frequency and irregular human motion”. In: *Applied Physics Letters* 113 (Nov. 2018), p. 203901. DOI: 10.1063/1.5053945.

[56] Miah A. Halim et al. “A miniaturized electromagnetic vibration energy harvester using flux-guided magnet stacks for human-body-induced motion”. In: *Sensors and Actuators A: Physical* 249 (2016), pp. 23–31. ISSN: 0924-4247. DOI: https://doi.org/10.1016/j.sna.2016.08.008.

[57] Michail Kiziroglou, Cairan He, and Eric Yeatman. “Non-resonant electrostatic energy harvesting from a rolling mass”. In: July 2008, pp. 318–321. DOI: 10.1109/ISSMDBS.2008.4575083.

[58] A. Erturk and D.J. Inman. “Broadband piezoelectric power generation on high-energy orbits of the bistable Duffing oscillator with electromechanical coupling”. In: *Journal of Sound and Vibration* 330.10 (2011). Dynamics of Vibro-Impact Systems, pp. 2339–2353. ISSN: 0022-460X. DOI: https://doi.org/10.1016/j.jsv.2010.11.018.

[59] Dapeng Qiao et al. “A New PCB-Based Low-Cost Accelerometer for Human Motion Sensing”. In: Oct. 2008, pp. 56–60. DOI: 10.1109/ICAL.2008.4636119.

[60] Thijs WA Blad and Nima Tolou. “On the efficiency of energy harvesters: A classification of dynamics in miniaturized generators under low-frequency excitation”. In: *Journal of Intelligent Material Systems and Structures* 30.16 (2019), pp. 2436–2446. DOI: 10.1177/1045389X19862621.

[61] Hiroshi Okamoto et al. “Improving an electret energy harvester by redirecting the electric field”. In: (Jan. 2008).

[62] J. Wei. “Distributed capacitance of planar electrodes in optic and acoustic surface wave devices”. In: *IEEE Journal of Quantum Electronics* 13 (1977), pp. 152–158.

[63] N Matsuura, H Ishii, and Y Tanaka. “Demonstration of an electret generator using self-assembled electret for energy harvesting without any charging process”. In: *Journal of Physics: Conference Series* 1407 (Nov. 2019), p. 012116. DOI: 10.1088/1742-6596/1407/1/012116.

[64] Y Naruse et al. “Electrostatic micro power generation from low-frequency vibration such as human motion”. In: *Journal of Micromechanics and Microengineering* 19 (Aug. 2009), p. 094002. DOI: 10.1088/0960-1317/19/9/094002.

[65] Andrea Crovetto, Fei Wang, and Ole Hansen. “Modeling and Optimization of an Electrostatic Energy Harvesting Device”. In: *Journal of Microelectromechanical Systems* 23 (Oct. 2014). DOI: 10.1109/JMEMS.2014.2306963.

[66] Erick O. Torres and Gabriel A. Rincón-Mora. “Electrostatic Energy-Harvesting and Battery-Charging CMOS System Prototype”. In: *Trans. Cir. Sys. Part I* 56.9 (Sept. 2009), pp. 1938–1948. ISSN: 1549-8328. DOI: 10.1109/TCSI.2008.2011578. URL: https://doi.org/10.1109/TCSI.2008.2011578.

[67] Hiroshi Aozasa et al. “Analysis of Carrier Traps in Sisubb3/b/subNsubb4/b/subin Oxide/Nitride/Oxide for Metal/Oxide/Nitride/Oxide/Silicon Nonvolatile Memory”. In: *Japanese Journal of Applied Physics* 38.Part 1, No. 3A (Mar. 1999), pp. 1441–1447. DOI: 10.1143/jjap.38.1441. URL: https://doi.org/10.1143/jjap.38.1441.

[68] Tae Hun Kim et al. “Electron trap density distribution of Si-rich silicon nitride extracted using the modified negative charge decay model of silicon-oxide-nitride-oxide-silicon structure at elevated temperatures”. In: *Applied Physics Letters* 89.6 (2006), p. 063508. DOI: 10.1063/1.2335619. eprint: https://doi.org/10.1063/1.2335619. URL: https://doi.org/10.1063/1.2335619.

[69] Hiroshi Aozasa, Ichiro Fujiwara, and Yoshiaki Kamigaki. “Analysis of Carrier Traps in Silicon Nitride Film with Discharge Current Transient Spectroscopy, Photoluminescence, and Electron Spin Resonance”. In: *Japanese Journal of Applied Physics* 46.9A (Sept. 2007), pp. 5762–5766. DOI: 10.1143/jjap.46.5762. URL: https://doi.org/10.1143/jjap.46.5762.

[70] Jang Uk. Lee et al. “Optical capacitance-voltage characterization of charge traps in the trapping nitride layer of charge trapped flash memory devices”. In: *Applied Physics Letters* 91.22 (2007), p. 223511. DOI: 10.1063/1.2819092. eprint: https://doi.org/10.1063/1.2819092. URL: https://doi.org/10.1063/1.2819092.

[71] J.A. Voorthuyzen, K. Keskin, and P. Bergveld. “Investigations of the surface conductivity of silicon dioxide and methods to reduce it”. In: *Surface Science* 187.1 (1987), pp. 201–211. ISSN: 0039-6028. DOI: https://doi.org/10.1016/S0039-6028(87)80132-2. URL: https://www.sciencedirect.com/science/article/pii/S0039602887801322.

[72] R. Dammel. *Diazonaphthoquinone-based Resists*. Tutorial Texts. SPIE Optical Engineering Press, 1993. ISBN: 9780819410191. URL: https://books.google.nl/books?id=X3UeI1nb7hoC.

[73] Susanna Laurén. *Wetting in electronics - how HMDS Treatment Works?* 2020. URL: https://www.biolinscientific.com/blog/wetting-in-electronics-how-hmds-treatment-works.

[74] S. Boisseau et al. “New DRIE-Patterned Electrets for Vibration Energy Harvesting”. In: *EPJ Web of Conferences* 33 (2012), p. 02010. DOI: 10.1051/epjconf/20123302010. URL: https://doi.org/10.1051%2Fepjconf%2F20123302010.

[75] Takumi Tsutsumino et al. “Seismic power generator using high-performance polymer electret”. In: *19th IEEE international conference on micro electro mechanical systems*. IEEE. 2006, pp. 98–101.

[76] J. Boland et al. “Micro electret power generator”. In: *The Sixteenth Annual International Conference on Micro Electro Mechanical Systems, 2003. MEMS-03 Kyoto. IEEE*. 2003, pp. 538–541. DOI: 10.1109/MEMSYS.2003.1189805.

[77] Shiwen Wang et al. “Linear freestanding electret generator for harvesting swinging motion energy: Optimization and experiment”. In: *Nano Energy* 65 (2019), p. 104013. ISSN: 2211-2855. DOI: https://doi.org/10.1016/j.nanoen.2019.104013. URL: https://www.sciencedirect.com/science/article/pii/S2211285519307207.

[78] Nima Tolou, Vincent Henneken, and Just Herder. “Statically Balanced Compliant Micro Mechanisms (SB-MEMS): Concepts and Simulation”. In: vol. 2. Jan. 2010. DOI: 10.1115/DETC2010-28406.

[79] *Basic Bearing Knowledge*. [Accessed 08-Sep-2022]. URL: https://koyo.jtekt.co.jp/en/support/bearing-knowledge/8-4000.html.

[80] Xingjian Dai, Kai Zhang, and Changliang Tang. “Friction and wear of pivot jewel bearing in oil-bath lubrication for high rotational speed application”. In: *Wear* 302.1 (2013). Wear of Materials 2013, pp. 1506–1513. ISSN: 0043-1648. DOI: https://doi.org/10.1016/j.wear.2013.01.032. URL: https://www.sciencedirect.com/science/article/pii/S0043164813000525.

[81] Vivienne HALLEUX. “New EU regulatory framework for batteries: Setting sustainability requirements”. In: (2021).

[82] Logan S. McCarty, Adam Winkleman, and George M. Whitesides. “Ionic electrets: electrostatic charging of surfaces by transferring mobile ions upon contact.” In: *Journal of the American Chemical Society* 129 13 (2007), pp. 4075–88.

[83] Junqing Zhao et al. “Remarkable merits of triboelectric nanogenerator than electromagnetic generator for harvesting small-amplitude mechanical energy”. In: *Nano Energy* 61 (2019), pp. 111–118. ISSN: 2211-2855. DOI: https://doi.org/10.1016/j.nanoen.2019.04.047. URL: https://www.sciencedirect.com/science/article/pii/S2211285519303489.

[84] Xinping Cao et al. “Electromagnetic Energy Harvesting Circuit With Feedforward and Feedback DC–DC PWM Boost Converter for Vibration Power Generator System”. In: *Power Electronics, IEEE Transactions on* 22 (Apr. 2007), pp. 679–685. DOI: 10.1109/TPEL.2006.890009.

[85] Steve P. Beeby et al. “A micro electromagnetic generator for vibration energy harvesting”. In: *Journal of Micromechanics and Microengineering* 17 (2007), pp. 1257–1265.

[86] Hailing Fu and Eric M. Yeatman. “A methodology for low-speed broadband rotational energy harvesting using piezoelectric transduction and frequency up-conversion”. In: *Energy* 125.C (2017), pp. 152–161. DOI: 10.1016/j.energy.2017.02.. URL: https://ideas.repec.org/a/eee/energy/v125y2017icp152-161.html.

[87] Shad Roundy. “On the Effectiveness of Vibration-based Energy Harvesting”. In: *Journal of Intelligent Material Systems and Structures* 16 (Oct. 2005), pp. 809–823. DOI: 10.1177/1045389X05054042.

[88] M.A. Halim et al. “An electromagnetic rotational energy harvester using sprung eccentric rotor, driven by pseudo-walking motion”. In: *Applied Energy* 217 (2018), pp. 66–74. ISSN: 0306-2619. DOI: https://doi.org/10.1016/j.apenergy.2018.02.093. URL: https://www.sciencedirect.com/science/article/pii/S0306261918302186.

[89] Eric Yeatman. “Energy harvesting from motion using rotating and gyroscopic proof masses”. In: *Proceedings of The Institution of Mechanical Engineers Part C-journal of Mechanical Engineering Science - PROC INST MECH ENG C-J MECH E* 222 (Jan. 2008). DOI: 10.1243/09544062JMES701.

[90] Ghislain Despesse et al. “High Damping Electrostatic System For Vibration Energy Scavenging”. In: Oct. 2005, pp. 283–286. DOI: 10.1145/1107548.1107617.

[91] Heung Soo Kim, Joo-Hyong Kim, and Jaehwan Kim. “A Review of Piezoelectric Energy Harvesting Based on Vibration”. In: *International Journal of Precision Engineering and Manufacturing* 12 (Dec. 2011). DOI: 10.1007/s12541-011-0151-3.

[92] Kangqi Fan et al. “Scavenging energy from human walking through a shoe-mounted piezoelectric harvester”. In: *Applied Physics Letters* 110 (Apr. 2017), p. 143902. DOI: 10.1063/1.4979832.

[93] Bor-Shiunn Lee et al. “Piezoelectric MEMS generators fabricated with an aerosol deposition PZT thin film”. In: *Journal of Micromechanics and Microengineering* 19 (2009), p. 065014.

[94] Lei Gu. “Low-frequency piezoelectric energy harvesting prototype suitable for the MEMS implementation”. In: *Microelectron. J.* 42 (2011), pp. 277–282.

[95] Lokesh Dhakar et al. “A new energy harvester design for high power output at low frequencies”. In: *Sensors and Actuators A-physical* 199 (2013), pp. 344–352.

[96] Huicong Liu et al. “Investigation of the Nonlinear Electromagnetic Energy Harvesters From Hand Shaking”. In: *IEEE Sensors Journal* 15 (2015), pp. 2356–2364.

[97] Mahmoud Halima et al. “An electromagnetic rotational energy harvester using sprung eccentric rotor , driven by pseudo-walking motion”. In: 2018.

[98] Peihong Wang et al. “A micro electromagnetic low level vibration energy harvester based on MEMS technology”. In: *Microsystem Technologies* 15 (2009), pp. 941–951.

[99] Matthias Geisler et al. “Looped energy harvester for human motion”. In: *Smart Materials and Structures* 26 (Aug. 2017). DOI: 10.1088/1361-665X/aa8918.

[100] John Oxaal, Mona Mostafa Hella, and Diana-Andra Borca-Tasciuc. “Electrostatic MEMS vibration energy harvester for HVAC applications with impact-based frequency up-conversion”. In: *Journal of Micromechanics and Microengineering* 26 (2016), p. 124012.

[101] Daniel Hoffmann, Bernd Folkmer, and Yiannos Manoli. “Fabrication, characterization and modelling of electrostatic micro-generators”. In: *Journal of Micromechanics and Microengineering* 19 (2009), p. 094001.

[102] Philippe Basset et al. “Electrostatic vibration energy harvester with combined effect of electrical nonlinearities and mechanical impact”. In: *Journal of Micromechanics and Microengineering* 24 (Feb. 2014). DOI: 10.1088/0960-1317/24/3/035001.

[103] Ling Bu et al. “Non-resonant electrostatic energy harvester for wideband applications”. In: *Micro & Nano Letters* 8.3 (2013), pp. 135–137. DOI: https://doi.org/10.1049/mnl.2012.0924. eprint: https://ietresearch.onlinelibrary.wiley.com/doi/pdf/10.1049/mnl.2012.0924. URL: https://ietresearch.onlinelibrary.wiley.com/doi/abs/10.1049/mnl.2012.0924.

[104] Hailing Fu, Guangzhu Chen, and Nan Bai. “Electrode Coverage Optimization for Piezoelectric Energy Harvesting from Tip Excitation”. In: *Sensors* 18 (Mar. 2018), p. 804. DOI: 10.3390/s18030804.

[105] Kangqi Fan et al. “Design and development of a multipurpose piezoelectric energy harvester”. In: *Energy Conversion and Management* 96 (2015), pp. 430–439. ISSN: 0196-8904. DOI: https://doi.org/10.1016/j.enconman.2015.03.014. URL: https://www.sciencedirect.com/science/article/pii/S0196890415002241.

[106] Shad Roundy and Paul K. Wright. “A piezoelectric vibration based generator for wireless electronics”. In: *Smart Materials and Structures* 13 (2004), pp. 1131–1142.

[107] Anjana Jain et al. “Dielectric and piezoelectric properties of PVDF/PZT composites: A review”. In: *Polymer Engineering & Science* 55.7 (2015), pp. 1589–1616. DOI: https://doi.org/10.1002/pen.24088. eprint: https://onlinelibrary.wiley.com/doi/pdf/10.1002/pen.24088. URL: https://onlinelibrary.wiley.com/doi/abs/10.1002/pen.24088.

[108] Maria Teresa Todaro et al. “Piezoelectric MEMS vibrational energy harvesters: Advances and outlook”. In: *Microelectronic Engineering* 183-184 (2017), pp. 23–36. ISSN: 0167-9317. DOI: https://doi.org/10.1016/j.mee.2017.10.005. URL: https://www.sciencedirect.com/science/article/pii/S0167931717303349.

[109] Isaku Kanno. “Piezoelectric MEMS for energy harvesting”. In: 660 (Dec. 2015), p. 012001. DOI: 10.1088/1742-6596/660/1/012001. URL: https://doi.org/10.1088/1742-6596/660/1/012001.

[110] Reza Abdolvand, Hedy Fatemi, and Sina Moradian. “Quality Factor and Coupling in Piezoelectric MEMS Resonators”. In: *Piezoelectric MEMS Resonators*. Ed. by Harmeet Bhugra and Gianluca Piazza. Cham: Springer International Publishing, 2017, pp. 133–152. ISBN: 978-3-319-28688-4. DOI: 10.1007/978-3-319-28688-4_5. URL: https://doi.org/10.1007/978-3-319-28688-4_5.

[111] Miah A. Halim and Jae Y. Park. “Theoretical modeling and analysis of mechanical impact driven and frequency up-converted piezoelectric energy harvester for low-frequency and wide-bandwidth operation”. In: *Sensors and Actuators A: Physical* 208 (2014), pp. 56–65. ISSN: 0924-4247. DOI: https://doi.org/10.1016/j.sna.2013.12.033. URL: https://www.sciencedirect.com/science/article/pii/S0924424713006316.

[112] Yuji Suzuki. “Recent progress in MEMS electret generator for energy harvesting”. In: *IEEJ Transactions on Electrical and Electronic Engineering* 6.2 (2011), pp. 101–111. DOI: https://doi.org/10.1002/tee.20631. eprint: https://onlinelibrary.wiley.com/doi/pdf/10.1002/tee.20631. URL: https://onlinelibrary.wiley.com/doi/abs/10.1002/tee.20631.

[113] C Eichhorn, Frank Goldschmidtboeing, and Peter Woias. “Bidirectional frequency tuning of a piezoelectric energy converter based on a cantilever beam”. In: *Journal of Micromechanics and Microengineering* 19 (Aug. 2009), p. 094006. DOI: 10.1088/0960-1317/19/9/094006.

[114] Eli Leland and Paul Wright. “Resonance tuning of piezoelectric vibration energy scavenging generators using compressive axial preload”. In: *Smart Materials and Structures* 15 (Sept. 2006), p. 1413. DOI: 10.1088/0964-1726/15/5/030.

[115] Ivo Ayala et al. “A tunable kinetic energy harvester with dynamic over range protection”. In: *Smart Materials and Structures* 19 (Sept. 2010), p. 115005. DOI: 10.1088/0964-1726/19/11/115005.

[116] Rodrigo Ai et al. “Piezoelectric Vibration-Based Energy Harvesting Enhancement Exploiting Nonsmoothness”. In: *Actuators* 8.1 (2019). ISSN: 2076-0825. DOI: 10.3390/act8010025. URL: https://www.mdpi.com/2076-0825/8/1/25.

[117] Sergio P Pellegrini et al. “Bistable vibration energy harvesters: A review”. In: *Journal of Intelligent Material Systems and Structures* 24 (July 2013), pp. 1303–1312. DOI: 10.1177/1045389X12444940.

[118] Helios Vocca et al. “Kinetic energy harvesting with bistable oscillators”. In: *Applied Energy* 97 (2012). Energy Solutions for a Sustainable World - Proceedings of the Third International Conference on Applied Energy, May 16-18, 2011 - Perugia, Italy, pp. 771–776. ISSN: 0306-2619. DOI: https://doi.org/10.1016/j.apenergy.2011.12.087. URL: https://www.sciencedirect.com/science/article/pii/S0306261911008932.

[119] B. Andò et al. “A bistable buckled beam based approach for vibrational energy harvesting”. In: *Sensors and Actuators A: Physical* 211 (2014), pp. 153–161. ISSN: 0924-4247. DOI: https://doi.org/10.1016/j.sna.2013.12.027. URL: https://www.sciencedirect.com/science/article/pii/S0924424713006250.

[120] Nurettin Sezer and Muammer Koç. “A comprehensive review on the state-of-the-art of piezoelectric energy harvesting”. In: *Nano Energy* 80 (2021), p. 105567. ISSN: 2211-2855. DOI: https://doi.org/10.1016/j.nanoen.2020.105567. URL: https://www.sciencedirect.com/science/article/pii/S2211285520311411.

[121] Stephen P. Beeby and Terence O’Donnell. “Electromagnetic Energy Harvesting”. In: *Energy Harvesting Technologies*. Ed. by Shashank Priya and Daniel J. Inman. Boston, MA: Springer US, 2009, pp. 129–161. ISBN: 978-0-387-76464-1. DOI: 10.1007/978-0-387-76464-1_5. URL: https://doi.org/10.1007/978-0-387-76464-1_5.

[122] Pranay Podder et al. “Silicon MEMS bistable electromagnetic vibration energy harvester using double-layer micro-coils”. In: *Journal of Physics: Conference Series* 660 (Dec. 2015), p. 012124. DOI: 10.1088/1742-6596/660/1/012124.

[123] Ashok Batra and Almuatasim Alomari. *Power Harvesting via Smart Materials*. July 2017. ISBN: 9781510608498. DOI: 10.1117/3.2268643.

[124] Hailing Fu et al. “Rotational energy harvesting for self-powered sensing”. In: *Joule* 5.5 (2021), pp. 1074–1118. ISSN: 2542-4351. DOI: https://doi.org/10.1016/j.joule.2021.03.006. URL: https://www.sciencedirect.com/science/article/pii/S254243512100101X.

[125] Qing-Ming Wang et al. “Electromechanical coupling and output efficiency of piezoelectric bending actuators”. In: *IEEE Transactions on Ultrasonics, Ferroelectrics, and Frequency Control* 46.3 (1999), pp. 638–646. DOI: 10.1109/58.764850.

[126] Y. Lu et al. “A nonlinear MEMS electrostatic kinetic energy harvester for human-powered biomedical devices”. In: *Applied Physics Letters* 107.25 (2015), p. 253902. DOI: 10.1063/1.4937587. eprint: https://doi.org/10.1063/1.4937587. URL: https://doi.org/10.1063/1.4937587.

[127] Binh Truong, Cuong Le, and Einar Halvorsen. “Experimentally verified model of electrostatic energy harvester with internal impacts”. In: vol. 2015. Jan. 2015. DOI: 10.1109/MEMSYS.2015.7051162.

[128] V. Leonov and Chris Van Hoof. “Multilayer Inorganic Electrets with SiO2 and Si3N4 Layers for Applications on Heated Machinery”. In: *Smart Materials Research* 2012 (May 2012), p. 904168. DOI: 10.1155/2012/904168.

[129] Heung Soo Kim, Joo-Hyong Kim, and Jaehwan Kim. “A Review of Piezoelectric Energy Harvesting Based on Vibration”. In: *International Journal of Precision Engineering and Manufacturing* 12 (Dec. 2011). DOI: 10.1007/s12541-011-0151-3.

[130] Stephen Beeby and Neil White. “Energy Harvesting for Autonomous Systems”. In: 308 (Jan. 2010).

[131] Sébastien Boisseau et al. “Cantilever-based electret energy harvesters”. In: *Smart Materials and Structures* 20.10 (2011), p. 105013.

[132] Daigo Miki et al. “MEMS ELECTRET GENERATOR WITH ELECTROSTATIC LEVITATION”. In: 2009.

[133] Hiroshi Okamoto, Teppei Onuki, and Hiroki Kuwano. “Improving an electret transducer by fully utilizing the implanted charge”. In: *Applied Physics Letters* 93 (Sept. 2008), pp. 122901–122901. DOI: 10.1063/1.2985899.

[134] GerHard M Sessler and James E West. *Electroacoustic transducer*. Jan. 1964.

[135] Heung Soo Kim, Joo-Hyong Kim, and Jaehwan Kim. “A review of piezoelectric energy harvesting based on vibration”. In: *International journal of precision engineering and manufacturing* 12.6 (2011), pp. 1129–1141.

[136] Alperen Toprak and Onur Tigli. “Piezoelectric energy harvesting: State-of-the-art and challenges”. In: *Applied Physics Reviews* 1.3 (2014), p. 031104.

[137] Kwan Chi Kao. “Dielectric phenomena in solids : with emphasis on physical concepts of electronic processes”. In: 2004.

[138] Jinwen Zhang, Xudong Zou, and Yaping Zhang. “Improvement of the performance of the PECVD SiO2/Si3N4 double-layer electrets”. In: *IEEE Transactions on Dielectrics and Electrical Insulation* 18.2 (2011), pp. 456–462. DOI: 10.1109/TDEI.2011.5739449.

[139] W. Olthuis and P. Bergveld. “On the charge storage and decay mechanism in silicon dioxide electrets”. In: *IEEE Transactions on Electrical Insulation* 27.4 (1992), pp. 691–697. DOI: 10.1109/14.155784.